Selection of Vector Boson Fusion Events in the $H \to \gamma\gamma$ Decay Channel Using an Inclusive Event Shape

Früd Braren

Date of Birth
6.12.1988

Master's Thesis

University of Hamburg

2015

Primary supervisor:	Dr. Kerstin Tackmann
Secondary supervisor:	Prof. Dr. Peter Schleper

Eidesstattliche Erklärung

Hiermit bestätige ich, dass die vorliegende Arbeit von mir selbständig verfasst wurde und ich keine anderen als die angegebenen Hilfsmittel – insbesondere keine im Quellenverzeichnis nicht benannten Internet-Quellen – benutzt habe und die Arbeit von mir vorher nicht einem anderen Prüfungsverfahren eingereicht wurde. Die eingereichte schriftliche Fassung entspricht der auf dem elektronischen Speichermedium. Ich bin damit einverstanden, dass die Masterarbeit veröffentlicht wird.

Hamburg, 16. 4. 2015,   Früd Braren

Abstract

Present-day measurements of the signal strength of the Higgs-boson production mode vector boson fusion tend to suffer from large theoretical uncertainties on the gluon fusion contamination in the vector boson fusion selection. The measurements are still limited by the statistical uncertainties, but as more data will be recorded, the statistical uncertainties will be reduced. Therefore it is of importance to think of alternative vector boson fusion selections with a better control over the theoretical uncertainty. Vector boson fusion selections use a central jet veto. Such a veto can be implemented via the inclusive event shape 2-jettiness as an alternative to the presently used central-jet veto.

In this thesis, the properties of this event shape in $H \rightarrow \gamma\gamma$ events and its use in a vector boson fusion selection are examined. The theoretical uncertainties accompanying this event-shape based selection are studied. Finally, the vector boson fusion signal strength is determined using 8 TeV ATLAS data with a vector boson fusion selection which relies on cuts on the 2-jettiness.

Zusammenfassung

Aktuelle Messungen der Signalstärke des Higgsboson-Produktionskanals Vektorbosonfusion leiden an großen theoretischen Unsicherheiten hinsichtlich der Anzahl an Gluonfusion-Ereignissen in der Vektorbosonfusion-Selektion. Derzeit sind die Unsicherheiten der Messungen vor allem durch die statistischen Unsicherheiten dominiert, doch diese statistischen Unsicherheiten werden durch das weitere Sammeln von Daten reduziert werden. Daher ist es geboten, alternative Vektorbosonfusion-Selektionen zu erwägen, die eine bessere Kontrolle über die theoretischen Unsicherheiten bieten. Vektorbosonfusion-Selektionen nutzen ein Veto gegen zusätzliche zentrale Jets. Ein solches Veto kann alternativ zu der derzeitig verwendeten Veto-Technik mittels der inklusiven *Event Shape*-Observablen mit dem Namen *2-Jettiness* implementiert werden.

Die Eigenschaften jener *Event Shape* in $H \rightarrow \gamma\gamma$ - Ereignissen und seine Anwendbarkeit in einer Vektorbosonfusion-Selektion werden in dieser Arbeit untersucht. Die mit der Verwendung dieser Observablen einhergehenden theoretischen Unsicherheiten werden bestimmt. Anhand von 8 TeV-ATLAS-Daten wird unter Verwendung einer auf der *2-Jettiness* basierenden Vektorbosonfusion-Selektion die Signalstärke des Vektorbosonfusion-Higgsboson-Produktionskanals gemessen.

Contents

In the year 2012 a new particle has been found [1], and its properties are in the focus of research. At the present time, the measured properties are in agreement with the hypothesis that the discovered particle is a Higgs boson [2][3]. One of its properties which is investigated is the coupling to the Standard Model particles. The various coupling strengths can be determined via the measurement of branching ratio as well as via the measurement of production cross sections for different Higgs-boson production modes. Five such Higgs boson production channels are currently being studied; gluon fusion (ggF) and vector boson fusion (VBF) are predicted to be the modes with the highest production cross sections, i.e. $\sigma_{\mathrm{ggF}} = 19.2\,\mathrm{pb}$ and $\sigma_{\mathrm{VBF}} = 1.6\,\mathrm{pb}$ at $\sqrt{s} = 8\,\mathrm{TeV}$ collisions at the LHC for a Standard-Model Higgs boson with a mass of $m_H = 125.4\,\mathrm{GeV}$ [4]. Higgs events involving the fusion of two massive vector bosons, i.e. VBF events, are more likely to contain two well-separated jets than gluon fusion events and non-Higgs events. Hence, VBF-enriched selections commonly select events with at least two jets. The highest significance in a VBF-enriched selection with respect to ggF background can be achieved when one imposes a veto on additional central jets, since, due to the color structure of VBF events, radiation between the two outgoing partons is suppressed. The same does not hold for ggF events, a fact that can be used in order to discriminate against ggF events in a VBF selection. The vector boson fusion selection that is used in the latest ATLAS paper [2] analyzing the compatibility of measured Higgs boson production cross sections with Standard Model predictions employs a multivariate analysis that involves variables which are sensitive to additional hadronic radiation. With this selection, a high VBF signal fraction is achieved at the price of a sizable theoretical uncertainty. Furthermore, the use of multivariate techniques makes the estimation of the theoretical uncertainty more complicated. Because of even larger statistical uncertainties, the sizable theoretical uncertainty is not important at the present amount of integrated luminosity. But since the dataset will quickly grow and the statistical uncertainty will decrease in the next years of LHC operation, the investigation of alternative VBF selections with better control over the theoretical uncertainties is recommended.

The event shape 2-jettiness is an inclusive measure of how much radiation in addition to two given jets is present in a given event [5]. Thus, it can be used as a veto on additional radiation and is therefore possibly valuable for VBF selections. Because it is inclusive, the use of this event shape would enable better control over theoretical uncertainties and may possibly lead to smaller theoretical uncertainties.

The purpose of this thesis is to analyze the properties of this event shape and its use in a simple cut-based analysis aiming at the measurement of the ratio of the VBF signal production cross section and the corresponding predicted value, i.e. the VBF signal strength. This includes also the computation of the theoretical uncertainty accompanying such a selection. While the described approach can be applied to all Higgs decay modes, this work is an analysis in the $H \to \gamma\gamma$ decay channel.

The outline of the thesis is:

- In the next part, the theoretical foundations will be introduced. Beside the Standard Model of particle physics also the estimation of theoretical uncertainties for the ggF contamination in a VBF selection will be explained.

- Subsequently, the ATLAS experiment will be described. This description includes the basics of the ATLAS detector as well as the analysis objects such as photons, tracks and jets.

- Following these theoretical and experimental fundamentals, the strategy and results of the analysis will be presented. These include the investigation of the properties of the 2-jettiness in interplay with the ATLAS detector and the event shape's utility in the creation of a VBF-enriched selection. The theoretical uncertainties, which depend on the selection, will be estimated. In the end, a computation of the VBF signal strength using a VBF selection based on the 2-jettiness is performed using 8 TeV ATLAS data.

1 Theoretical foundations

1.1 The Standard Model of Particle Physics

1.1.1 Preface

The Standard Model is the underlying theory of particle physics and is a quantum field theory. Gravitation is the only known force which is not part of the Standard Model: The Standard Model describes the *electromagnetic*, the *weak* and the *strong* force. These three forces are described by a gauge theory [6]. In the Standard Model, forces correspond to the exchange of vector bosons, while matter consists of fermionic particles. In addition to fermions and vector bosons, a scalar field exists, which is called *Higgs* field and is the source of mass of elementary particles.

The particles of the Standard Model can be divided into fermions and bosons. Fermions are particles with half-integer spin, while bosons are particles with integer spin. Not counting the antiparticles, 12 different elementary fermions are known to exist. These 12 fermions include six quarks and six leptons. Quarks are subject to the strong force, to the weak force and to the electromagnetic force. Leptons on the other hand interact only via the electroweak interaction. The group of leptons can be subdivided into two types: One lepton type is called neutrino and carries only weak charge. The other type of leptons carries weak charge and is in addition electrically charged with an electrical charge whose magnitude is equal to the charge of the electron. Of both types there are each three different kinds of leptons with differing masses. The same subdivision applies also to quarks. Up-type quarks are charged with $+2/3\,e$, while down-type quarks carry charge $-1/3\,e$. Thus, both leptons and quarks fermions can be grouped into three *generations*, each generation comprising two quarks and two leptons, see table 1[1]. The neutrinos, denoted by ν, are very light particles with masses less than $2\,\mathrm{eV}$ [6]. The corresponding charged leptonic partner of each neutrino is heavier. Among quarks there is the most massive known elementary particle, i.e. the top quark [7]. The fermion masses range over 11 orders of magnitude. The electromagnetic force is a long-range force, whereas the weak

---

[1] In this thesis, *natural* units are used, i.e. the speed of light and the reduced Planck constant are set to unity, $c = 1$ and $\hbar = 1$.

Generation	I	II	III
Leptons	$\nu_e\big\lvert^{0}_{<2\,\mathrm{eV}}$	$\nu_\mu\big\lvert^{0}_{<2\,\mathrm{eV}}$	$\nu_\tau\big\lvert^{0}_{<2\,\mathrm{eV}}$
	$e\big\lvert^{-1}_{0.5\,\mathrm{MeV}}$	$\mu\big\lvert^{-1}_{0.1\,\mathrm{GeV}}$	$\tau\big\lvert^{-1}_{1.8\,\mathrm{GeV}}$
Quarks	$u\big\lvert^{+1/3}_{2\,\mathrm{MeV}}$	$c\big\lvert^{+1/3}_{1.3\,\mathrm{GeV}}$	$t\big\lvert^{+1/3}_{173\,\mathrm{GeV}}$
	$d\big\lvert^{-2/3}_{5\,\mathrm{MeV}}$	$s\big\lvert^{-2/3}_{95\,\mathrm{MeV}}$	$b\big\lvert^{-2/3}_{4.2\,\mathrm{GeV}}$

TABLE 1: Fermionic particle content of the Standard Model. The superscript numbers give the electric charge in units of the elementary charge while the subscripts give the particle mass [7].

force is very limited in its range of action[2]. This difference in range is due to differing masses of the force carriers, the gauge bosons. The gauge boson of electromagnetism is called photon and denoted by γ, those of the weak force are denoted with $W^{\pm}$ and Z^0 and the exchange particles of the strong force are called gluons. The strong force is a short-range force as well, but for another reason than for the weak force: The force carriers of the strong force, the gluons, are massless just like photons. Due to the self-interaction of gluons, which produces a phenomenon called *confinement*, gluons cannot penetrate the space as photons do [8]. Gauge bosons are vector bosons, meaning that they carry unit spin. Scalar particles, which carry zero spin, are another kind of bosons, of which so far only one instance is known: the Higgs boson. The Higgs boson is a particle which is a consequence of the Higgs mechanism, which is an essential part of the Standard Model. Without the Higgs boson, masses of elementary particles would be forbidden by gauge invariance, which will be discussed in the following.

1.1.2 Interactions in the Standard Model

Interactions in the Standard Model are mathematically described and interpreted by means of particular symmetry groups [8]. These symmetry groups are groups of transformations which can be parametrized by one or more continuous real-valued variable(s)[3] [9]. The interactions are a result of the requirement that certain local symmetries with respect to transformations of fields

---

[2]Two weakly charged particles ought to be in a distance of about 10^{-18} m in order to have an interaction strength comparable to the electromagnetic force.

[3]Therefore they are called *continuous*. *Discrete* symmetry transformations can be defined as well, but they are not sources of forces. An example for a continuous group is the group of rotations in 3-dimensional space. These transformations are specified by three numbers. For further reading, see *Lie groups* [9].

ψ hold: Certain independent, continuous transformations at each point in spacetime are required to leave the Lagrangian of the system invariant. Local symmetries have to be distinguished from global symmetries; the transformations related to the latter are the same for all spacetime points, while in the former case at each spacetime point an independent choice of the transformation's parameter is allowed. Local symmetries are a centerpiece of gauge theory. The symmetries of the Standard Model are of the type $SU(N)$ – this means that they can be represented by unitary $n \times n$ matrices with determinant 1. A generic element of such a symmetry group acting on a field with n components $\psi(x) = (\psi_1(x), \psi_2(x), ..., \psi_n(x))$ can be written as

$$\psi(x) \rightarrow \exp(ig\alpha^i T^i)\psi(x). \tag{1}$$

Here, α^i are the components of a n-dimensional vector containing real numbers and the T^i are the *generators* of the symmetry group[4]. When $n > 1$, the order in which multiple transformations are applied, does generally matter. In this case, the symmetry group is called non-Abelian, opposed to the notion of Abelian groups, whose elements may be exchanged in a series of transformations without affecting the series' result.

The symmetry group which constitutes the Standard Model is [10]

$$SU(3)_C \times SU(2)_L \times U(1)_Y. \tag{2}$$

This symmetry group consists of one Abelian ($U(1)_Y$) and two non-Abelian gauge groups $SU(3)_C$ and $SU(2)_L$. The number of gauge bosons connected to a given symmetry $SU(N)$ is given by $N^2 - 1$. Hence, the existence of a $SU(2)_L \times U(1)_Y$ symmetry leads to four $((2^2 - 1) + 1 = 4)$ corresponding gauge bosons[5] (W_i^μ, $i = 1, 2, 3$ and B^μ) whereas the gauge group $SU(3)_C$ results in 8 different gauge bosons called gluons. The way how the leptons and quarks have been arranged in doublets in each generation in table 1, reflects the fact that interactions with a charged weak gauge boson transforms a particle into the other particle of the doublet: an electron turns into a neutrino or vice versa and an up-type quark into a down-type quark or vice versa[6]. If no additional mechanism like the Higgs mechanism would be assumed, the gauge bosons

---

[4]The generators of a given group are a subset of the group with the property that every element of the group can be accessed by a linear combination of the subset's elements and their inverses.

[5]For the sake of readability, the dependence on the spacetime is mostly not explicitly written in the following.

[6]The mass eigenstates are not the interaction eigenstates. This means that, to a small degree, there are transitions

have to be massless for reasons of gauge symmetry. The reason for this is that not only fermion fields undergo local gauge transformations but also gauge fields. In the presence of explicit gauge-boson mass terms in the Lagrangian, the transformation of the gauge fields would not leave the Lagrangian unchanged. Therefore the symmetry, for which the gauge field has been introduced in the first place, would be explicitly broken. Hence, massive gauge bosons cannot comply with the gauge principle if the model which so far contains only fermions and gauge bosons would not be extended. However, there are gauge bosons which are massive. Fermions are massive as well, and this as well would be forbidden in a model which does not include any mechanism that can give fermions a mass without explicitly breaking the gauge symmetry, as will be detailed in section 1.1.3.

A Lagrangian which is locally invariant under a given symmetry transformation must be globally invariant under the same symmetry transformation. Resulting from this global symmetry, a conserved quantity exists[7]. For the $U(1)_Y$ symmetry, the conserved quantity is called *weak hypercharge* and is denoted by Y; the conserved quantity of $SU(2)_L$ is one component of the *weak isospin*, commonly chosen as the *z*-component. In strong interactions ($SU(3)_C$), the conserved charge is called *color* [8].

In order to obtain an interacting theory, one takes the non-interacting and globally invariant Lagrangian as a starting point and replaces the partial derivatives ∂_μ with *covariant derivatives* D_μ, which depend on the considered symmetry group. In addition, one has to add kinetic terms for the gauge fields in order to take all the energetic content of the theory into account. The resulting Lagrangian includes interactions between fermionic fields and gauge fields, and in case of non-Abelian symmetry groups also interactions between the gauge fields themselves.

1.1.3 Theory of Electroweak Interactions and the Higgs Mechanism

In this section, only the $SU(2)_L \times U(1)_Y$ part of the Standard Model group (2) is considered, since the $SU(3)_C$ symmetry has no direct connection with the mechanism of *electroweak symmetry breaking*. The electromagnetic and the weak force can be unified to the *electroweak* force. This unification is manifest in the mixing of $SU(2)_L$ and $U(1)_Y$ gauge fields. By these symmetries,

---

between different generations, i.e. some weak interactions can transform a fermion mass-eigenstate of a given generation into a fermion mass-eigenstate of another generation.

[7]See Noether's theorem, e.g. [8].

four gauge fields are introduced: W_μ^i, $i = 1, 2, 3$ and B_μ. These result in four mass eigenstates which are combinations of the original gauge fields: W_μ^+, W_μ^-, Z_μ^0 and γ_μ. The conserved charges of $SU(2)_L$ and $U(1)_Y$ are one component of the weak isospin T_z and the weak hypercharge Y, respectively. The subscript L in $SU(2)_L$ indicates that only the left-handed fermion doublets are subject to the interaction corresponding to the $SU(2)_L$ gauge group, i.e. the weak force. The right-handed component of a fermion field transforms as a singlet, which means that they are not participating in the interaction [8]. The gauge field quantum γ is the massless photon, which carries no kind of charge. The two $W^\pm$ bosons carry electric charge, while the Z^0 boson is electrically neutral. The two charged gauge bosons $W^\pm$ carry in addition non-vanishing weak isospin: $T_z W_\mu^+ = +1 W_\mu^+$ and $T_z W_\mu^- = -1 W_\mu^-$. All left-handed fermions are weakly charged; the upper (neutrinos or up-type quarks) and lower component (charged leptons or down-type quarks) of a doublet has z-component of weak isospin of $+1/2$ and $-1/2$, respectively. An interaction of a fermion with a charged weak gauge boson is accompanied with a change of the fermion's third component of the weak isospin. This corresponds for example to the conversion of an electron to a neutrino or vice versa. The electric charge is related to the z-component of the weak isospin and the weak hypercharge via the equation $eQ = e(T_z + Y)$ [8]. The covariant derivative of the symmetry group $SU(2)_L \times U(1)_Y$ is

$$
\begin{aligned}
D_\mu &= \partial_\mu + i\frac{g}{2}\sigma^i W_\mu^i + ig'\frac{Y}{2}\hat{B}_\mu \\
&= \partial_\mu + \frac{i}{2}\begin{pmatrix} gW_\mu^3 + g'B_\mu & g(W_\mu^1 - iW_\mu^2) \\ g(W_\mu^1 + iW_\mu^2) & -gW_\mu^3 + g'B_\mu \end{pmatrix},
\end{aligned}
\tag{3}
$$

where the σ_i denote the three Pauli matrices. The coupling constants for the $SU(2)_L$ and $U(1)_Y$ gauge interactions are denoted by g and g', respectively. Thus, the matrix elements which act on the fermionic fields are linear combinations of the basic fields W_μ^i and B_μ. Therefore, it is

convenient and useful to define physical fields according to the following definitions:

$$W_\mu^\pm = \frac{1}{\sqrt{2}}(W_\mu^1 \mp W_\mu^2)$$

$$Z_\mu^0 = \frac{1}{\sqrt{g^2 + g'^2}}(gW_\mu^3 - g'B_\mu)$$

$$A_\mu = \frac{1}{\sqrt{g^2 + g'^2}}(gW_\mu^3 + g'B_\mu). \tag{4}$$

So far, all involved particles, fermions as well as bosons, have to be considered as massless, since otherwise gauge invariance would be lost. Because massive elementary particles are known to exist, a remedy is needed – which can be obtained by the assumption of a Higgs field. The resulting dynamical creation of particle masses is called Higgs mechanism. It bases on the assumption that a weak isospin doublet of a complex scalar field with non-vanishing vacuum expectation value v of the form as shown in the following equation exists.

$$\phi = \begin{pmatrix} \phi^+ \\ \phi^0 \end{pmatrix} = \frac{1}{\sqrt{2}} \begin{pmatrix} \phi_1 + i\phi_2 \\ \phi_3 + i\phi_4 \end{pmatrix}. \tag{5}$$

The weak hypercharge Y of the Higgs doublet is $Y = +\frac{1}{2}$ [8]. This Higgs field is described by a Lagrangian (6) that leads to *spontaneous symmetry breaking*, which corresponds to the dynamical generation of mass [8]:

$$\mathscr{L}_\phi^{\text{free}} = \partial_\mu \phi^\dagger \partial^\mu \phi - V(\phi)$$

$$= \partial_\mu \phi^\dagger \partial^\mu \phi + \mu^2 \phi^\dagger \phi - \lambda(\phi^\dagger \phi)^2. \tag{6}$$

The parameters μ^2 and λ are real parameters; both must be chosen positive if a stable vacuum state is required. With these signs of λ and μ^2, the potential of the Higgs field looks as shown in figure 1. There is not only one ground state but a four-dimensional circle with radius $\frac{v}{\sqrt{2}} = \frac{\mu}{\sqrt{2\lambda}}$, containing a continuum of ground states. The Lagrangian in (6) is symmetric under $SU(2)_\text{L} \times U(1)_\text{Y}$ transformations, but from the perspective of one of the ground states, that symmetry is hidden. This situation has an analog in solid state physics: While inside a
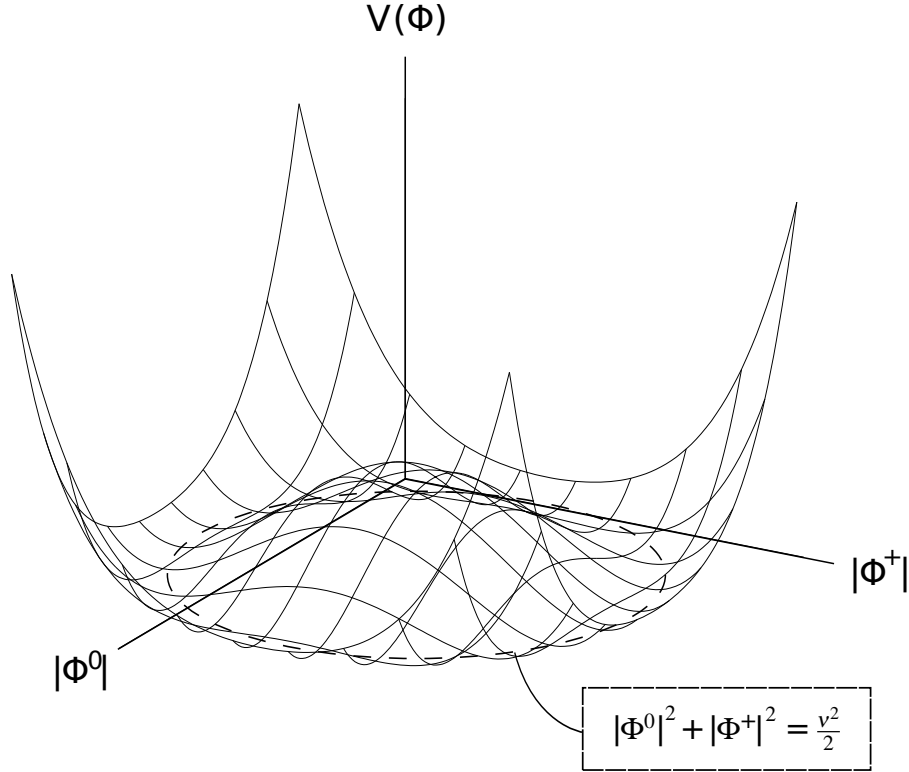
FIG. 1: The Higgs potential as a function of the field strength. For the sake of the presentation, the Higgs potential is drawn as a function of only two of the four real-valued Higgs field components.

ferromagnet the system appears to be not rotationally invariant[8], this does not mean that the general physical laws ruling the world have to favor one special direction. If one would increase the ferromagnet's temperature above the Curie temperature[9], the rotational symmetry would be manifest in the ferromagnet, too.

In order to make meaningful statements about the particle spectrum in a world being in the ground state, one has to assume the ground state in calculations as well. The Lagrangian of the Higgs fields ϕ is invariant under $SU(2)_L \times U(1)_Y$ transformations, but the ground state is not. Assuming the ground state corresponds here to the reduction of the $SU(2)_L \times U(1)_Y$ symmetry to a $U(1)_{EM}$ symmetry, which is the symmetry group of the electromagnetic force. The Higgs field doublet can be gauged in a way which leads to only one real-valued and non-vanishing

---

[8]In a ferromagnetic material atomic spins are aligned in a way that a particular direction is special; thus the rotational symmetry is broken.

[9]The Curie temperature denotes the temperature above which a ferromagnetic material has lost its ferromagnetic properties.

component, see equation (7). This particular gauge is called *unitary* [8].

$$\phi = \exp\left(i\frac{\theta_a}{2}\sigma_a + i\frac{\beta}{2}\right)\begin{pmatrix}\phi_1 + i\phi_2 \\ \phi_3 + i\phi_4\end{pmatrix} = \begin{pmatrix}0 \\ \phi_3\end{pmatrix}. \tag{7}$$

In the ground state, this becomes

$$\phi = \begin{pmatrix}0 \\ \frac{1}{\sqrt{2}}(v + H(x))\end{pmatrix}. \tag{8}$$

The vacuum expectation value of the Higgs field is denoted by v, and the dynamic variable is now denoted by $H(x)$. Quantized excitations of this scalar field $H(x)$ are called *Higgs bosons*. If one compares this expression with equation (5), one can see that the chosen ground state is electrically neutral, which means that photons are not interacting directly with the Higgs field and therefore are not acquiring mass via the Higgs mechanism.

In order to make the free Lagrangian of the Higgs field invariant under $SU(2)_L \times U(1)_Y$ transformations, one replaces the ordinary derivative ∂_μ with the covariant derivative D_μ, defined in equation (3):

$$\begin{aligned}\mathscr{L}_{\text{Higgs}} &= (D_\mu\phi)^\dagger(D^\mu\phi) + \mu^2\phi^\dagger\phi - \lambda(\phi^\dagger\phi)^2 \\ &= (\partial_\mu\phi)^\dagger(\partial^\mu\phi) + \mu^2\phi^\dagger\phi - \lambda(\phi^\dagger\phi)^2 \\ &\quad + \frac{1}{4}\phi^\dagger(gW_\mu^a\sigma^a + g'B_\mu)(gW_\mu^b\sigma^b + g'B_\mu)\phi.\end{aligned} \tag{9}$$

If now the Pauli matrices σ^a are evaluated and one assumes the ground state as defined in equation (8), equation (9) becomes

$$\begin{aligned}\mathscr{L}_{\text{Higgs}}^{\text{vac}} &= \frac{1}{2}(\partial_\mu H)^\dagger(\partial^\mu H) - \mu^2 H^2 - \lambda v H^3 - \frac{1}{4}\lambda H^4 \\ &\quad + \frac{1}{8}(v + H)^2\left(g^2((W_\mu^1)^2 + (W_\mu^2)^2) + (-gW_\mu^3 + g'B)^2\right).\end{aligned} \tag{10}$$

Exchanging the basic fields W_μ^i and B_μ with the mass eigenstates defined in equations (4) leads to the following gauge boson masses:

$$m_{W^\pm} = \frac{v\,g}{2}$$

$$m_{Z^0} = \frac{v\,\sqrt{g^2 + g'^2}}{2}$$

$$m_\gamma = 0 \tag{11}$$

As a consequence, one can compute the vacuum expectation value of the Higgs field if the mass of the $W^\pm$ boson is known via $v = 2\,m_{W^\pm}/g = 246\,\text{GeV}$ [7]. This scale is called the *electroweak scale*. There is a close relationship between the $W^\pm$ and the Z^0 mass:

$$\frac{m_{W^\pm}}{m_{Z^0}} = \frac{g^2}{\sqrt{g^2 + g'^2}}. \tag{12}$$

If one counts the degrees of freedom before the spontaneous symmetry breaking and after, one obtains the following result: Before spontaneous symmetry breaking, one has four massless gauge fields, which relates to eight degrees of freedom[10] and in addition, the complex Higgs doublet gives four degrees of freedom. Thus, there are in total twelve degrees of freedom. After symmetry breaking, one has three massive gauge bosons and one massless gauge boson, which leads to $3 \cdot 3 + 2 = 11$ degrees of freedom in that part, while the Higgs field's strength can be expressed by one single number H. Thus, one has again twelve degrees of freedom. Three of the four degrees of freedom of the Higgs field ϕ have been converted into third degrees of freedom of the originally massless $W^\pm$ and Z^0 bosons, corresponding to them having become massive.

In addition to those gauge boson mass terms, the Lagrangian (10) includes interactions between the Higgs field and the gauge fields:

$$\mathscr{L}_{\text{int.}} = \frac{g^2}{4} H^2 (W_\mu^\pm)^2 + \frac{g^2}{2} H (W_\mu^\pm)^2 + \frac{g^2 + g'^2}{8} H^2 (Z_\mu^0)^2 + \frac{g^2 + g'^2}{4} H (Z_\mu^0)^2 \tag{13}$$

---

[10]Massless particles with spin 1 only have two possible polarizations, while massive particles have three.

The remaining part of the Lagrangian (10) describes the Higgs field kinematics and the Higgs field's self-interactions:

$$\mathscr{L}_H = \frac{1}{2}(\partial_\mu H)^\dagger (\partial^\mu H) - \frac{1}{2}m_H^2 H^2 - \frac{\lambda}{2}m_H H^3 - \frac{1}{4}\lambda H^4 \tag{14}$$

The mass of the Higgs field is $m_H = \sqrt{2}\,\mu$. Since μ is not known, the theory does not predict the mass of the Higgs boson. The terms proportional to H^3 and H^4 correspond to self-interactions of the Higgs field.

A convenient way to allow for fermion masses is to assume a *Yukawa* coupling[11] between the Higgs field and fermion fields. An explicit fermion mass-term of the form

$$m\bar{\psi}\psi = m\,(\psi_L^\dagger \psi_R + \psi_R^\dagger \psi_L) \tag{15}$$

in the Lagrangian of fermions would violate gauge invariance [8]. This is because left- and right-handed components transform differently under gauge transformations. A Yukawa coupling of the Higgs field to fermions, however, leads to fermion mass generation preserving gauge invariance. For example, an electron mass term can be generated by introducing a Lagrangian term [8]

$$\mathscr{L}_{\text{Yukawa}}^e = -\lambda_e\,(\bar{E}_L\,\phi\,e_R + \bar{e}_R\,\phi^\dagger E_L). \tag{16}$$

In this equation the left-handed $SU(2)$ doublet which contains the electron and electron-neutrino is denoted by

$$E_L = \begin{pmatrix} \nu_e \\ e^- \end{pmatrix}_L. \tag{17}$$

The right-handed electron singlet in $SU(2)_L$ is denoted by e_R. The coupling strength between fermions and the Higgs field is given by λ_f, in this case λ_e. The Lagrangian (16) is a gauge-invariant expression. Assuming the vacuum state as chosen in equation (8), it becomes

$$\mathscr{L}_{\text{Yuk}}^e = -\lambda_e\,\frac{v}{\sqrt{2}}\,(\bar{e}_L\,e_R + \bar{e}_R\,e_L). \tag{18}$$

This expression is a proper mass term for a fermion, in this case an electron. Neutrinos have no

---

[11]A Yukawa coupling is a coupling of a scalar field to two fermions.

right-handed component in the Standard Model, hence a Dirac mass term (18) is zero. This means that neutrino masses are forbidden in the Standard Model. However, neutrinos are measured to be massive to a small extent. This problem is not yet resolved. A possible remedy for this situation could be to assume a completely non-interacting right-handed neutrino [7]. The same procedure as described above for the electron can be worked out for the other fermions. The mass for a fermion is in general given by

$$m_f = \frac{\lambda_f v}{\sqrt{2}}. \tag{19}$$

The coupling parameter λ_f are free parameters of the theory which means that no prediction of the fermion masses can be made. The coupling of the Higgs field to the fermionic fields increases with the mass of the fermion.

1.1.4 The Higgs Boson

The existence of a Higgs boson has been experimentally verified in July 2012 [1]. Since then, there have been efforts to measure its properties. The mass of the Higgs boson is measured by the ATLAS collaboration to be $m_H = 125.36 \pm 0.37 \, (\text{stat.}) \pm 0.18 \, (\text{syst.})$ GeV [11]. Since the decay into two gauge bosons has been observed, the Higgs particle itself must be a boson. Based on the fact that the decay into two photons has been observed, one can discard the hypothesis of a spin-1 particle[12]. The measurements so far indicate a spin of 0, which is also the predicted value [12]. Given the Higgs mass and the masses of the other particles, all couplings strengths to other Standard Model particles are predicted by theory. These coupling strengths between the Higgs boson and the other particles can be extracted from measurements of the Higgs boson's decay and production modes. Once a Higgs boson is produced, it is predicted to decay very quickly into subsequent particles. Decays into a pair of fermions, into a pair of gauge bosons as well as into pairs or triplets[13] of Higgs bosons are allowed. How quickly the Higgs boson decays, depends on the mass of the Higgs boson. The more decay modes are permitted by means of energy conservation, i.e. the heavier the Higgs boson is, the more quickly the Higgs boson

---

[12]It is impossible to construct a spin state with two photons with spin 1 originating from a particle with half-integer spin due to conservation of angular momentum.

[13]At the present integrated luminosity, the decay into pairs or even triplets of Higgs bosons is not a significant decay channel.

will decay. The relevant number here is the total decay width $\Gamma = \sum \Gamma_i$, where Γ_i denotes the partial decay width for the decay mode i. The total decay width is inversely proportional to the mean lifetime τ_H of the Higgs boson: $\Gamma_H = 1/\tau_H$. The expected decay width of the Higgs boson at the measured Higgs boson mass of 125.4 GeV is (4.12 ± 0.16) MeV [4]. Therefore, one can predict the Higgs boson's lifetime to be $\tau_H = 1.60 \cdot 10^{-24}$ s. The *branching ratios* of the Higgs decay channels are defined as [6]

$$B_i = \frac{\Gamma_i}{\Gamma}. \tag{20}$$

Figure 2 shows the branching ratios of the Higgs decay as a function of the Higgs mass. The branching ratios to the individual decay modes depend on the Higgs mass, as well as on the masses of the decay products. The Higgs tends to decay into the pair of particles which have the largest mass allowed by energy conservation at a given Higgs mass. But as one can see in figure 2, this energy conservation criterion does not hold exactly, which is due to the uncertainty principle $\Delta t \cdot \Delta E \geq 2\pi\hbar$. It means that the energy of a particle can vary to some extent for a certain time. In effect, the Higgs boson can decay via a certain channel even if the Higgs mass is smaller than the mass of the real decay products. If such a decay occurs, some degree of *virtuality* of the resulting decay products must be present. Virtuality means that a given particle does not fulfill the energy-momentum relation $E^2 = \vec{p}^2 + m^2$. A virtual particle can only exist for a short period of time, after which it must have undergone some interaction or decay. The more virtual an intermediate state is, the more the energy-momentum relation is violated and the more suppressed the process is. This is why the branching fraction of a certain decay channel decreases quickly when one goes to lower Higgs masses than the invariant mass of the decay products. At the measured Higgs mass of 125.36 GeV, the decay into a pair of b and $\bar{b}$ quarks is most likely, since b quarks are the heaviest particles with a mass smaller than half of the Higgs mass. This is a somewhat unlucky situation for the experimenter, due to the large backgrounds of the $H \rightarrow b\bar{b}$ signature. The decays into massive and non-massive gauge bosons on the other side are the most important decay channels for the verification of the Higgs boson and in case of the decay into $\gamma\gamma$ or ZZ also for the mass measurement:
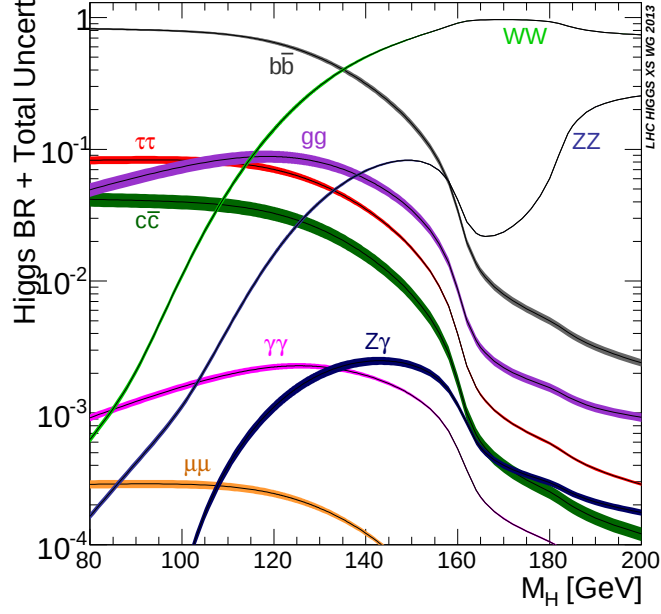
FIG. 2: The branching ratios of the Higgs boson as a function of the Higgs mass [4].

- $H \to \gamma\gamma$: This decay is predicted to have a small branching ratio of $(2.28 \pm 0.11) \cdot 10^{-3}$ at $m_H = 125.4\,\text{GeV}$ [4]. Still, it is a mode with high significance and the Higgs boson mass can be measured with high accuracy. Since photons do not carry mass, this decay must involve a loop of heavy charged particles between Higgs boson and the two outgoing photons, see figure 3. Since this is the decay mode most important for this thesis, it is worthwhile to give a few details about its experimental backgrounds: The fraction of Higgs events among all events which contain two photons is small. In most of these events, the two photons are produced in non-Higgs events such as quark-antiquark annihilations, which is an *irreducible* background. There are also contributions from hadrons or jets which have been misidentified as photons; those contributions are called *reducible* because, with increasing experimental abilities, these contributions can be more efficiently rejected.

- $H \to Z^0 Z^0 \to 4l$: This decay mode constitutes a so-called *golden channel*. It provides high sensitivity and good energy resolution. The branching ratio at $m_H = 125.4\,\text{GeV}$ is predicted to be $(2.74 \pm 0.11) \cdot 10^{-2}$ [4].

- $H \to W^+ W^- \to l^+ \nu l^- \bar{\nu}$: The branching ratio of $(2.21 \pm 0.09) \cdot 10^{-1}$ [4] of this decay channel is relatively high. Due to the decay of $W^\pm$ boson into a pair of quarks – a signature

15

which has a huge non-Higgs background – or into a leptonic final state containing a neutrino, the mass of the Higgs boson can not be measured directly in this channel.

Decays into fermions with low masses, i.e. those stemming from the first two generations, are very suppressed so that these decay channels are not significantly substantiated by the analysis which can be done with run 1 data.Nevertheless, it is important to measure the coupling of the Higgs boson also to those lighter fermions, since these measurements allow tests of the Standard Model predictions regarding the Higgs couplings.
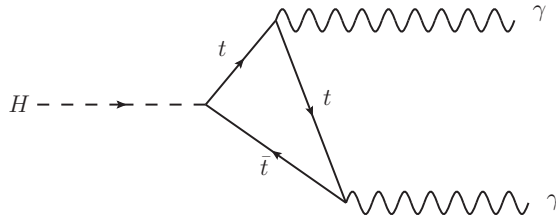

FIG. 3: Feynman diagram for the decay of a Higgs boson through a top quark loop into two photons. The particle in the loop can be any massive charged particle such as *W* bosons.

In figure 4, the five different production modes which are important at a hadron collider like the LHC are presented in form of Feynman diagrams.

- Gluon fusion (ggF): Two incoming gluons fuse into a loop of heavy quarks, which can produce an outgoing Higgs boson. Since the parton content of protons at high energies is made to a high degree of gluons, this mode is the dominant production mode, having at 8 TeV LHC operation a cross section of 19.2 pb at a Higgs mass of 125.4 GeV and at 8 TeV LHC operation. At leading order nothing but a Higgs boson is produced in this interaction. Through higher order corrections, additional jets can emerge. The properties of the gluon fusion process are controlled by *Quantum Chromodynamics*[14] (QCD) and therefore inherit the complications of QCD, see section 1.1.5.

- Vector boson fusion (VBF): Here, a heavy gauge boson is emitted by each of two incoming quarks. Those heavy bosons can fuse into a Higgs boson. The magnitude of the VBF cross section is an important measure for the coupling strength of electroweak gauge bosons to the Higgs boson. As experimental signature, one expects the Higgs boson accompanied

---

[14]This topic is treated in section 1.1.5

by two jets in the forward region, which originate from the scattered quarks. Between these jets, little additional radiation is expected. Vector boson fusion is predicted to be a subdominant production mode, having a production cross section at 8 TeV of 1.65 pb.

- Associated vector-boson production (WH and ZH): A $W^{\pm}$ or Z^0 boson emits a Higgs boson. The production cross sections for these modes are 0.70 pb and 0.41 pb, respectively.

- ttH: Here, two incoming gluons split up into each a pair of top quarks[15]. Two oppositely-charged top quarks can couple to a Higgs boson. Thus, in the final state a Higgs boson as well as two top quarks of opposite charge can be measured. The production cross section for this process is 0.13 pb.
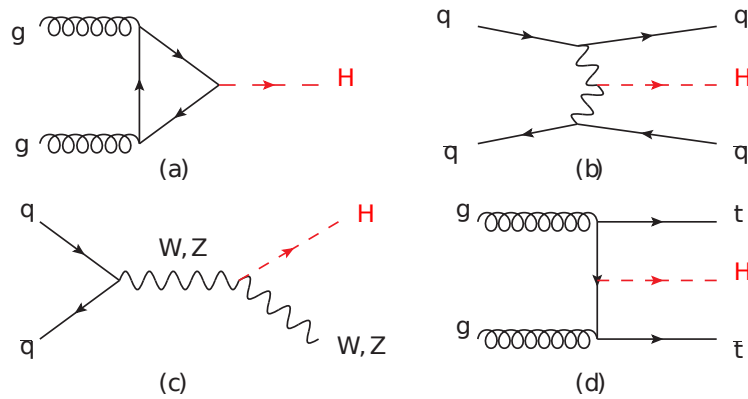

FIG. 4: The leading Feynman diagrams for the five leading Higgs production modes. a) Gluon fusion, b) Vector boson fusion, c) Associated vector-boson production, d) Higgs boson production in association with $t\bar{t}$ pairs [7].

1.1.5 Quantum Chromodynamics

Quantum Chromodynamics is the theory of strong interactions and is based on the $SU(3)_C$ gauge group [8]. A quark is a fermion which interacts via the strong force. A quark can have three different $SU(3)_C$ charges. These charges are called *red*, *green* and *blue* – the C in $SU(3)_C$ stands for color. Corresponding to the fact that this gauge group is non-Abelian, the gluon, which is the transmitter of the strong force, carries color charge itself and therefore interacts with other gluons. There are eight types of gluons, carrying different combinations of colors and anti-colors. Therefore, quarks can change their color by interacting with gluons.

---

[15]Of course, also $b\bar{b}H$ or $c\bar{c}H$ may occur, but such modes are expected to be considerably less significant, because of the large backgrounds of the corresponding event signatures.

At different distance scales, or equivalently at different momentum-transfer scales, the coupling parameter of an interaction has different magnitudes. This property is called *running*. The coupling parameter α_{EM} of electromagnetism is decreasing at increasing distances. The opposite holds for the strong interaction, which leads to very different phenomena as observed in electromagnetism; the strong interactions comprises effects such as confinement or *asymptotic freedom*, which will be described below. In the following equation, the running of the QCD coupling strength is given in lowest order of perturbation theory:

$$\alpha_{\text{s}} \approx \frac{2\pi}{\left(11 - \frac{2}{3}N_f\right)\ln\left(\frac{Q}{\Lambda}\right)}. \tag{21}$$

Here, N_f is the number of quark flavors, which is 6, and Λ is the scale at which the strong coupling constant becomes large when the momentum transfer Q is lowered. The scale Λ is of order $\Lambda \approx 0.1\,\text{GeV}$ to $0.5\,\text{GeV}$ [10]. Light hadrons are roughly of the size $1/\Lambda \approx 10^{-14}\,\text{m}$. At the same time, the lightest mesons, i.e. pions, have a mass in the same range as Λ. Perturbation theory can only be applied if Q is larger than about $1\,\text{GeV}$, which corresponds to α_{s} being smaller than approximately 0.4, since the convergence of the series is not given otherwise.

No colored objects such as single quarks or gluons can be measured in a detector: If one tries to separate a colored object from a hadron, the force between the colored particle and the remaining rest of the hadron will *increase* with increasing separation[16] – the result of this is that the colored particle which was meant to be isolated is not a colored object anymore but has been joined together with other colored particles from the vacuum into a new, color-neutral state. An illustration of this process called *hadronization* can be the following: The increasing force between the two colored objects in the process of separation leads to such a high energy density that new quarks come into existence between them. These make new bonds with the original colored particles, and hence all particles are color-neutral again in the final state. Due to the large distance scales involved in hadronization, this process is not computable by perturbative QCD calculations. Processes which are happening at small distances or high energies, for example a collision of two partons with sufficiently high momentum transfer at the LHC can be computed

---

[16]Note that in Quantum Electrodynamics, the theory of electromagnetism, the opposite holds: The more one separates two electrically charged objects, the weaker the force between them will be.

without problems in perturbation theory, because the coupling strength of QCD is in that case small enough to let the perturbation series converge.

To compare theory predictions and experimental results involving QCD physics, one has to measure quantities which are *infrared-safe*. This means that the quantity must not depend on low-energy or large-distance processes (e.g. an emission of a soft gluon from a hadronizing gluon or quark) but only on short-distance processes. If that is the case, such a quantity can be computed in perturbative QCD. There are of course processes which depend on soft QCD physics. *Factorization* is a technique which makes it possible to compute such processes as well: A quantity which depends on a hard process as well as on a soft process can be computed by separating the two energy scales. Perturbative QCD is used to compute the hard process. By using factorization, a scale called *factorization scale* is introduced. Physics below this scale is treated as part of the internal interactions within the proton, which are described by the parton density functions, while a process with an energy above this scale enters the scattering cross section as hard interaction.

1.2 Theoretical Uncertainty on the Gluon Fusion Cross Section in Vector Boson Fusion Selections

1.2.1 Preface

A goal of this thesis is to compare the number of measured VBF events with the predicted number of VBF events in order to test of the Standard Model prediction. A simple way[17] to do this measurement is via the equation

$$N_{\mathrm{VBF}} = N^{\mathrm{sel.}} - N_{\mathrm{bkg}}^{\mathrm{fit}} - N_{\mathrm{H,non-VBF}}^{\mathrm{SM}}, \tag{22}$$

where $N^{\mathrm{sel.}}$ is the number of selected events, $N_{\mathrm{bkg}}^{\mathrm{fit}}$ is the number of non-Higgs background events which is obtained on basis of data, and $N_{\mathrm{H,non-VBF}}^{\mathrm{SM}}$ is the number of non-VBF Higgs events which is predicted by the Standard Model. Because of the relatively large cross section of gluon

---

[17]In the official $H \to \gamma\gamma$ couplings analysis [2], a more sophisticated method is used to extract the signal strengths. It is outlined in subsection 3.5.2

fusion, which is about one order of magnitude larger than the cross section of vector boson fusion [4], the number of gluon fusion events in the selection must be considered with great care.

For this measurement of the number of VBF events, it is advantageous to use a selection which mostly contains VBF events. As described in section 1.1.4, VBF events have two forward jets and only little additional hadronic radiation. For a VBF selection it would be therefore useful to require two jets with little additional central radiation in between. However, also gluon fusion events can be accompanied by two jets through initial-state gluon radiation, corresponding to higher-order corrections in the perturbation expansion. Since gluon fusion is predicted to have a relatively large cross section, it is important to know how large the gluon fusion contribution to the VBF-enriched selection is and with which precision this contribution can be predicted. The uncertainty on this prediction, i.e. the theoretical uncertainty on the gluon-fusion contribution to VBF selections, is the topic of this section.

The two main types of theoretical uncertainties are perturbative uncertainties and parametric uncertainties; examples for the latter are uncertainties on the parton distribution function [13] or on the magnitude of α_s. In this treatment of theoretical uncertainties, only the perturbative uncertainty is addressed. In contrast to parametric uncertainties, they depend on the phase space restrictions imposed by the event selection. Perturbative uncertainties are resulting from usage of incomplete perturbation expansions in cross section calculations. A typical inclusive cross section of a process involving the strong interaction has the form

$$\sigma = \sigma_B \sum_{i=0}^{\infty} c_i(\mu, Q)\, \alpha_s^i(\mu, Q), \tag{23}$$

where σ_B denotes the *Born-level* cross section[18] of the process in question, μ is an scale called the *renormalization scale*, which would not have any effect on the result if all orders of perturbation theory would be considered, and Q is the energy scale of the interaction. In practice, and in particular in case of QCD calculations, only a finite and often not particularly large number of terms can be taken into account, because only some of the factors c_i could be computed so far.

The influence of unknown higher order terms in the perturbative expansion in the calculation of a given cross section must be estimated in some way, and the magnitude of this influence is taken as an estimate of the perturbative uncertainty. The impact of these missing terms is usually

---

[18]Born level cross sections are cross sections computed at lowest possible order in perturbation theory.

estimated using variations[19] of certain energy scales around a central value [13]: the factorization scale μ_F and the renormalization scale μ_R. The strong coupling constant α_s is scale-dependent, as mentioned in subsection 1.1.5. The calculation of the coupling strength at a given scale Q can so far only be done to finite order in perturbation theory, which entails that α_s depends on the scales μ_F and μ_R. The central value is commonly chosen to be the scale of the hard interaction; in case of Higgs production it would be the mass of the Higgs boson.

1.2.2 Definition of an Exclusive 2-Jet Cross Section

The splitting of the cross section into parts with restrictions on the number if jets, i.e. the creation of *jet bins*, can be useful to concentrate the analysis on phase space regions in which the signal (VBF, in this case) sensitivity is especially high, that is, in which is comparatively little background compared to the number of signal events. With a jet reconstruction algorithm one can define the inclusive 2-jet cross section $\sigma_{\geq 2}$, which contains all events with at least two reconstructed jets. It is useful for a VBF selection to select only events whose configuration is close to the VBF Born-level diagram, i.e. events which contain not more than two outgoing jets and the Higgs boson's decay products. Thus, it is useful to further constrain the cross section, i.e. to define an *exclusive* 2-jet cross section, using the relation:

$$\sigma_{\geq 2} = \sigma_2 + \sigma_{\geq 3} \tag{24}$$

Here, one divides the inclusive 2-jet cross section into an exclusive 2-jet cross section and an inclusive 3-jet cross section. One has to define the exact definition of *exclusive* in terms of an appropriate observable k which should measure the radiation which occurs in addition to the two signal jets and the Higgs decay products. Then, the exclusive 2-jet cross section can be defined as follows:

$$\sigma_2(k < k^{\text{cut}}) = \sigma_{\geq 2} - \sigma_{\geq 3}(k > k^{\text{cut}}). \tag{25}$$

---

[19]The reliability of this approach is not guaranteed, but in many cases it leads to sensible results: Given an estimate of the influence of higher-order corrections at a given order in α_s, e.g. at leading order, one can check at the transition to the next order in α_s (in this example: next-to-leading-order (NLO)) whether the NLO prediction is contained within the uncertainty band estimation based on the leading-order (LO) calculation. Such a case speaks in favor of this procedure.

This can be expressed in terms of integrals over a differential cross section in the variable k:

$$\sigma_{\geq 2} = \int_0^{k_{\text{cut}}} \mathrm{d}k \, \frac{\mathrm{d}\sigma_{\geq 2}}{\mathrm{d}k} + \int_{k_{\text{cut}}}^{\infty} \mathrm{d}k \, \frac{\mathrm{d}\sigma_{\geq 2}}{\mathrm{d}k} \tag{26}$$

Entailed by the splitting of the inclusive 2-jet inclusive into an exclusive 2-jet cross section and an inclusive 3-jet cross section, a large perturbative uncertainty of the exclusive 2-jet cross section and the inclusive 3-jet cross section of ggF can appear, depending on how restrictive the selection is. The tighter[20] the restriction on the additional radiation, the larger those uncertainties become. To be more specific: By cutting off infrared divergences in real-emission diagrams, *Sudakov double-logarithms* are introduced in each order of the perturbation series. These logarithms have the form

$$L(k^{\text{cut}} =) \alpha_{\text{s}}^n \ln^m \left(\frac{k^{\text{cut}}}{Q} \right), \qquad \text{with } m \leq 2n. \tag{27}$$

The hard scale Q is given by the Higgs mass m_H. The exclusive 2-jet cross section and inclusive 2-jet and 3-jet cross sections schematically look like [14]

$$
\begin{aligned}
\sigma_{\geq 2} &\approx \sigma_{\text{B}} \left[c_1 + c_2 \, \alpha_{\text{s}} + c_3 \, \alpha_{\text{s}}^2 + \cdots \right], \\
\sigma_{\geq 3} &\approx \sigma_{\text{B}} \left[c_2' \, \alpha_{\text{s}} \left(d_1 L^2 + d_2 L + d_3 \right) + c_3' \alpha_{\text{s}}^2 \left(d_4 L^4 + d_5 L^3 + d_6 L^2 + d_7 L + d_8 \right) + \cdots \right], \\
\sigma_2 &= \sigma_{\geq 2} - \sigma_{\geq 3} = \sigma_{\text{B}} \left\{ c_1 + \alpha_{\text{s}} \left[c_2 - c_2'(d_1 L^2 + d_2 L + d_3) \right] \right. \\
&\quad \left. + \alpha_{\text{s}}^2 \left[c_3 - c_3' \left(d_4 L^4 + d_5 L^3 + d_6 L^2 + d_7 L + d_8 \right) \right] + \mathcal{O}(\alpha_{\text{s}}^3) \right\}.
\end{aligned}
\tag{28}
$$

The effect of the logarithms in this equation on the selected gluon fusion cross section can be seen in figure 5. The cross section is shown as function of cuts on $\pi - \Delta\phi_{H-jj}$ for different choices of the factorization- and renormalization scale, which, for simplicity, have been chosen to be $\mu_{\text{R}} = \mu_{\text{F}} = \mu$. The variable $\Delta\phi_{H-jj}$ is a measure for additional radiation in events with at least two jets[21] and defined as [14]

$$\frac{(\vec{p}_{\text{T},j1} + \vec{p}_{\text{T},j2}) \cdot \vec{p}_{\text{T},H}}{|\vec{p}_{\text{T},j1} + \vec{p}_{\text{T},j2}| \cdot |\vec{p}_{\text{T},H}|}, \tag{29}$$

---

[20]In this case, *tight* means that only events close to the VBF Born configuration are selected, i.e. a restrictive veto on additional jets in the central region is applied.

[21]*Additional radiation* means in this context radiation that is not contained in the two jets with the highest transverse momentum.

where $\vec{p}_{T,H}$ is the transverse momentum of the Higgs boson. The transverse momentum of the jet with the largest and second-largest transverse momentum is denoted with $\vec{p}_{T,j1}$ and $\vec{p}_{T,j2}$, respectively. Due to the conservation of transverse momentum, $\Delta\phi_{H-jj}$ would be equal to π if the Higgs boson and the two jets are the only final-state objects of the interaction[22]. If, however, there would be a third jet, it would make itself noticeable by decreasing the value of $\Delta\phi_{H-jj}$. By cutting on this variable, one divides the cross section into an effective exclusive 2-jet cross section σ_2, containing the events close to the VBF-Born configuration, and an effective inclusive 3-jet cross section $\sigma_{\geq 3}$ which contains the events with a $\pi - \Delta\phi_{H-jj}$ larger than a given value.

The tighter the cut, i.e. the closer $\Delta\phi_{H-jj}$ is to π, the smaller the selected number of gluon fusion events is. At some point, the calculated cross section is becoming negative, which is evidence for perturbation theory breaking down: If also very small emissions are vetoed, soft QCD gets important. But as already mentioned in subsection 1.1.5, that regime of QCD is not described by perturbation theory.
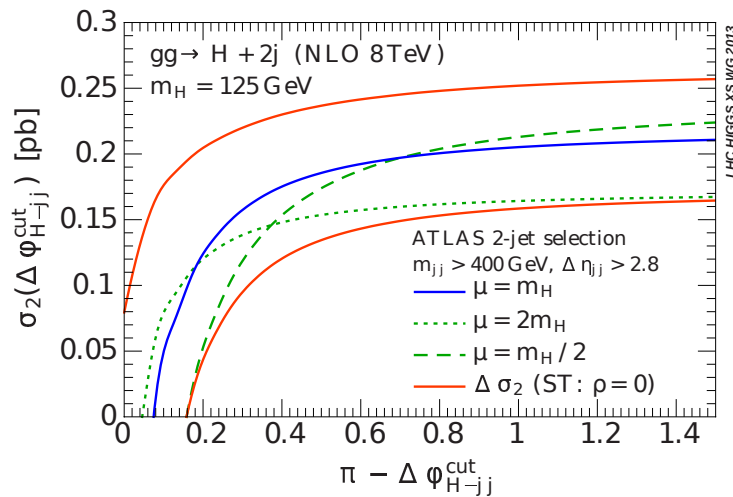

FIG. 5: Predicted selected ggF cross sections for different scales, with $\mu = \mu_R = \mu_F$. [14].

1.2.3 The Stewart-Tackmann Method

After splitting the inclusive 2-jet cross section into the 2-jet-exclusive and the 3-jet-inclusive part, one is interested in the covariance matrix of the new system of variables σ_2, $\sigma_{\geq 3}$. This

---

[22]The Higgs boson and the dijet system would be scattered of back-to-back, corresponding to an angle of π between them.

covariance matrix is a 2×2 matrix and can be parametrized as follows [14][15]:

$$C = \begin{pmatrix} (\Delta_2^y)^2 & \Delta_2^y \Delta_{\geq 3}^y \\ \Delta_2^y \Delta_{\geq 3}^y & (\Delta_{\geq 2}^y)^2 \end{pmatrix} + \begin{pmatrix} (\Delta^{\mathrm{cut}})^2 & -(\Delta^{\mathrm{cut}})^2 \\ -(\Delta^{\mathrm{cut}})^2 & (\Delta^{\mathrm{cut}})^2 \end{pmatrix} \tag{30}$$

The first matrix describes the uncertainty on the yield; it is 100 % correlated between the two jet bins. The sum of the yield uncertainties on the exclusive and inclusive cross section gives the uncertainty on the inclusive 2-jet cross section:

$$\Delta_{\geq 2} = \Delta_{\geq 2}^y = \Delta_2^y + \Delta_{\geq 3}^y. \tag{31}$$

The second matrix parametrizes the uncertainty on the migration between the two bins. This uncertainty is 100 % anti-correlated between the two inclusive and exclusive cross section; thus the migration uncertainty disappears when the two bins are added, i.e. when the inclusive 2-jet cross section is considered. It follows from equation (30) that

$$\Delta_2^2 = (\Delta_2^y)^2 + (\Delta^{\mathrm{cut}})^2$$
$$\Delta_{\geq 3}^2 = (\Delta_{\geq 3}^y)^2 + (\Delta^{\mathrm{cut}})^2. \tag{32}$$

The migration uncertainty is directly related to the presence of Sudakov logarithms, which are introduced by the separation into an inclusive and exclusive part of the cross section. Those logarithms are large at tight selections, so that the α_{s} suppression of higher orders in α_{s} may be overpowered. Thus, large Sudakov logarithms would have impact on the unknown higher-order contributions, leading to enhanced uncertainties. The difference between the two dotted lines in figure 28 is corresponding to the uncertainty obtained from plain scale variations, not taking into account the effect of the logarithms. At intermediate cut values, this uncertainty vanishes completely, which is unsatisfactory, but expected if one looks at equation (5): It is conceivable that at some value of $L(k^{\mathrm{cut}})$ the factors which accompany powers of α_{s} vanish. Thus, the vanishing uncertainty from scale-variations is due to the compensation of logarithmic terms with non-logarithmic terms. But if such coefficient is zero, variations in α_{s} cannot have any effect on the computed cross sections. This leads to the conclusion that one may not neglect the influence of logarithmic contributions to the exclusive 2-jet cross section when the cuts are not loose.

If the cut on the additional radiation is loose the migration uncertainty is small. In that case, a fixed-order calculation can be applied without having to worry about the impact of the logarithms on the perturbative uncertainty. If the cut values are very tight, i.e. small, then a resummation to all orders in α_s would be necessary [16][17]. In an experiment, one would choose the cut value at intermediate values, so that the migration uncertainty entailed by the logarithms cannot be considered small in general but resummation to all orders is not necessary. If one attempts to estimate the uncertainty on the exclusive cross section σ_2 by simply varying the scales like in the inclusive case, one might underestimate the uncertainty due to coincidental cancellations between the logarithms and other terms as explained above. A way to estimate the influence of the applied cut on the additional radiation is the *Steward-Tackmann* (ST) method [15]. Using this method, one can avoid the influence of accidental cancellations on the computation of theoretical uncertainties.

Still, one has to know what to plug in for the uncertainties Δ_2^y, Δ^{cut} and $\Delta_{\geq 3}^y$ in equation (32). As described above, perturbative uncertainties are commonly estimated via scale variations of the factorization scale μ_F and the renormalization scale μ_R. The uncertainties from these variations will be denoted in the following with a superscript μ. These are the only values for uncertainties available, so the final expression for the exclusive 2-jet cross section has to be given in terms of these.

The first assumption at this point is that these scale variation uncertainties are trustworthy for inclusive cross sections, i.e. $\Delta_{\geq 2} = \Delta_{\geq 2}^\mu$ and $\Delta_{\geq 3} = \Delta_{\geq 3}^\mu$. After plugging this into the equations (31) and (32), one obtains

$$(\Delta_{\geq 3}^\mu)^2 = (\Delta_{\geq 3}^y)^2 + (\Delta^{\text{cut}})^2$$
$$\Delta_{\geq 2}^\mu = \Delta_2^y + \Delta_{\geq 3}^y.$$

Assuming that the cuts are not very loose, one may not use just simple scale variations for all the terms involved and may not just set Δ^{cut} zero. Instead, one can argue that in a intermediate region of cutting the logarithmic contribution to $\sigma_{\geq 3}$, see equation (28), is dominating the series because the logarithms are in that case of order $\mathcal{O}(1)$. Thus, the variation of the scales in $\sigma_{\geq 3}$ mainly gives information about the magnitude of the logarithms, which are directly connected to

the migration uncertainty. The result of this reasoning is that one can take

$$\Delta^{\text{cut}} = \Delta^{\mu}_{\geq 3}.$$ (33)

Finally one obtains the following covariance matrix:

$$C_{ST} = \begin{pmatrix} (\Delta^{\mu}_{\geq 2})^2 + (\Delta^{\mu}_{\geq 3})^2 & -(\Delta^{\mu}_{\geq 3})^2 \\ -(\Delta^{\mu}_{\geq 3})^2 & (\Delta^{\mu}_{\geq 3})^2 \end{pmatrix}.$$ (34)

Thus, the exclusive 2-jet cross section is given by

$$\sigma_2^2 = (\Delta^{\mu}_{\geq 2})^2 + (\Delta^{\mu}_{\geq 3})^2.$$ (35)

This method of evaluating cross section uncertainties for selections with non-negligible migration uncertainties will be hereafter referred to as the *ST method*.
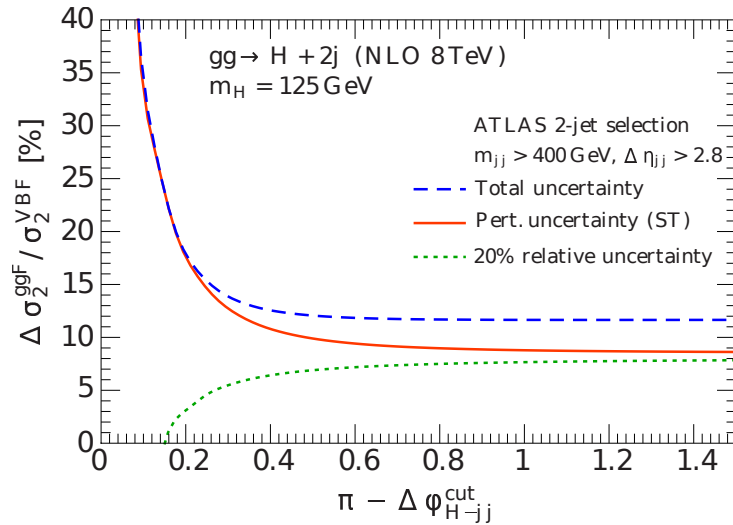

FIG. 6: Theoretical uncertainty on the ggF contamination in a VBF-enriched selection divided by the expected vector boson fusion cross section in selection [14].

In figure 6, the ST-uncertainty on the gluon fusion contribution in a loose VBF selection, divided by the expected selected VBF contribution, is shown. This is a interesting quantity, since it is a part of the relative uncertainty on the VBF cross section. The relative parametric uncertainty of 20 % on the ggF contribution quickly loses its impact on the total relative uncertainty because of the decrease of the selected number of ggF events. However, the perturbative uncertainty

overpowers the decrease in the number of selected ggF events, leading to a strong increase in $\Delta\sigma_2^{\text{ggF}}/\sigma_2^{\text{VBF}}$

The ST method can be propagated into a technique to compute uncertainties for more than two bins; this is necessary when the phase space restrictions are not as simple as a single cut on k. As will be described in section 3.5.2, the VBF selection which is used in the official analysis of the Higgs couplings [2] is using rather complicated phase space restrictions, for which such an extension of the ST method is necessary in order to compute the perturbative uncertainty on the number of selected ggF events. The inclusive 2-jet cross section can then be defined in a similar way as in (26) [4]:

$$\sigma_{\geq 2} = \int_0^{k_{\text{cut},1}} \mathrm{d}k \, \frac{\mathrm{d}\sigma_{\geq 2}}{\mathrm{d}k} + \int_{k_{\text{cut},1}}^{k_{\text{cut},2}} \mathrm{d}k \, \frac{\mathrm{d}\sigma_{\geq 2}}{\mathrm{d}k} + \cdots + \int_{k_{\text{cut},n-1}}^{k_{\text{cut},n}} \mathrm{d}k \, \frac{\mathrm{d}\sigma_{\geq 2}}{\mathrm{d}k} \,. \tag{36}$$

The creation of n bins in the variable k which is used as measure for the additional radiation requires the creation of a $n \times n$ covariance matrix. In order to construct this matrix, one can take advantage of the fact that uncertainties of two narrow bins which are next to each other are more correlated than those of bins which are much separated from each other. A simple linear correlation model has been used to arrive at a correlation matrix:

$$\kappa_{ij} = 1 - (1 - \kappa) \frac{|k_{\text{cut},i} - k_{\text{cut},j}|}{k_{\text{cut},n} - k_{\text{cut},1}} \,. \tag{37}$$

Since the exact value of κ is not known, several values have been tested. Fortunately, the outcome for the theoretical uncertainty resulting from the correlation matrix depends very little on κ [4].

In addition to perturbative uncertainties on the gluon fusion cross section, one may also be interested in the corresponding uncertainties for vector boson fusion. The VBF process is controlled by electroweak physics, and therefore the calculations are much more precise, leading to comparatively small uncertainties [13].

2 The ATLAS Experiment

2.1 The Large Hadron Collider

The ATLAS experiment is based at the *Large Hadron Collider* (LHC), which is the world's largest proton-proton collider, located in Geneva (Switzerland), and is part of CERN. The LHC has a circumference of 26.7 km [18]. Around the ring, four interaction points are installed. In these interaction points, two counter-rotating proton beams with each half of the center-of-mass energy $\sqrt{s}$ are brought to collision. A proton *bunch* is a set of protons captured within one bucket of the high-frequency electromagnetic field which accelerates the protons in radio-frequency cavities. A proton bunch contains about $10 \cdot 10^{11}$ protons. Since there are many protons in one bunch and the beams are very focused at the interaction points, there are typically many proton-proton interactions happening in the ATLAS detector during one bunch crossing, see table 2. In this table, the LHC design parameters as well as the corresponding parameters which describe the LHC operation in 2011 and 2012 are listed.

	Nominal design	2011	2012
$\sqrt{s}$	14 TeV	7 TeV	8 TeV
μ	19	9	21
Δt	25 ns	50 ns	50 ns
N_b	2808	1380	1374

TABLE 2: Performance parameters of the LHC runs in 2011 and 2012 as well as the design parameters. The center-of-mass energy is denoted by $\sqrt{s}$, the average number of proton-proton interactions per bunch crossing by μ, the time interval between two bunch crossings by Δt, and the number of bunches lined up along the total LHC circumference is denoted by N_b [2][18][19][20].

2.2 The ATLAS Detector: Introduction

The ATLAS detector is a multi-purpose detector at one of the four interaction regions of the LHC. An overview of it is shown in figure 7. As a multi-purpose detector, the ATLAS detector is designed to detect a wide range of different event topologies, among those the decays of Higgs bosons, as well as processes of physics beyond the Standard Model. This demands

greatest possible *coverage* of the detector. Ideally, no particle should leave the detector without being detected. But the detector cannot cover all directions since one can not place detectors arbitrarily close to the beamline. Moreover, neutrinos are very unlikely to leave a signal in the detector. Nevertheless, they can be detected indirectly by means of the conservation of transverse momentum.

The ATLAS detector consists of three subdetectors with different purposes:

- The **Inner Detector** detects charged particles and measures their momentum by measuring the particles' track curvature in a magnetic field.

- The **calorimeter** surrounds the Inner Detector and measures the energy of charged and uncharged particles.

- The **muon detector** surrounds the calorimeter system and measures the momentum of muons[23].
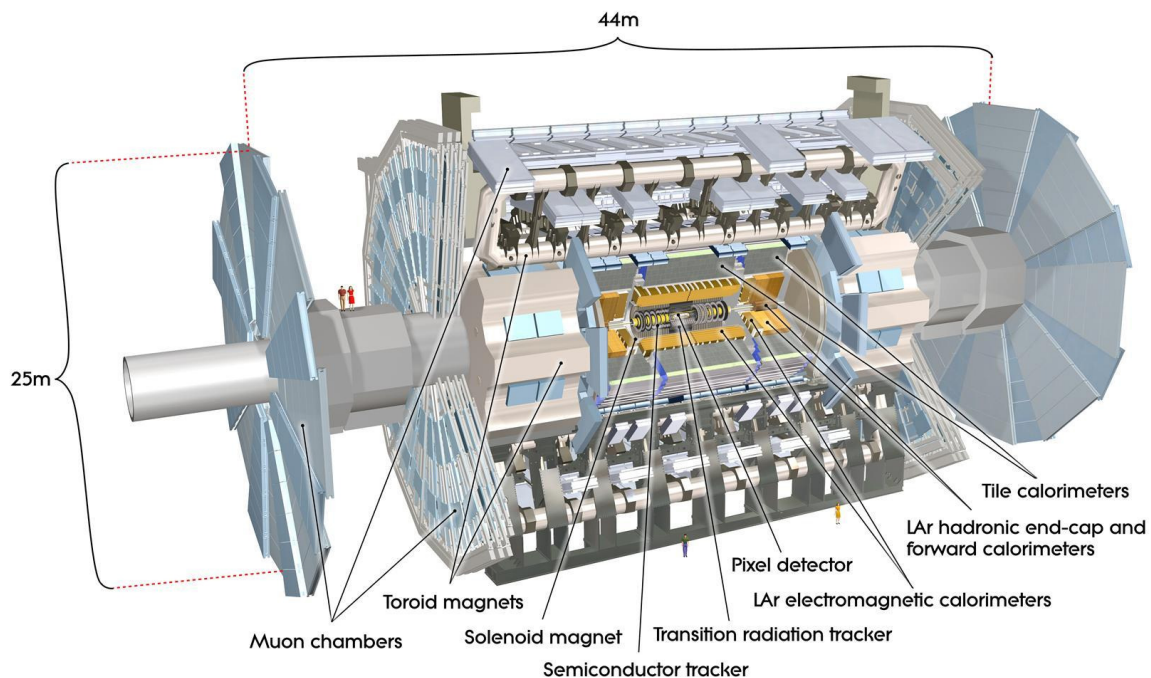

FIG. 7: An overview over the ATLAS detector [21].

---

[23]To be more precise: It measures the momentum of charged particles which have such large penetration power to traverse the calorimeters without being stopped. The majority of charged particles reaching the muon spectrometer are muons.

In order to minimize the number of undetected particles, *end-cap* detectors have been installed in addition to *barrel* detectors, which are placed in the central region of the detector. The subdetectors of ATLAS which are relevant for this thesis are described in more detail in sections 2.5 and 2.6.

2.3 Pile-Up

As mentioned in section 2.1, a bunch crossing typically leads to many *pp*-collisions, in which many particles are produced. The term *pile-up* refers to the presence and influence of additional, low-energetic proton-proton collisions in the measurement of properties of a given event. Those additional collisions result in additional particles with mostly low transverse momenta. Two categories of pile-up can be defined:

- *In-time* pile-up

- *Out-of-time* pile-up

Given that one has identified a proton-proton collision of interest, i.e. the hard interaction, the term *in-time pile-up* refers to the presence of additional proton-proton interactions in the *same* bunch crossing. This should not be confused with the term *underlying event*, which describes additional interactions between partons belonging to the same proton-proton pair as the hard-interacting pair of partons does. The term *out-of-time pile-up* denotes the influence of preceding bunch crossings on the present bunch crossing.

In general, it is important to reduce the impact of pile-up on experimental results and thus on the reconstructed events. Since proton-proton collisions predominantly produce hadrons, which are detected in form of tracks and jets, see sections 2.7.1 and 2.7.3, tracks and jets are objects of interest when one would like to reduce the influence of pile-up. Pile-up also gives a contribution to the noise level of the detectors, and, connected with these statistical fluctuation of the activity in the detector, has influence on e.g. shower shapes of signals in the calorimeters. Hence, one has to carefully study the effect of pile-up and techniques to mitigate its effects.

2.4 Geometry and Coordinate System

The ATLAS detector has a cylindrical shape and is forward-backward symmetrical. A three-dimensional coordinate system is spanned as follows [22]: The x-direction is pointing towards the center of the collider ring, the y-axis is pointing upwards, and the z-axis is parallel to the beam line. Often it is useful to use cylindrical coordinates R, ϕ and z to describe the detector geometry.

The azimuthal angle is defined by $\tan(\phi) = \Delta y / \Delta x$. In addition to the azimuthal angle, a polar angle needs to be defined: $\tan(\theta) = \sqrt{(\Delta x)^2 + (\Delta y)^2}/\Delta z$. From the detector response one can reconstruct the trajectory of particles. In the actual analysis, it is common to speak of particle momenta. Especially the transverse momentum, defined by

$$p_\mathrm{T} = \sqrt{p_x^2 + p_y^2}\,,\tag{38}$$

is of importance. Large transverse momenta indicate interactions in which a hard scattering has taken place, i.e. an interaction with large momentum transfer. These interactions are most interesting when physics processes at high energy scales, e.g. Higgs physics, are analyzed.

Closely connected to the polar angle is the *rapidity y*, which is given by $y = \frac{1}{2}\ln(\frac{E+p_\mathrm{L}}{E-p_\mathrm{L}})$, where p_L denotes the longitudinal momentum component of a particle. The rapidity is especially well suited for the description of event properties since differences in this variable are invariant under Lorentz boosts along the z-axis[24]. In the high-energy approximation, i.e. $m \ll E$, the rapidity y is equal to the *pseudorapidity η*, which is defined as

$$\eta = -\ln\left[\tan\left(\frac{\theta}{2}\right)\right].\tag{39}$$

In contrast to y, one only needs the polar angle for the computation of η, while for y the particle's energy and momentum must be measured. The pseudorapidity as a function of the polar angle is shown in figure 8.

It is useful to define a angular distance measure based on the pseudorapidity and the azimuthal

---

[24]The proton is not an elementary particle but consists of gluons and quarks. Because the fraction of the proton momentum those particles carry is not known for a given interaction, the center-of-mass reference frame is generally not known. Therefore it is a very useful that differences in the rapidity do not depend on the actual longitudinal velocity component of the rest frame of the colliding particles.

angle:

$$\Delta R = \sqrt{(\Delta\eta)^2 + (\Delta\phi)^2}. \tag{40}$$

This quantity must be distinguished from the radius R which is commonly used to quantify radial positions of detector elements.
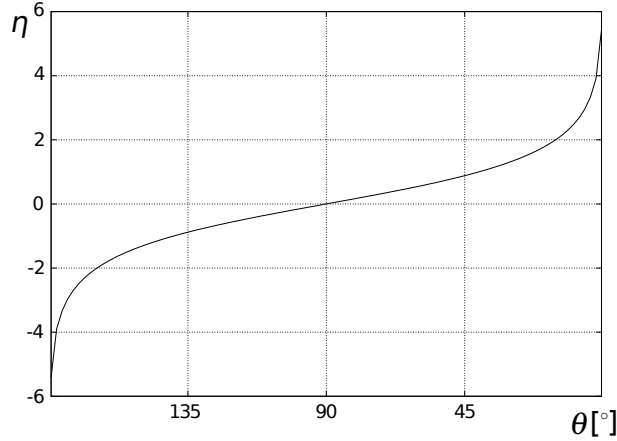

FIG. 8: Pseudorapidity η as function of the polar angle θ

2.5 The Inner Detector

The main purpose of the Inner Detector is to determine the momentum of charged particles and the position at which these particles emerge. For this, the trajectory of particles needs to be reconstructed. During the measurement of the corresponding particle hit positions, the trajectory of the particles should be changed as little as possible. Therefore one uses thin low-density materials. Silicon semiconductor detectors and gas detectors meet these conditions. In general, the detector components of the Inner Detector must be very radiation-hard.

Charged particles coming directly from proton-proton collisions as well as charged particles created in secondary interactions can be reconstructed. The latter also means that photons which are converted into an electron-positron pair inside the Inner Detector can be reconstructed as converted photons with high efficiency up to a radius of about 80 cm [23]. A superconducting solenoid magnet surrounds the Inner Detector. Because charged particles are deflected by a magnetic field, their momentum can be obtained by measuring the curvature of their trajectory:

$$R_{\text{curv}} = \frac{p_{\text{T}}}{qB}. \tag{41}$$

32

The sign of a particle's charge is obtained by the measurement of the curvature as well.

The magnetic field strength B is 2 T [22]. The solenoid magnetic field points to a good approximation in the z-direction. This holds quite exactly in the central region of the barrel, but at the ends of the solenoid, the radial component of the magnetic field strength reaches a value which is about one order of magnitude lower than the z-component, depending on the radial position. Only the z-component of the magnetic field should enter equation (41), since it is the transverse momentum which is to be measured.

The Inner Detector has a cylindrical shape with a radius of 1.08 m and a length of 7 m. It covers the range of $|\eta| < 2.5$. The momentum resolution which is achieved by the Inner Detector for high-p_T particles is about $\sigma_p/p = 5 \cdot 10^{-4}\,\text{GeV}^{-1} \times p_T$ [24]. Illustrations of the Inner Detector can be found in figures 9 and 10.

The Inner Detector consists of three subsystems:

- Pixel detector

- **S**emi**C**onductor **T**racker (SCT)

- **T**ransition **R**adiation **T**racker (TRT)

The pixel detector and the SCT are using doped silicon sensors connected to high voltage. If an energetic charged particle traverses such semiconductor detectors, electron-hole[25] pairs are created. Thus, a traversing charged particle can be detected by measuring the current which is powered by the high voltage and enabled by the particle-induced free charge carriers.

The TRT is the outermost part of the Inner Detector and employs a gas mixture whose molecules and atoms are ionized by energetic charged particles travelling through it; an applied voltage then leads to a detectable electrical current.

2.5.1 The Pixel Detector

The pixel detector is the innermost layer of the tracking system of ATLAS and therefore closest to the interaction point. The radial position of the pixel barrel layers ranges from 50.5 mm to 150 mm. As the name implies, pixels are used as detectors; thus, and a very good spatial

---

[25]A hole is an electron state which is not occupied. Such a hole can be described effectively as positively charged particle with an effective mass; a hole is capable of moving and can therefore be part of an electric current.
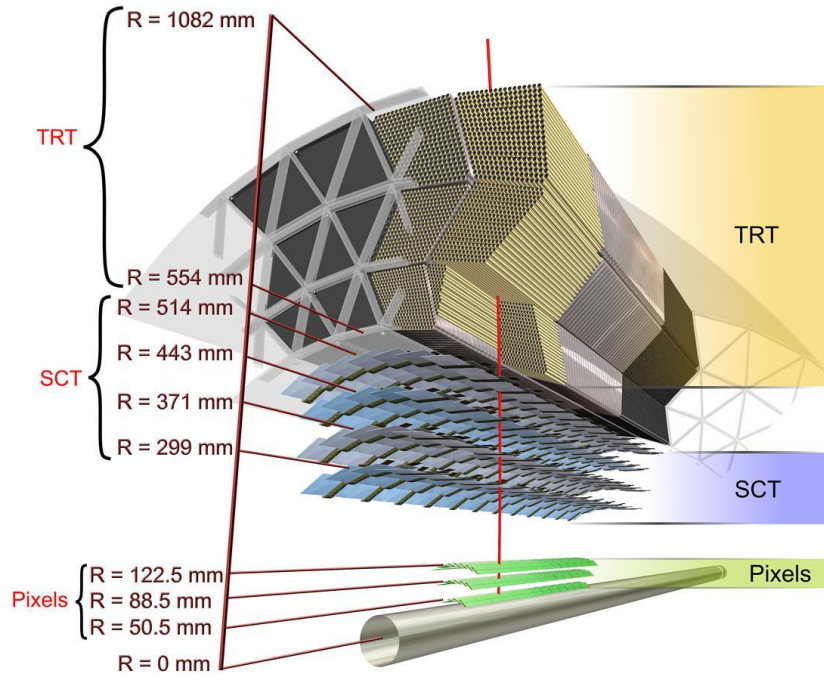
FIG. 9: Representative segment of the Inner Detector barrel with a particle leaving the interaction point at $R = 0\,\text{mm}$ and traversing the Inner Detector [25].

resolution of particle hits can be obtained in this subdetector. The pixel detector consists of three concentric cylinders around the beam axis in the barrel part[26] and of three discs on each side in the end-caps. In total there are $80 \cdot 10^6$ readout channels. The size in $R\phi \times z$ (for the barrel region) of most pixels (90 %) is $50\,\mu\text{m} \times 400\,\mu\text{m}$, the rest of them has the size $50\,\mu\text{m} \times 600\,\mu\text{m}$. Due to the small pixel size and the short distance between pixel layers and the interaction region, the pixel layer gives an important contribution to the accuracy of the position measurement of primary vertices, see section2.7.1. For the barrel part, the intrinsic spatial resolution is $10\,\mu\text{m}$ in $R\phi$-direction and the intrinsic resolution in z-direction is $115\,\mu\text{m}$. In the end-caps, the same resolution in $R\phi$ is provided as in the barrel part. Because the end-cap discs are placed perpendicular to the beamline, the z-position is fixed and instead the radial position is measured with an intrinsic accuracy of $115\,\mu\text{m}$.

---

[26]The number of pixel layers in the barrel has been recently incremented to four layers. For the analysis which is performed in this thesis, the data being used in this thesis was taken with the 3-layer pixel barrel.
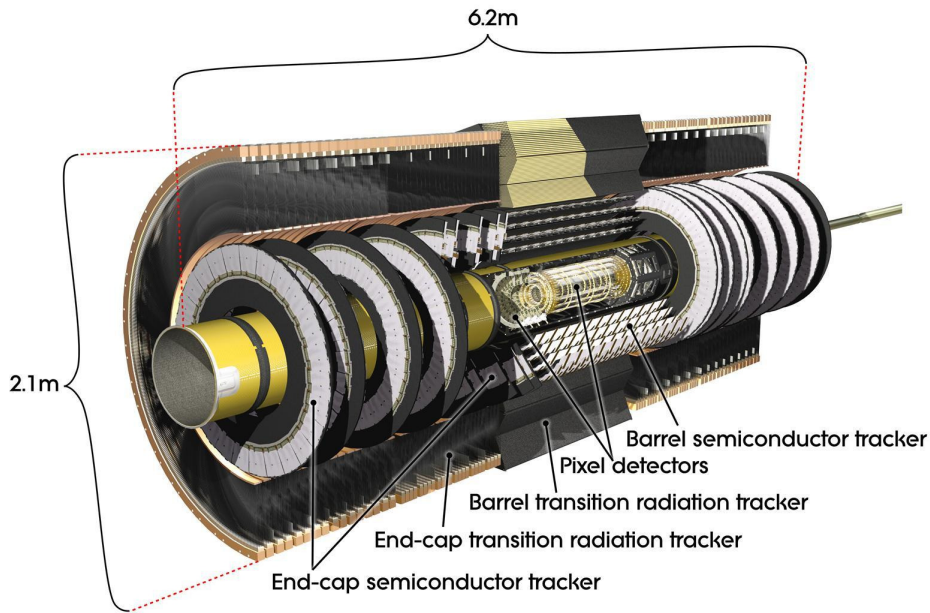
FIG. 10: A more complete view of the Inner Detector [25].

2.5.2 The Semiconductor Tracker

The SCT surrounds the pixel detector; it consists of $16 \cdot 10^3$ silicon microstrip detector sensors with each 768 active silicon strip sensors with a pitch of 80 μm [22]. These sensors are distributed over four radial layers in the barrel and over nine discs in each of the end-caps, containing each two microstrip sublayers, see figure 10. Because the silicon strips alone only allow for a one-dimensional measurement of a particle hit position, the microstrip sensors in the sublayers are placed on top of each other with a small stereo angle of 40 mrad, see figure 11. This angle allows to measure a second particle hit coordinate, i.e. the z-component in the barrel part and the radial component in the end-caps. A charged particle ideally leaves 8 hits on its way through the barrel SCT. In each end-cap, 9 double-layer discs employing the same stereo-angle technique are installed.

The SCT system provides an intrinsic spatial resolution in $R\phi$-direction of 17 μm. In the barrel, the z-position can be measured with an intrinsic resolution of 580 μm, and the same holds for the radial position in the end-caps.
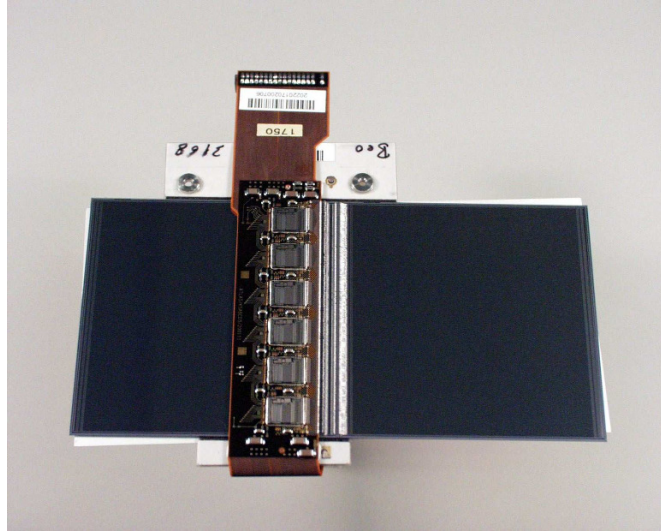
FIG. 11: Photograph of a barrel SCT module. Note the stereo angle between the two layers [22].

2.5.3 The Transition Radiation Tracker

The TRT is the outermost part of the Inner Detector and covers an η range of $|\eta| < 2.0$. It does not only give another contribution to the measurement of particle trajectories, but also induces and detects *transition radiation*, i.e. radiation produced by relativistic charged particles when they enter a medium with a different dielectric constant. The more relativistic a particle is, i.e. the higher its Lorentz factor γ, the higher is the intensity of transition radiation. Thus, the measurement of the transition radiation intensity gives information about the Lorentz factor. If, in addition, the particle's momentum is known, one can to some degree distinguish between light charged particles (i.e. electrons) and heavier charged particles like hadrons. The TRT consists of *straw-tubes*. These straw-tubes have a a diameter of 4 mm. The inner surface of these tubes is coated with aluminium, connected to high voltage. In each straw-tube is a 30 μm thick wire. The tubes are filled with a gas mixture which consists of 70 % Xe, 27 % CO_2 and 3 % O_2 [22]. When energetic charged particles traverse a tube, they ionize the gas, creating free charge carriers, which in turn lead to an electrical signal due to the applied voltage between the aluminium-coated inner surface and the wire in the tubes. The straw-tubes are interleaved with polypropylene-polyethylene. The straw tubes themselves can measure the particles position. The use of interleaving layers and fibres of polypropylene-polyethylene on the other hand leads to enhanced emission of transition radiation. In the barrel region, 73 layers of straw tubes are installed, in the end-caps this number amounts to 160. A charged particle produces on average

36 TRT hits [22]. Due to the arrangement of the straw tubes, the TRT provides only information about the $(R\phi)$ coordinate in the barrel region.

2.6 The Calorimeter

A calorimeter is a device to measure the energy. In order to do so, the energy of a particle has to be transformed into measurable signals in the calorimeter. To measure the whole energy of a particle, the calorimeter must be designed thick enough in order to stop and absorb incident particles completely. This closure is advantageous in three aspects:

- It is unlikely to miss a significant part of the particles energy in the energy measurement.

- Given this first advantage, the missing transverse momentum per event can be computed with good reliability.

- The operation of the calorimeter-surrounding Muon System is based on the assumption that only muons can reach it. This entails that all other particles which could be measured in the Muon System should be stopped beforehand, i.e. inside the calorimeter.

The measurement of the particle or jet energies cannot be done by simply stopping them in dense absorbers, called *passive* material. For the task of measuring the energy of a particle, *active* material is needed. Like passive material, whose purpose is to most effectively absorb and distribute particle energy by creating a shower, active material must absorb energy in order to serve its purpose, i.e. the measurement of particle energy. But unlike in passive material, the absorbed energy is not transformed only into heat and secondary particles but also into an electrical or optical signal, which can be read out and interpreted as a measure of the deposited energy.

One distinguishes between homogeneous and sampling calorimeters [6]. In the former calorimeter type, active and passive material is identical. The latter is made of layers of alternately passive and active material. In figure 12, an electromagnetic shower, see section 2.6.1 for further explanations, in such a calorimeter is depicted. Both have advantages and disadvantages: A particle which creates a shower in a sampling calorimeter deposits energy also in passive parts of the detector; therefore one has to extrapolate from the energy measured in the active material up to the energy which is expected to be deposited in the active *and* the passive material. This

37

results in a limit on the energy resolution. An advantage is the longitudinal segmentation, which allows for more detailed information about the longitudinal shape of showers in the calorimeter.

2.6.1 Electromagnetic Showers

The calorimeter stops incoming particles by enforcing the production of a *particle shower*, which is driven by the energy of the original particle. Such a shower develops from the successive production of secondary particles, which in turn produce secondary particles themselves. In purely electromagnetic showers, the production of secondary particles can occur via electron-positron pair production in case of incoming photons ($\gamma \rightarrow e^+ e^-$), and via bremsstrahlung in case of incoming charged particles like electrons ($e^\pm \rightarrow e^\pm + \gamma$). By a multitude of these two processes, the energy of the original particle is distributed to many secondary particles. When the energy of the incoming particle has been distributed to so many secondary particles such that those secondaries' energies do not allow for the production of further secondary particles, the shower stops to grow and the remaining kinetic energy gets absorbed in processes such as Compton scattering or ionization.

A way to define and measure the absorption power of a given material for charged particles is the radiation length X_0. It denotes the thickness of the material that decreases the mean energy of a charged particle by a factor of $1/e$ when that particle travels through the given material. The radiation length for lead is $X_0 = 5.6\,\text{mm}$ [6]. This is a relatively small value, which corresponds to a relatively large stopping power. In general, the radiation length is smaller the larger the charge of the material's nuclei is. A quantity which is closely related to X_0 is the mean free path λ of an energetic photon before undergoing a pair production process; this length is connected to the radiation length X_0 introduced above via $\lambda = 9X_0/7$.
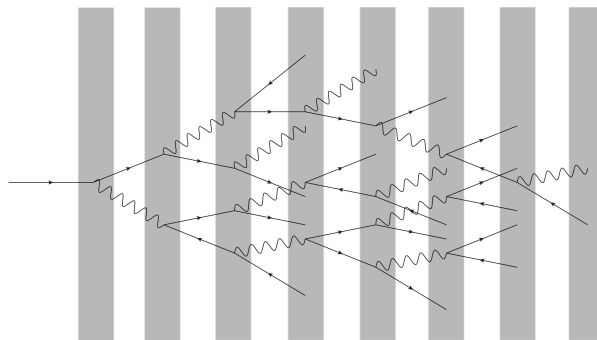

FIG. 12: Schematic sketch of an electromagnetic shower traversing a sampling calorimeter.

2.6.2 Hadronic Showers

For hadronic incident particles, the shower development is more complicated than for electromagnetic showers. Compared to electrons, even the lightest hadrons are very heavy and emit therefore much less electromagnetic bremsstrahlung. Beside that, not all hadrons are electrically charged. Hadrons interact via the strong force with the nuclei in the detector material. Through the interaction of hadrons with the atomic nuclei, the nuclei can be excited, with the result that a part of the shower energy is stored in a way that can not be detected. Because pions are the lightest hadrons, many of them are produced in the development of a hadronic shower. On average, one third of pions are neutral pions, which decay very quickly into two photons and result in an electromagnetic shower. The individual electromagnetic fraction of the deposited energy varies from shower to shower. To summarize, the energy which is deposited in the calorimeter by a generic jet with an energy of $100\,\mathrm{GeV}$ consists on average of roughly [26]

- $50\,\%$ electromagnetic components (neutral pions decaying into a pair of photons, electrons, photons),

- $25\,\%$ visible strongly interacting components (protons, neutrons, charged pions, etc.) and

- $25\,\%$ invisible energy of nuclear excitations or spallation, muons or neutrinos.

These fractions depend on the type and energy of the incident particle. As a result, it is comparatively difficult to reconstruct the energy of the actual incident hadron, which entails that the resolution of hadron energy measurements is worse than the energy resolution of electrons or photons. Hadronic showers tend to be larger than electromagnetic showers, which is a fact that is also used to distinguish them from electromagnetic showers.

2.6.3 The Electromagnetic Calorimeter

The ATLAS calorimeter consists of two subdetectors: An electromagnetic calorimeter and a hadronic calorimeter. The former surrounds the solenoid system and is enclosed by the hadronic calorimeter, which will be described in section 2.6.4. Both calorimeters are sampling calorimeters. An overview of the calorimetric system is shown in figure 13.

The ATLAS electromagnetic calorimeter is a sampling calorimeter with an *accordion* geometry, to be seen in figure 14. This geometry has the advantage of a good homogeneous response in the
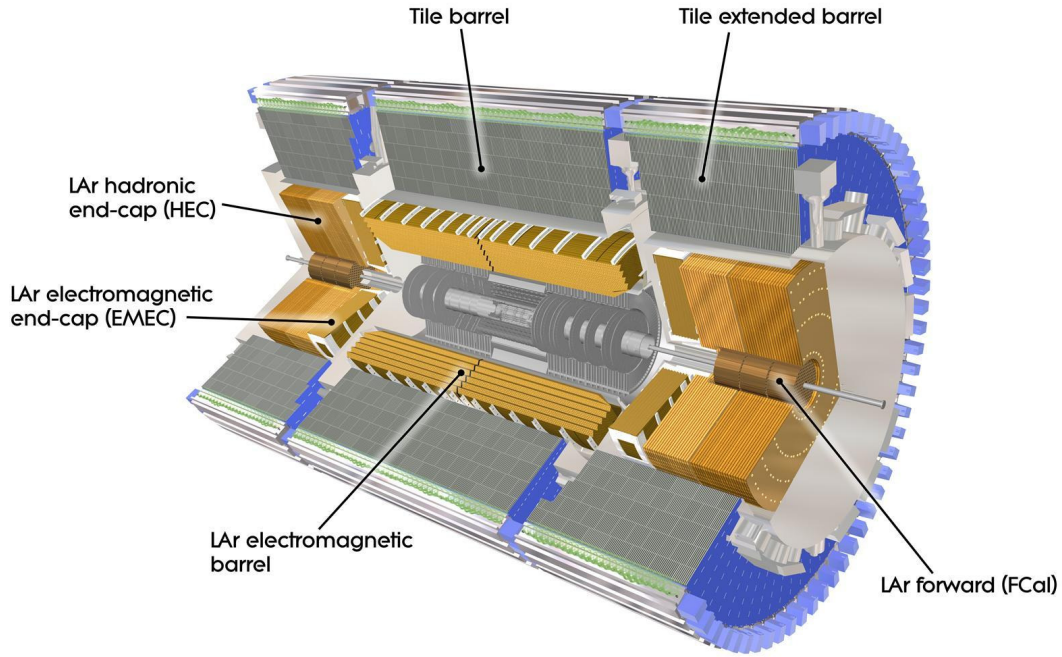
FIG. 13: Overview over the ATLAS calorimetric systems [22].

whole azimuthal range and avoids azimuthal cracks. The electromagnetic calorimeter is divided into a barrel part two end-caps.

In the barrel part, lead plates are used a passive material. Between those plates is liquid argon, in which copper anodes are submerged. This is used as active element of the electromagnetic calorimeter. By the interaction with traversing high-energetic particles, argon atoms are ionized, i.e. free charge carriers are created. By a strong electric field, a measurable current pulse is generated in the event of energy depositions of energetic particles. The electromagnetic
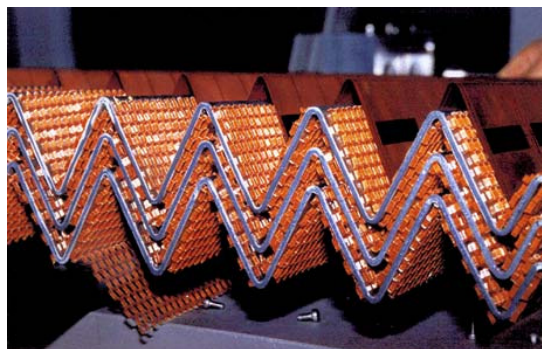

FIG. 14: Schematic detail of the sampling structure of the electromagnetic calorimeter [27].

calorimeter has a lateral and longitudinal substructure; for a schematic illustration and details on

the cell sizes see figure 15. In the η region of $|\eta| < 2.5$ there are three longitudinal segments, whereas in the region of $2.5 < |\eta| < 3.2$, only two longitudinal segments exist. Each of the longitudinal segments has a different granularity in η and ϕ.

- The first longitudinal segment, closest to the beam pipe, is also called *strip layer*, due to its fine segmentation in the η direction. Thanks to its fine granularity, single photons or electrons can be effectively distinguished from neutral hadrons like neutral pions, which decay very quickly into a collimated[27] pair of photons, such that it is reconstructed as a single calorimeter cluster. The fine segmentation of the strip layer can resolve a substructure in the shower shape, which is very helpful to veto such *fake photons*. However, this fine segmentation exists only in the pseudorapidity range of $|\eta| < 2.5$.

- The second layer has a coarser structure than the first layer, as can be seen in figure 15. It is the thickest segment and absorbs most of the energy of electromagnetic showers.

- A third longitudinal layer is installed in the η region of $|\eta| < 2.5$ to measure the longitudinal tail of high-energy showers.

In order to correct for energy losses in the upstream material, i.e. material from cryogenic systems and supporting structures, in the range of $|\eta| < 1.8$ a presampler is installed between the electromagnetic calorimeter and the tracker. The overall thickness of the electromagnetic calorimeter in terms of radiation lengths is always larger than 22 X_0 in the barrel part and is always larger than 24 X_0 in the end-caps [22].

---

[27]At least at photon candidate energies which are interesting in the present analysis.
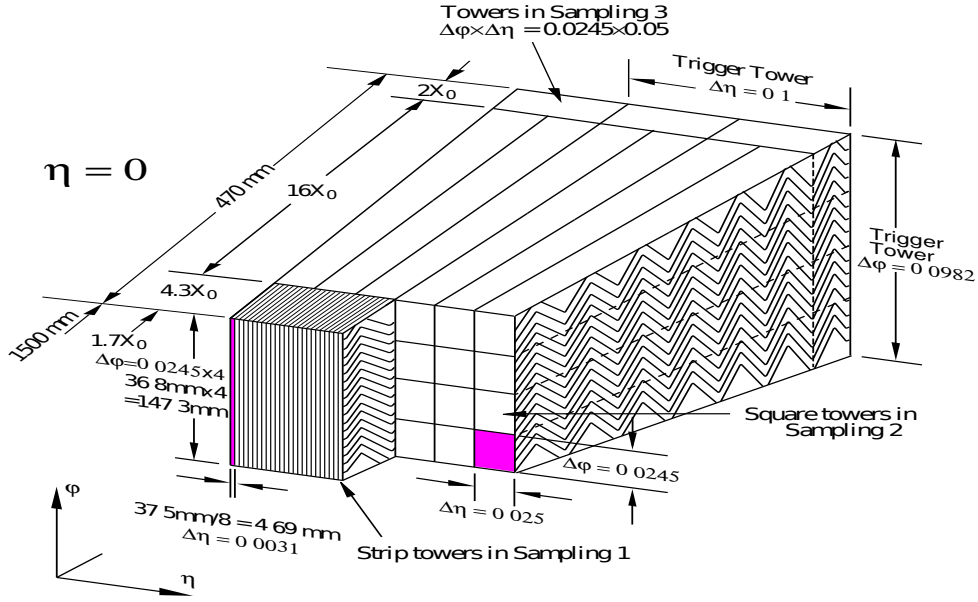
FIG. 15: Segmentation of the individual layers of the electromagnetic calorimeter [22].

2.6.4 The Hadronic Calorimeter

The hadronic calorimeter is of importance when one wants to measure the energy of jets. It uses three different combinations of active and passive material [22]:

- In the range of $|\eta| < 1.7$ a tile calorimeter with steel tiles as passive material and plastic scintillators as active material is used. The tile calorimeter consists of a barrel part and two extended-barrel parts. It ranges from a radius of 2.28 m to 4.25 m. This means that it is much thicker than the electromagnetic calorimeter, a fact that is necessitated by the larger size of hadronic showers. The light produced by particles interacting with the the scintillators is read out[28] by photomultipliers, which generate an electrical signal. The tile calorimeter is longitudinally segmented into three parts, of which the first two have a granularity of $\Delta\eta \times \Delta\phi = 0.1 \times 0.1$, while the outermost layer is segmented into $\Delta\eta \times \Delta\phi = 0.2 \times 0.1$.

- In the end-cap region of $1.5 < |\eta| < 3.2$ a liquid argon hadronic calorimeter is used for hadronic calorimetry. Liquid argon as active material is more radiation-hard than plastic scintillators. Because of this property, it is used in the end-cap region, which is subject to

---

[28]To be more precise, ultraviolet radiation is produced in the scintillators and is subsequently shifted in its wavelength in order to be detectable by the photomultipliers.

higher doses of radiation than the barrel region. Copper is used as passive material. The end-cap hadronic calorimeter is composed of two wheel-shaped subdetectors, which have a flat-plate sampling geometry.

- In the forward-region of $3.1 < |\eta| < 4.9$, the Forward Calorimeter is placed, which also uses the radiation-hard Liquid-Argon technology. The Forward Calorimeter consists of three 45 cm deep wheels. Although the first of the three is employed for electromagnetic calorimetry, all three of them will be described here for the sake of simplicity. Copper serves as passive material for the first wheel. The passive material of the outer two wheels is chosen to be tungsten because of its large stopping power. The forward calorimeter is essentially a block of metal, in which many thin tunnels are incorporated. These tunnels contain electrodes which are immersed in liquid argon [22].

2.7 Definition of Physical Objects

In the following, the basic analysis objects relevant for this thesis will be discussed, i.e. especially photons and hadronic particles which result in tracks and jets.

2.7.1 Tracks and Vertices

Tracks are signatures of charged particles travelling through the Inner Detector. Due to the limited range of the Inner Detector, charged particles can only be reconstructed as tracks if they have a pseudorapidity of $|\eta| < 2.5$. A typical track in the barrel region consists of 3 hits in the pixel system, 8 hits in the SCT and 36 hits in the TRT [28].

One distinguishes between the *back-tracking* method and the *inside-out* algorithm for track reconstruction [29]. The latter is seeded by hits in the silicon layers of the Inner Detector, the former by hits in the TRT. Using the spacepoints of a seed, one can determine a seed direction. In the next step, hits which are close to the extrapolated line, are associated with the seed. Based on these track candidates, further actions with aim to resolve ambiguities between the track candidates and to remove fake tracks are performed. While in the inside-out algorithm the seed is extrapolated to larger radii, the back-tracking algorithm extends the TRT-based seed in direction of the silicon detectors, i.e. to lower radii. In back-tracking, one distinguishes between tracks which only contain information from the TRT and tracks that also contain hits in

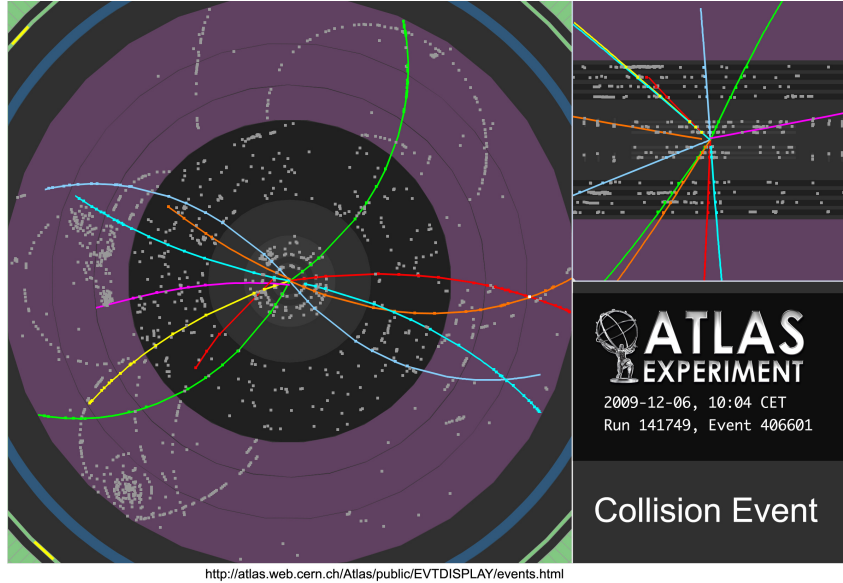http://atlas.web.cern.ch/Atlas/public/EVTDISPLAY/events.html

FIG. 16: Reconstructed tracks in the Inner Detector. The grey blobs represent energy deposits in the tracking devices [30].

the silicon detectors. Back-tracking is useful to reconstruct converted photons or tracks which have been shadowed by other track candidates in the inward-track-reconstruction. Tracks which are reconstructed by the inside-out algorithm must have a p_T larger than 0.4 GeV. Tracks are required to have 7 hits in the silicon detectors. The amount of pile-up has influence on the reconstruction of tracks in the Inner Detector. In general, the reconstruction becomes more and more complicated when pile-up increases. A result of increased pile-up is a degraded resolution of track parameters, a smaller fraction of reconstructed tracks and more fake tracks from random combination of hits in the Inner Detector. On basis of tracks, primary vertices are reconstructed. Primary vertices are points of interactions between two colliding protons. In the LHC environment, there are on average multiple primary vertices per bunch crossing, see table 2 on page 28. The first step in the vertex reconstruction is to create the distribution of the z-coordinate of reconstructed tracks at the point of closest approach to the center of the beamspot. The global maximum of this distribution is taken as seed for a primary vertex [31]. This seed and nearby tracks enter an iterative vertex finding algorithm [28]. In this algorithm, a χ^2 fit is performed. Based on the outcome of this fit, each track receives a weight which quantifies the track's compatibility with the vertex. If the distance between a track's position and the fitted vertex position is larger than approximately 7σ, where σ is the uncertainty on the z-position estimated in the fit, it is treated as seed for a new vertex. Again a fit will be

44

performed, using tracks in the vicinity, and so on, until no further vertex can be found. This vertex finding algorithm is an iterative process and it includes that a track is tried to fit in different vertices; in the end, however, a given track can only be influential on the position of one single vertex and can only be associated with at most one vertex. A vertex is required to have at least two tracks assigned to it. The reconstruction of vertices is necessary for the identification of particles coming from the hard interaction and also to measure the amount of pile-up on an event-by-event basis. The more proton-proton collisions occur during a bunch crossing, the smaller the fraction of reconstructed proton-proton interactions. This is due to *shadowing*, which denotes the hindrance of reconstruction of vertices caused by nearby proton-proton collisions. The mean number of tracks forming one vertex is about 20 tracks [28].

In a Higgs analysis, one of the possibly many reconstructed vertices will be identified as the *Higgs vertex* – the vertex which is taken to correspond to the interaction that includes the production of a Higgs boson. It is important to do so, since not only the decay products of the Higgs boson, e.g. two photons, are interesting, but also the additional emissions originating in the vertex in which the Higgs boson has been produced. These emissions, of which electrically charged ones can be reconstructed as tracks in the Inner Detector and assigned to vertices, constitute the basis for the computation of the event shape observable τ_2. Thus, it is important to correctly identify the Higgs production vertex among all reconstructed vertices. In most analyses, a vertex is selected as hard-interaction vertex when the summed squared transverse momentum of the tracks that are associated with it is maximal. In the $H \rightarrow \gamma\gamma$ analysis however, this method often does not identify the hard-interaction vertex since the photons will often carry away significant amounts of transverse momentum which is not considered in the computation of the summed squared transverse momentum. Tracks of converted photons are in most cases not used in this computation, due to their rather high impact parameter and subsequent inaccurate assignment to particular vertices. Instead, a *neural network*, which uses more information than the summed track transverse momentum [2], is utilized. The networks input variables are:

- A vertex position obtained by photon pointing. Enabled by the longitudinal calorimeter segmentation, the two photon signals in the calorimeter are used to extrapolate the photon signal in the calorimeter to the beamline. In case of converted photon, also the conversion

vertex is used in the extrapolation of the photon trajectory. The resulting common diphoton vertex position enters the neural network.

- The summed squared and scalar transverse momenta of tracks associated with the vertex, $\sum p_T^2$ and $\sum p_T$.

- The difference in azimuthal angle between the diphoton system and the vector sum of the momenta of tracks which are associated with the primary vertex. Due to conservation of momentum, this is observable is vanishing for the true $H \to \gamma\gamma$ vertex (in case of perfect particle reconstruction and measurement).

With reconstructed tracks and vertices at hand, one can impose further constraints on tracks associated with the hard-interaction vertex in order to remove tracks originating in pile-up vertices from the Higgs vertex. In this analysis only tracks which fulfill one of the two following conditions are considered:

- The track is used in the Higgs vertex fitting procedure for the identified Higgs vertex and its fitting weight, which is a measure of its compatibility with a given primary vertex, is larger than 0.1.

- The track is not part of *any* vertex fit but it is closer to the fitted Higgs vertex position than to any other vertex.

Only tracks above with a transverse momentum of 0.5 GeV will be considered in this thesis.

2.7.2 Photons

Photons are an important analysis object in Higgs physics. When a high-energetic photon is produced in a pp-collision and enters the calorimeter, it may have been undergone a pair-production process in the Inner-Detector material, resulting in an electron-positron pair. The probability for a photon to be converted in the Inner-Detector material is about 50 % if it is not emitted at very small rapidities; in that case, the probability for conversion is about 25 %. [29]. In the process of photon reconstruction, one distinguishes between converted photons and unconverted photons.

Photon candidates (as well as electron candidates) are seeded by energy deposits (*clusters*) in the electromagnetic calorimeter with a transverse energy larger than $2.5\,\text{GeV}$, using a *sliding-window* algorithm [32] with a window size of $\Delta\eta \times \Delta\phi = 0.075 \times 0.125$ for the finding of clusters. If a track is matched to the cluster found by the sliding-window algorithm and if a photon-conversion vertex for the matched track has been found, the cluster is considered a converted-photon candidate. A track is matched to an electromagnetic cluster if the extrapolated track position in the calorimeter is closer than 0.05 in η-direction and closer than 0.1 in ϕ-direction to the center of the cluster [33]. If a cluster is found to be unmatched by a track, it is a unconverted-photon candidate. After the categorization in converted and unconverted photons, the cluster is rebuilt with a customized[29] area in η- and ϕ-direction: In the barrel part of the calorimeter, an area of $\Delta\eta \times \Delta\phi = 0.075 \times 0.175$ and $\Delta\eta \times \Delta\phi = 0.075 \times 0.125$ is used for converted-photon and unconverted-photon candidates, respectively. In the end-caps, a cluster size of $\Delta\eta \times \Delta\phi = 0.0125 \times 0.125$ is used for both. The cluster energies are then corrected for losses due to upstream material and for lateral and longitudinal leakage losses.

After this cluster building and classification, a photon identification algorithm is used in order to reject *fake photons*. Fake photons are signals created by hadronic particles, especially neutral pions, which decay very quickly into a collimated pair of photons. Based on the shower shape in the calorimeter, many of these fake photons can be rejected, strongly based on the fine segmentation of the first longitudinal layer of the electromagnetic calorimeter. Only photon candidates that pass the *tight* photon identification criteria will be considered as identified photons; these enter the analysis. These tight criteria are different for converted and unconverted photon candidates [34].

In order to suppress the jet contamination of the photon sample as effective as possible, additionally two isolation observables are used:

- Calorimeter-based isolation: This quantity corresponds to the sum of transverse energy deposited within a radius $R = \sqrt{(\Delta\eta)^2 + (\Delta\phi)^2} < 0.4$, where the energy belonging to the reconstructed photon candidate is excluded. This excluded energy is the energy that is contained within an area of $\Delta\eta \times \Delta\phi = 0.125 \times 0.175$ centered around the cluster barycenter. Because there is some leakage of the photon energy outside this window of

---

[29]Converted photons tend to have larger cluster sizes in ϕ-direction, due to radiation processes which are induced by the deflection in the magnetic field.

$\Delta\eta \times \Delta\phi = 0.125 \times 0.175$, one applies a leakage correction which is determined by the cluster's transverse energy [35]. Moreover, a subtraction of the median energy density stemming from the underlying event is performed on an event-per-event basis.

- Track-based isolation: This is the scalar sum of track transverse momentum p_T within $\Delta R < 0.2$ around the photon, excluding conversion tracks as well as those tracks which are not produced in the hard-interaction vertex [23].

If a photon candidate has a calorimeter-based isolation smaller than $6\,\text{GeV}$ and a track-based isolation smaller than $2.6\,\text{GeV}$ [2], it is considered *isolated*.

An accurate measurement of the photon energy is important for many purposes, for example for the measurement of the Higgs-boson mass in the diphoton decay channel. The cluster energy is corrected for losses in the upstream material and for lateral and longitudinal leakage losses. Moreover, the cluster energy calibration is performed using simulations of the detector geometry. For the calibration of the electromagnetic energy scale, $Z \rightarrow ee$ events have been used [23]. The uncertainty on the energy measurement of converted and unconverted photons is about $0.2\,\%$ to $0.3\,\%$ in the barrel region of $|\eta| < 1.37$ and in the region $1.82 < |\eta|$. In the pseudorapidity region of $1.52 < |\eta| < 1.82$, this uncertainty is $0.9\,\%$ and $0.4\,\%$ for unconverted and converted photons, respectively. In the transverse energy range of $30\,\text{GeV} < E_T < 100\,\text{GeV}$, unconverted photons and converted photons are identified with an efficiency of about $83\,\%$ to $95\,\%$ and $87\,\%$ to $99\,\%$, respectively [2].

2.7.3 Jets

Jets originate from high-energetic quarks and gluons with relatively high p_T, which in the course of their showering and subsequent hadronization processes generate a evolve into spray of hadrons. In the ATLAS detector, they appear as a cluster of energy deposits in the calorimeter which can have corresponding tracks in the Inner Detector if the jet is in the acceptance of the Inner Detector. Several algorithms to build jets from detector signals are available; the most commonly used one is the anti-k_T algorithm [36], which is also in used in this thesis. The distance parameter, which controls the lateral size of reconstructed jets, is chosen to be $R = 0.4$. *Topological calorimeter clusters* are the seed for the jet-finding algorithm. These clusters in turn

are seeded from calorimeter cells with signal-to-noise[30] ratio $S/N > 4$. If a neighbor cell has a signal-to-noise ratio of larger than 2, it will be added to the cluster. If a neighbor cell has a signal-to-noise ratio of larger than 4, it will be made a seed cell itself. By repeating this procedure until no neighboring cells with $S/N > 2$ are found, the cluster grows. When the growth process has come to an end, all cells which are a neighbor of one of the outer cluster cells are added to the cluster. The result is a topological calorimeter cluster [37]. On the basis of these topological clusters, or, more specifically, their massless 4-momenta, jets are clustered using the anti-k_{T} algorithm.

Due to pile-up, there are in general more jets in the detector than belonging to the hard-interaction vertex. These pile-up can be falsely attributed to the hard-interaction. Also single tracks from pile-up interactions can be assigned with the hard-interaction vertex, which also should be avoided as well. Moreover, jets and diffuse radiation from pile-up give a contribution to the noise level in the calorimeters, which also enters the energy measurement of photons, other jets, etc. The latter effect of pile-up jets can be mitigated by a a subtraction of the median energy area-density of the total event scaled with the transverse area of the jet belonging to the hard-interaction [2]. The former, i.e. the incorrect assignment of pile-up jets with the hard-interaction can be attenuated by means of a track-based variable called *jet-vertex-fraction* (JVF) is introduced. Given that a vertex is chosen to be the hard-interaction vertex, denoted with PV_0, the jet-vertex-fraction is defined with respect to it and for each jet J_i as [38]

$$JVF(J_i) = \frac{\sum_{k \in J_i} p_{\mathrm{T}}^k(PV_0)}{\sum_{l \in J_i} p_{\mathrm{T}}^l(PV_0) + \sum_n \sum_{l \in J_i} p_{\mathrm{T}}^l(PV_n)} \,, \qquad (42)$$

where k and l refer to all tracks matched to jet J_i[31]. In the sum over n it is implied that all primary vertices which are not identical with the hard-interaction vertex PV_0 are taken into account. In general, the vertex identifier PV_a given in parenthesis denotes the vertex to which the track has been assigned by the vertex reconstruction algorithm. The jet-vertex-fraction is thus defined as the fraction of transverse momentum of a jet which is associated with the hard-interaction vertex. If this variable is of size unity, all tracks of the jet in question are reconstructed to originate in

---

[30]The noise consists of electronic noise as well of incident particles from other proton-proton interactions; see subsection 2.3.

[31]This matching is done by a method called *ghost association*: The transverse momentum of all tracks associated to a primary vertex is scaled down by a very small number. Then, these tracks are added to the jet reconstruction algorithm, which is then run again. If a *ghost* track is assigned to the jet, the track and the jet are matched.

the hard-interaction vertex. Such a jet is quite likely to have originated from the hard interaction. A jet whose jet-vertex-fraction is close to zero is a jet that mostly contains tracks produced in pile-up reactions and will be accordingly rejected. If no track is assigned to a given jet, the jet has per definition a jet-vertex-fraction of -1. Since this form of pile-up rejection is inherently relying on tracks and their attribution to primary vertices, this mapping has to be done with great care. Moreover it is to be noted that the jet-vertex-fraction itself is pile-up-dependent, as can be seen in equation (42). The more pile-up, the more vertices and contribution from these additional vertices to the assessed jet enter the calculation; therefore the jet-vertex-fraction of signal jets decreases with increasing pile-up. As a result, the signal jet efficiency is a function of the number of vertices. At 8 TeV and within the range $|\eta| < 2.4$ (compare with the Inner Detector range) only jets with a jet-vertex-fraction of above 0.25 are taken into further consideration [2]. Outside of the tracking region, no such constraint is imposed.

It is also useful to define at truth level, that is, directly using stable final-state particles from Monte-Carlo simulations (see section 3.2) as input for the jet building algorithm. A stable particle is defined as a particle with an expected lifetime such that $c\tau > 10$ mm. All charged and neutral particles excluding muons and neutrinos are taken into account.

The jets, both at reconstruction and at truth level, are required to be within an η range of $|\eta| < 4.4$ and to have a transverse momentum larger than 30 GeV. Because each photon is also reconstructed as a jet and should not be double-counted as jet, a jet will be rejected if the angular distance of a jet to an isolated photon is smaller than $\Delta R < 0.4$.

2.8 The Trigger

Most collisions in the ATLAS detector only involve low-energy QCD interactions, which are not of primary interest in the ATLAS physics program. Instead, one would rather focus on more rare processes. The *trigger* of the ATLAS experiment actuates the recording of an event if the event's features suggest that the event may be containing one of the rare processes one is looking for. Since the fraction of rare events among all available events is tiny, the criteria for an event to be stored have to be chosen with care. At design luminosity, bunch crossings occur at a rate of 40 MHz, while in run 1 the rate has been 20 MHz[32]. At the same time, the number of events

---

[32]But due to multiple proton-proton interactions during one bunch crossing, the total proton-proton interaction rate is about $1 \cdot 10^9$ per second.

which can be stored per second amounts only to approximately 200 [22]. The size of a stored event is of order 1 MB.

The ATLAS trigger is constructed as a three-level system: The first part of the trigger is called level 1 trigger (L1) and reduces the initial rate of 40 MHz (20 MHz) to 0.1 MHz. When this is done, the second trigger level L2 reduces the rate to about 1 kHz; the third step is done by the so-called *Event Filter* (EF), which filters the remaining 10^3 events per second such that about 200 events per second are selected for permanent storage [22].

The complexity of the respective filter algorithms must be relatively low in case of L1, while L2 and the EF can run more complex algorithms. The Event Filter has the most time to decide upon a given event, so that in the Event Filter algorithms can be similar to the offline filter-algorithms. In the following, the three trigger components will be briefly described.

- L1: The L1 trigger analyzes the transverse energy of electromagnetic clusters, muons and jets. Moreover, it is computing the missing E_T and the summed transverse energy $\sum E_T$. Only calorimeter and muon system information is used at this stage of event selection. Because of the complexity of the reconstruction of tracks, track information is not used at L1. The L1 trigger uses rather low detector granularity; see figure 15 on page 42 for an illustration of the size of the *trigger towers*, the basic units of granularity in L1. During the L1 decision time, all data coming from the detector must be kept in a pipeline-like memory. Among other things[33], the L1 trigger passes the coordinates of so called *Regions of Interest* (RoI) to the L2 and EF triggers.

- L2: The L2 trigger is seeded with the Regions of Interest defined in L1 and analyzes them with higher granularity and accuracy. Moreover, it uses information from the Inner Detector. If also L2 confirms that the event is looking interesting, the *event builder* is instructed to reconstruct the whole event. In the course of the reconstruction, all available detector information is collected and formatted. This built event is then passed on to the Event Filter.

- The Event Filter uses offline-like software to analyze the event. If an event also passes this filter, it is written to storage to be part of physics analyses.

---

[33]This includes the p_T threshold range, the missing-E_T vector, the total scalar sum of transverse energy as well as the criteria which has lead to the L1-triggering of the event.

3 Selection of Vector Boson Fusion Events Using an Inclusive Event Shape

3.1 Preface

In this chapter, the analysis and its results will be presented. The analysis goal is to examine the experimental properties of the event shape τ_2 as well as to propose a VBF-enriched selection based on this observable, especially in order to estimate the contribution of the perturbative uncertainty on the ggF contamination in a τ_2-based VBF selection to the total uncertainty on the VBF signal strength. The VBF signal strength is defined as

$$\mu_{\mathrm{VBF}} = \frac{N_{\mathrm{VBF}}^{\mathrm{meas.}}}{N_{\mathrm{VBF}}^{\mathrm{SM}}} = \frac{\sigma_{\mathrm{VBF}}^{\mathrm{meas.}} \cdot B_{H \to \gamma\gamma}^{\mathrm{SM}}}{\sigma_{\mathrm{VBF}}^{\mathrm{SM}} \cdot B_{H \to \gamma\gamma}^{\mathrm{SM}}}. \tag{43}$$

Here, $N_{\mathrm{VBF}}^{\mathrm{meas.}}$ gives the measured number of VBF events, assuming the correctness of the Standard-Model prediction for a certain branching ratio, in this case the branching ratio $B_{H \to \gamma\gamma}$ for the decay mode $H \to \gamma\gamma$. The predicted number of VBF events is given by $N_{\mathrm{VBF}}^{\mathrm{SM}}$. In addition to the uncertainties, also a result for the VBF signal strength itself, computed using simple cuts on τ_2, will be presented. For the purpose of comparison, the recent $H \to \gamma\gamma$ coupling analysis paper will be outlined, with focus on its method for the determination of the VBF signal strength. The determination of the VBF signal strength as performed in this thesis will be described in the same section.

Before these topics can be addressed, the Higgs vertex selection and the basic properties of the event shape will be analyzed. The event shape τ_2 will be introduced and defined. Its spectrum will be shown for both simulated vector boson fusion and gluon fusion event samples. Based on these spectra, the characteristics of possible τ_2-based selections will be discussed. The τ_2 resolution and its contributions will be determined. After that, the measurement of VBF signal strength using 8 TeV and some of the contributions to its uncertainty will be discussed.

3.2 Dataset and Monte-Carlo Simulations

3.2.1 Dataset

The dataset used for this analysis contains events of pp collisions at 8 TeV, which have been triggered by the diphoton trigger. The trigger threshold on the transverse energy E_T is 35 GeV and 25 GeV for the leading[34] and sub-leading photon, respectively. Additionally, these two photons need to fulfill loose criteria in the high level trigger, i.e. L2 and Event Filter, which ensure that the photon candidate's shower shape in the calorimeter is similar to the expected shower shape of a photon. Finally, data quality requirements are applied to ensure that all subdetectors were fully operational. The resulting integrated luminosity is equal to $20.3\,\mathrm{fb}^{-1}$. However, due to technical issues[35], the data analyzed in this thesis does only contain 75.7 % of the total integrated luminosity, corresponding to $15.4\,\mathrm{fb}^{-1}$.

3.2.2 Monte-Carlo Simulations

In addition to data events, Monte-Carlo simulations are used to better understand and interpret the results obtained from data. Monte-Carlo simulations allow for the prediction of cross sections, detector response studies and simulation of signal and background processes. Theoretical calculations as well as physical models are implemented in the simulation algorithms. One can divide the production of Monte-Carlo simulations into three parts:

- Event generation, which consists of translating matrix element from Feynman diagrams at a given order in perturbation theory into parton-level events. These parton-level particles then undergo parton showering and hadronization.

- Simulation of interactions of the particles produced in the event generation detector with the detector.

- Digitization of simulated energy depositions in the detector components, leading to quantities that can be reconstructed like data.

---

[34]The *leading* photon (or jet) is defined as the photon (or jet) with the highest transverse momentum. Accordingly the sub-leading photon (or jet) is defined as the photon (or jet) with the second-highest transverse momentum.
[35]The simulation files had to be reproduced to include the track information, which is needed for the study of τ_2. Unfortunately, this production suffered from technical problems with the ATLAS production system.

The Monte-Carlo simulations which are used in this analysis contain events in which a Higgs boson with a mass of 125 GeV are produced and subsequently decays to two photons. These $H \rightarrow \gamma\gamma$ simulations are available for all five Higgs production modes. Minimum-bias events and the underlying event are simulated using `PYTHIA8` [42]. Gluon fusion events are produced by using `POWHEG-BOX` [43]–[48] interfaced with `PYTHIA8`. The former produces parton-level events at NLO, while the latter simulates the showering of the partons, the hadronization and the underlying event. VBF events are also produced using `POWHEG-BOX` [46] interfaced with `PYTHIA8`. Events in which the Higgs boson is produced in association with a W or Z boson are generated by `PYTHIA8`. Events of the production mode $t\bar{t}H$ are produced by a combination of the `POWHEL` and `HELAC-NLO` [49] generators which is interfaced with `PYTHIA8`. The parton distribution function set is `CT10` [50] for the events generated with `POWHEG-BOX` and `CTEQ6L1` [51] for events generated with `PYTHIA8`. The events of the Monte-Carlo sample are weighted such that the the Monte-Carlo simulation corresponds to what is expected for data. The primary-vertex positions are weighted such that the distribution of primary vertices matches the measured distribution which has a RMS length of 4.8 cm [2]. Weights are also applied in order to reproduce the distribution of the average number of pp-collisions per bunch crossing in data. Only stable particles with a lifetime longer than 10 ps enter the detector simulation, which is performed by `GEANT4` [52]. The detector signals are then treated by the same object reconstruction algorithms as used for data events.

When results from Monte-Carlo samples are combined with data, the number of events in Monte-Carlo samples will be scaled down to the available 75.7 % of total integrated luminosity in data. Background shapes of invariant diphoton mass spectra are estimated directly from data.

3.3 Preselection of Events

The following requirements are imposed both at reconstruction and at truth level. Only events with at least two reconstructed and identified photons are taken into account. Photons from the η region of $1.37 < |\eta| < 1.56$ are not considered; the pseudorapidity region of $1.37 < |\eta| < 1.56$ is excluded because it corresponds to the transition region between barrel and end-cap calorimeter, in which much upstream material is located in front of the calorimeter, which in turn interferes with a precise measurement of photon candidates' properties. Moreover, the region of $|\eta| > 2.37$

is excluded because of the relatively coarse η-granularity in that detector region, which does not allow for an efficient rejection of fake photons.

The two photons with highest transverse momentum are considered to be the candidates which constitute the Higgs decay products. These photons need to pass tight identification cuts on the shower shape and to fulfill isolation criteria, see section 2.7.2. The invariant mass of the diphoton system is given by

$$m_{\gamma\gamma} = \sqrt{2E_1 E_2 (1 - \cos(\alpha))} = \sqrt{2E_{\mathrm{T},1} E_{\mathrm{T},2} (\cosh(\eta_1 - \eta_2) - \cos(\phi_1 - \phi_2))}. \qquad (44)$$

Here, E_i denotes the energy of the two leading photons and α is the angle between these two photons. This angle can be expressed in terms of the difference in pseudorapidity η_i and in azimuthal angle ϕ_i, where $i = 1$ for the leading and $i = 2$ for the sub-leading photon. The leading and sub-leading photon are required to have a transverse energy of larger than $0.35\,m_{\gamma\gamma}$ and $0.25\,m_{\gamma\gamma}$, respectively, and the invariant mass of the diphoton system must be in the range of $105\,\mathrm{GeV}$ to $160\,\mathrm{GeV}$.

3.4 Vertex Selection

As mentioned in section 2.7.1, one of the reconstructed primary vertices will be identified as the Higgs vertex. The selection of the correct interaction vertex is crucial if one wants to assign the correct tracks and jets to the Higgs event. The figure of merit is the vertex selection efficiency; it can be studied using Monte-Carlo simulations, and is here defined as

$$\varepsilon_{\mathrm{vx}} = \frac{\#\,\text{events in which}\,|z_{\mathrm{Hvtx}}^{\mathrm{truth}} - z_{\mathrm{Hvtx}}^{\mathrm{reco.}}| < \Delta z}{\#\,\text{events}}. \qquad (45)$$

Here, the true z-position of the Higgs vertex is denoted by $z_{\mathrm{Hvtx}}^{\mathrm{truth}}$ and the position of the vertex which is selected to be the Higgs vertex by the Higgs-vertex selection method is denoted by $z_{\mathrm{Hvtx}}^{\mathrm{reco.}}$. For the purpose of checking whether a reconstructed vertex which has been selected to be the Higgs vertex is correctly chosen, a Δz of $0.3\,\mathrm{mm}$ is used, as it is done in the standard couplings analysis [2]. It is necessary to know whether the resolution of the measurement of the Higgs vertex' z-position is small enough so as to not influence this estimate of the vertex selection efficiency. The resolution depends on the number and the sum of the squared transverse

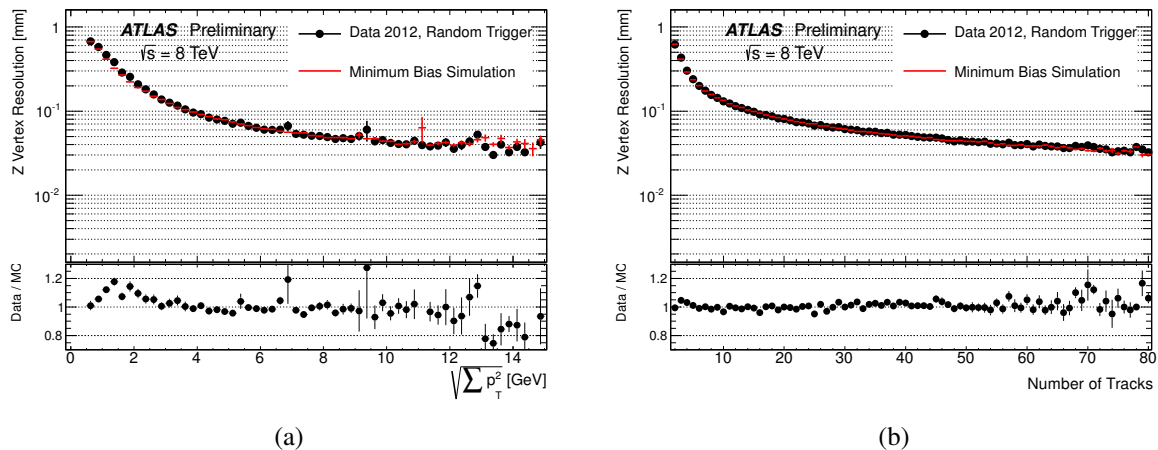momenta of tracks associated with the Higgs vertex, see figure 17. The distribution of the

FIG. 17: Vertex z-position resolution as function of summed track squared transverse momenta $\sum p_T^2$ (a), and as function of track multiplicity per vertex (b) [39]. Note that the track selection on which these results are based is not the same as in the vertex reconstruction of the events used in this analysis; a lower p_T threshold of 0.4 GeV has been used for these plots.

number of tracks which are associated with the Higgs vertex and of their corresponding $\sum p_T^2$ is shown in figure 18 and 19 for an inclusive 0-jet selection and for an inclusive 2-jet selection, respectively. Since in the later analysis of the event shape τ_2 only events with at least two jets will be considered, see section 3.5.1, the 2-jet-inclusive case is more relevant in this analysis. In combination with the resolution plots in figure 17, one can draw the conclusion that the resolution on the z-position of the Higgs vertex is about 0.04 mm and thus considerably smaller than the window size $\Delta z = 0.3$ mm in the vertex selection efficiency. This means that the resolution has practically no influence on the efficiency determination.
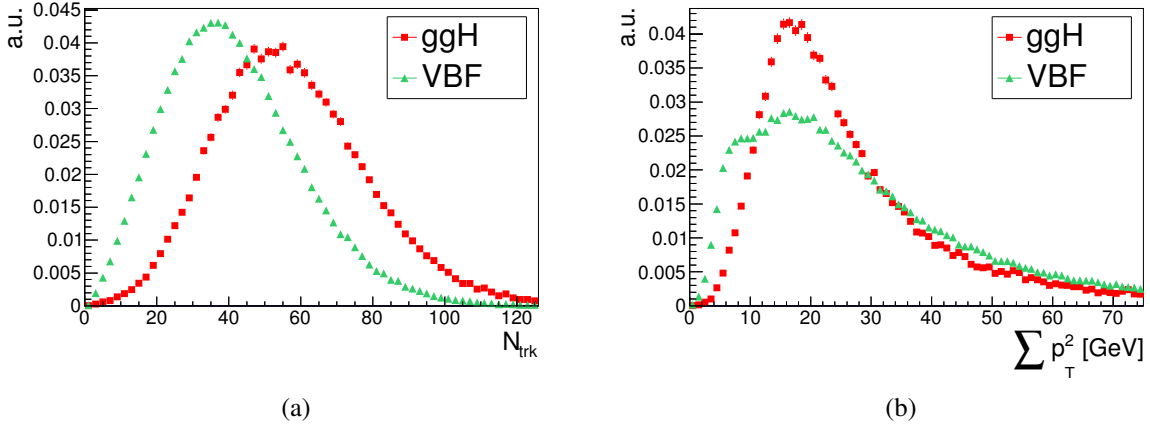
(a)

(b)
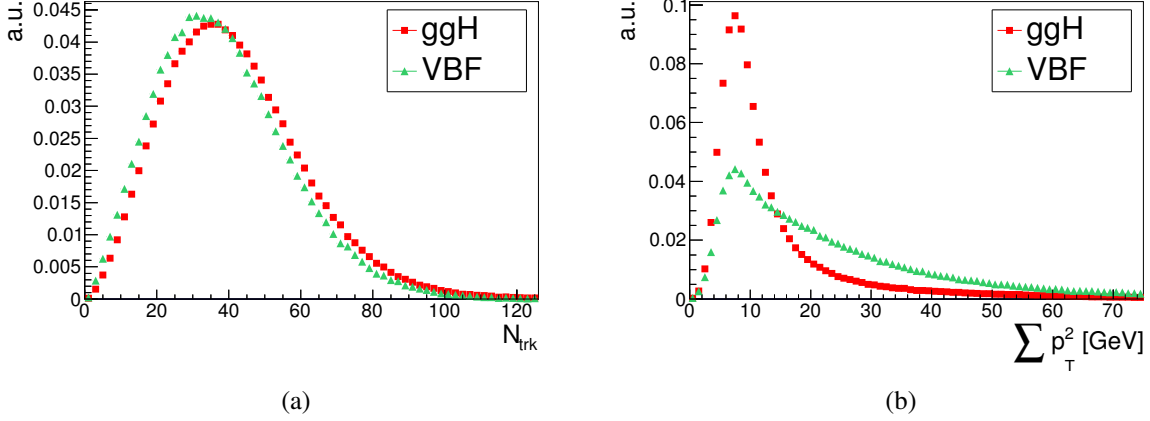
FIG. 18: Normalized distribution of the number of reconstructed tracks per Higgs vertex (a) and normalized distribution of the sum of squared transverse momenta of tracks associated with the Higgs vertex at reconstruction level (b). Only vertices with $|z_{\mathrm{H\,vtx.}}^{\mathrm{truth}} - z_{\mathrm{H\,vtx.}}^{\mathrm{reco.}}| < 0.3\,\mathrm{mm}$ have been selected. No restriction on the number of jets is applied.

(a)

(b)

FIG. 19: Normalized distribution of the number of reconstructed tracks per Higgs vertex (a) and normalized distribution of the sum of squared transverse momenta of tracks associated with the Higgs vertex at reconstruction level (b). Only vertices with $|z_{\mathrm{H\,vtx.}}^{\mathrm{truth}} - z_{\mathrm{H\,vtx.}}^{\mathrm{reco.}}| < 0.3\,\mathrm{mm}$ have been selected. At least two jets are required at reconstruction level.

The vertex selection efficiency is expected to depend on the number of pile-up vertices. The number of reconstructed vertices N_{PV} is highly correlated with the expected number of pp interactions per bunch crossing, μ; however, N_{PV} tends to be smaller than μ, especially in events with much pile-up. The number of reconstructed primary vertices is a measure of the amount of pile-up in the event, whereas μ is a measure for the average amount of pile-up. One can see the distribution of μ for the 2012- (and 2011) dataset in figure 20, while in figure 21 the distribution of the number of reconstructed primary vertices is displayed. When there is much

pile-up in the event, i.e. many additional soft *pp* interactions, the mean distance between the interaction vertices is smaller, leading to enhanced confusion about which track originated from which vertex and to a higher probability of vertices being merged in the process of reconstruction. Therefore, the vertex selection efficiency will be studied in the following as a function of the number of reconstructed vertices.
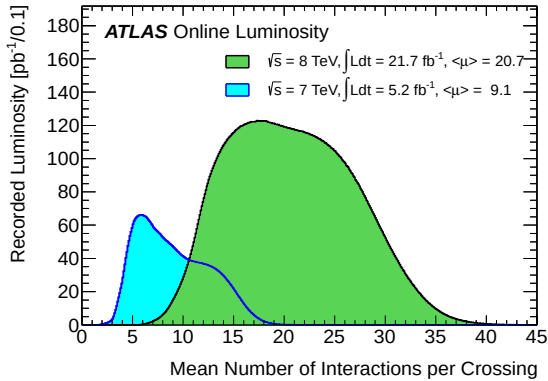
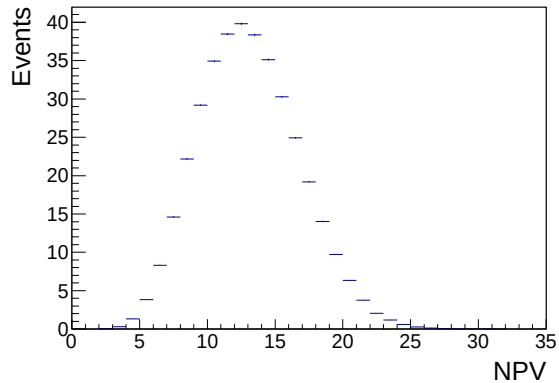

FIG. 20: Mean number of interactions per bunch crossing in the 2012- and 2011 dataset [41].

FIG. 21: Number of reconstructed primary vertices for 8 TeV Monte-Carlo simulations.

In figure 22a, the vertex selection efficiency for Higgs events is shown as a function of the number of reconstructed primary vertices N_{PV}, including all five Higgs production modes and for different methods of Higgs vertex selection. The method which employs a neural network (in the legend denoted as N.N.) leads to the highest vertex selection efficiencies. This method is used as the standard vertex selection method in the $H \to \gamma\gamma$ analysis; for a description see section 2.7.1. In other analyses it is common to select the vertex with the maximal summed squared transverse momentum of associated tracks, in the following denoted by the term $\sum p_{T}^2$-*method*. This method is commonly used to determine the hard-interaction vertex; in the $H \to \gamma\gamma$ analysis, however, this method is not optimal as explained in section 2.7.1. A third possibility of vertex position determination is to use *photon pointing*. This method uses the segmentation of the calorimeter and, if available, the photon conversion vertex of converted photons for an extrapolation of the photon trajectories in order to estimate the position of the position of the vertex from which the photons originate. For the purpose of selecting the correct hard-interaction vertex, it is not an adequate method, as one can see. It is a general tendency of the vertex selection efficiency to decrease with increasing number of reconstructed events, N_{PV}, with the exception of photon pointing, which is very robust against the influence of pile-up.

The same types of efficiencies are shown in figure 22b for events with at least two jets. In this case, the $\sum p_T^2$-method leads to vertex selection efficiencies which are nearly as high as for the neural network. Except for the pointing method, the efficiencies are increased compared to the case of the inclusive 0-jet selection. One can conclude from this figure that the vertex selection efficiency of the selected events in this analysis is 93.5 % at the most probable value of N_{PV}, which is 13, and is only weakly depending on the amount of pile-up.
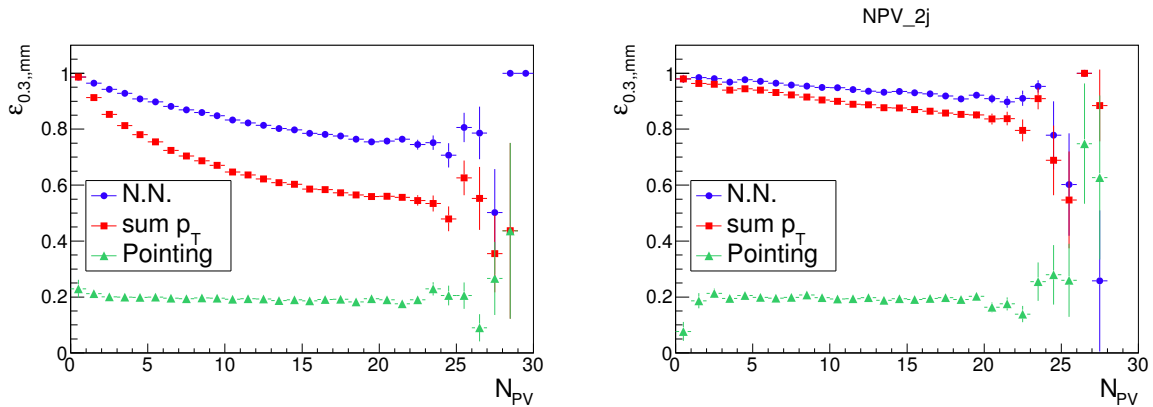
(a) Vertex selection efficiency for all Higgs production modes combined. No restriction on the number of jets.

(b) Vertex selection efficiency for all Higgs production modes combined. At least two jets are required.
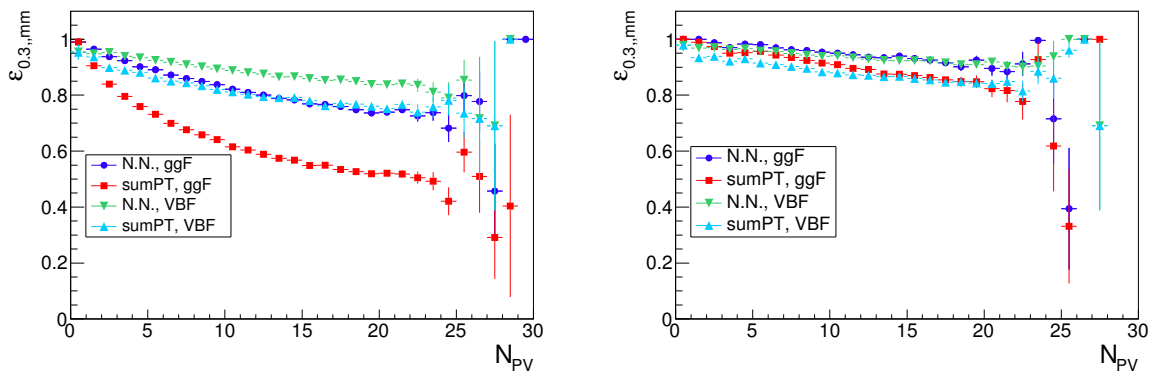
(c) Vertex selection efficiency for the two leading Higgs production modes, gluon fusion and vector boson fusion. No restriction on the number of jets.

(d) Vertex selection efficiency for the two leading Higgs production modes, gluon fusion and vector boson fusion. At least two jets are required.

FIG. 22: Vertex selection efficiency using different vertex reconstruction methods. *Final* denotes the outcome of the neural network (see section 2.7.1), which is used for the determination of the Higgs vertex in the $H \rightarrow \gamma\gamma$ analysis. The case in which the vertex with the maximal summed squared transverse momenta of tracks associated with the vertex is chosen as Higgs vertex is denoted by *sum p_T*. This is the standard method of selecting the hard-interaction vertex in the ATLAS experiment. The values titled with *Pointing* rely only on photon information from the calorimeter and, in case of converted photons, the Inner Detector.

In figure 22c and 22d the same types of efficiencies are shown, but for ggF and VBF events separately. Using an inclusive 0-jet selection, the efficiency is significantly higher for VBF if one uses the neural network or the $\sum p_T^2$-method. This can be explained with the higher $\sum p_T^2$ of VBF events, see figure 18b. If at least two jets are required, see figure 22d, the vertex selection efficiency is increased for the neural-network- and the $\sum p_T^2$-method, as is expected from the fact that Higgs events with more jets also tend to have more tracks and hence a larger $\sum p_T^2$; and, contrary to the 0-jet inclusive case, in this case the vertex selection efficiency tends to be a bit higher for ggF events. This can be understood by considering the fact that most VBF events contain at least two jets, and therefore the inclusive 2-jet selection does not enhance the fraction of events with at least two jets as much as it does for ggF event samples.

3.5 Selection of Vector Boson Fusion Events and Signal Strength Measurement

In the following, the kinematic properties of gluon fusion and vector boson fusion events will be discussed. The comparison of these properties for ggF and VBF events will result in an additional preselection cut which enriches the selected event sample with VBF events. After that, the analysis which has been done in the standard coupling paper [2] will be outlined, including the corresponding method of determining the VBF signal strength.

3.5.1 Kinematics of Gluon Fusion and Vector Boson Fusion

In this subsection, the transverse momentum distribution and pseudorapidity distributions of jets and charged particles coming from the Higgs vertex at truth level[36] will be shown for gluon fusion and vector boson fusion events. The p_T spectrum of charged particles at all pseudorapidities a truth level can be seen in figure 23a. These histograms are scaled by the inverse of the event numbers for gluon fusion and vector boson fusion, respectively. The total area enclosed by the histogram contours therefore corresponds to the mean number of particles coming from a Higgs vertex. At the same time, the bin contents correspond to the mean number of particles per event

---

[36]When quantities at truth level are considered, only events which fulfill the requirements on the two photons, see section 3.3, are considered.

in that particular bin. The fraction of particles with a high p_T is larger for VBF than for ggF events.

Figure 23b shows the η distribution of particles. The η spectrum for VBF events has a special shape, which reflects the fact that tracks and jets emerging from VBF events are emitted at rather high pseudorapidities and there is little hadronic activity in between. Since the Inner Detector acceptance in η is only $-2.5 < \eta < 2.5$, a relatively large fraction of particles is undetected by the Inner Detector: 50.1 % of particles in gluon fusion events and 52.9 % of the particles in vector boson fusion events are not within the Inner Detector acceptance.

(a)   (b)
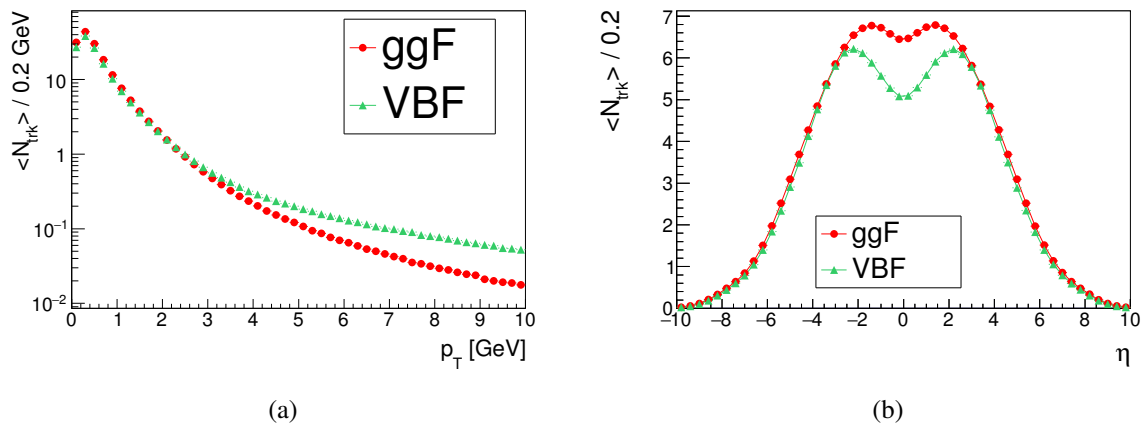
FIG. 23: Particle kinematics at truth level. The distributions are scaled by the inverse number of ggF and VBF events, respectively. No restrictions on the p_T or on η are applied; only charged particles are considered.

(a)   (b)
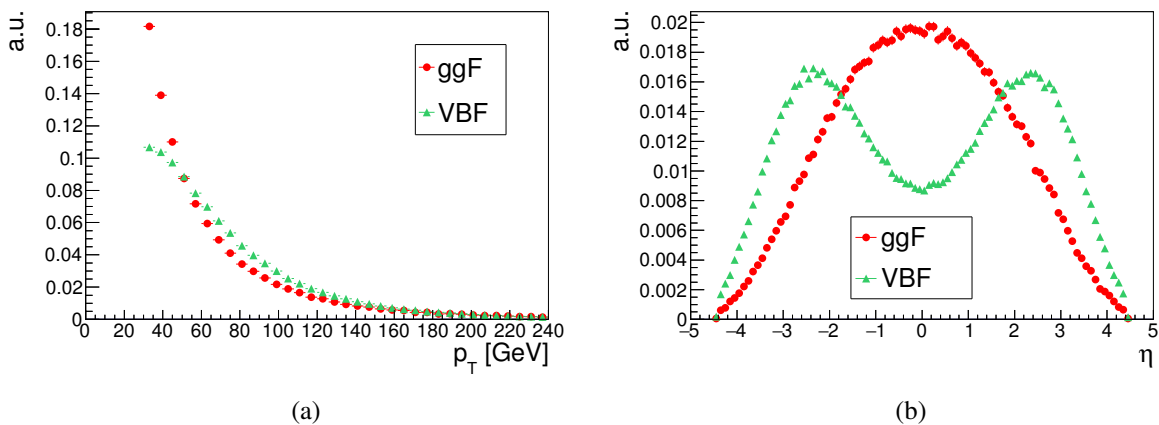
FIG. 24: Jet kinematics at truth level. Only the leading and sub-leading jets are considered. The distributions are normalized to 1.

The kinematic distributions of jets are shown in figure 24. The transverse momentum of VBF jets tends to be larger than that of ggF jets, which can be seen in figure 24a. A similar shape as in the distribution of the particles' pseudorapidity is also present in the corresponding distribution of the jets' pseudorapidities, see figure 24b. As can be expected from this distribution, the difference in pseudorapidity for the two leading jets tends to be larger for VBF events, which can be explicitly seen in figure 25. A fraction of 20 % of ggF jets is not within the Inner Detector acceptance, while this fraction is 36 % for VBF jets.
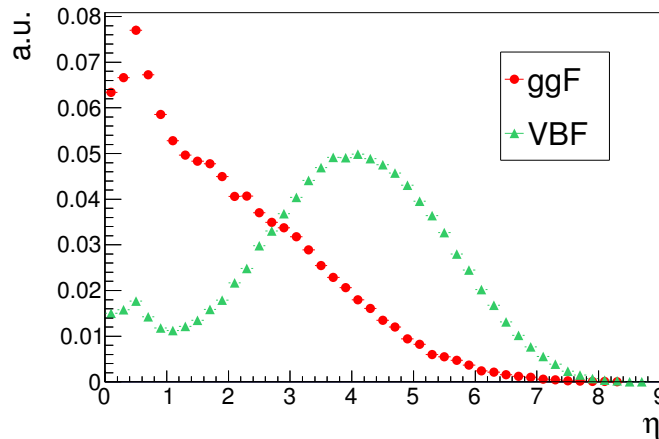
FIG. 25: Normalized distribution of the absolute difference in η between the two leading jets at truth level.

As described in section 3.3, so far only diphoton requirements have been imposed in the event selection. But since in this analysis an attempt is made to create an alternative VBF-enriched selection, it is useful to set constraints on jet-related properties of the event. In order to quantify the characteristics of a VBF-enriched selection, the *efficiency* and the *purity* are used.

- VBF-Efficiency $\varepsilon_{\mathrm{VBF}}$: The efficiency is defined as the fraction of all VBF events which are selected by a selection.

$$\varepsilon_{\mathrm{VBF}} = \frac{N_{\mathrm{VBF}}^{\mathrm{sel.}}}{N_{\mathrm{VBF}}}. \tag{46}$$

In a VBF-enriched selection it is useful to aim at a high VBF efficiency.

- VBF-Purity P_{VBF}: The purity quantifies how many of the selected events are signal events, in this case, VBF events. In this analysis, the gluon fusion background in a VBF-enriched selection is of special interest because of the high production cross section for gluon fusion

and the possibly large perturbative uncertainty on it. Therefore only the gluon fusion and not the other non-VBF Higgs production modes enter the following definition of the VBF-purity.

$$P_{\text{VBF}} = \frac{N_{\text{VBF}}^{\text{sel.}}}{N_{\text{VBF}}^{\text{sel.}} + N_{\text{ggF}}^{\text{sel.}}} \, . \tag{47}$$

In addition to a high VBF-efficiency, a high VBF-purity is desirable in a VBF-enriched selection. In reality, however, there will be a trade-off between the efficiency and the purity: The VBF-purity can be enhanced by applying tighter cuts on the event sample, but this would not only remove non-VBF events from the selection but also some VBF events, decreasing the VBF-efficiency.

Imposing lower bounds on the number of jets and on the separation in pseudorapidity between the two leading jets is an effective way to decrease the amount of gluon fusion and non-Higgs background events in the selection while preserving many of the VBF events. Only 10.8 % of reconstructed gluon fusion events and 11.2 % of data events, which consist mostly of non-Higgs events, contain more than one jet, whereas this fraction is 55.4 % for VBF events. This results in a VBF-purity of $P_{\text{VBF}} = 30.1$ %. Also, the computation of the 2-jettiness as it is implemented in this thesis requires at least two reconstructed jets. By imposing in addition the requirement $|\Delta\eta_{jj}| > 2.0$, only 4.6 % of ggF events, 3.6 % of data events, but 46.9 % of VBF events remain unrejected, which results in a purity in VBF of $P_{\text{VBF}} = 46.1$ %. If none of these jet cuts are applied, the purity in VBF as defined in equation 47 is expected to be merely $P_{\text{VBF}} = 7.71$ %. It is therefore an effective VBF-pre-enrichment to consider only events which meet the following criteria in the VBF selection:

- At least two reconstructed jets.

- A minimal separation in pseudorapidity between the leading and sub-leading jet of 2.0.

3.5.2 Vector Boson Fusion Selection and Signal Strength Measurement in the Standard $H \to \gamma\gamma$ Analysis

A part of this analysis is the construction and evaluation of an alternative VBF selection. In order to compare the alternative selection with an already existing selection, the VBF-categories used in the official $H \to \gamma\gamma$ couplings analysis [2] will be be reviewed. Moreover, the procedure to obtain signal strengths for individual Higgs production modes is summarized. The latest paper

treating the measurement of signal strengths in the ATLAS $H \to \gamma\gamma$ analysis is based on the 7 TeV and 8 TeV dataset. As is detailed in the cited paper, twelve exclusive event categories[37] are defined. These categories are designed such that each of them is enriched in a certain Higgs production mode. Each event passing the photon preselection will be associated with exactly one of these. Based on Monte-Carlo simulations one can determine how many events of each production mode are expected in each of the twelve categories. For each of the twelve categories a likelihood function $\mathscr{L}_c$ is defined. By maximizing the product of all these twelve likelihood functions $\mathscr{L}_c$, one can estimate the signal strengths of the different production modes. Each of the twelve likelihood functions has the form

$$\mathscr{L}_c = \mathrm{Pois}(n_c | N_c(\vec{\theta})) \cdot \prod_{i=1}^{n_c} f_c(m_{\gamma\gamma}^i, \vec{\theta}) \cdot G(\vec{\theta}). \tag{48}$$

The subscript c denotes the category. Examples of a category are the categories enriched in VBF events, i.e. *VBF tight* and *VBF loose*. These two categories are detailed below. The measured number of events in category c is labelled by n_c. The expected number of events in category c is denoted by N_c; it comprises the expected number of signal events from all the production modes, the number of background events[38] as well as the number of spurious signal events[39]:

$$N_c = \sum_p \mu_p N_{p,c} + N_{\mathrm{bkg},c} + N_{\mathrm{spur.},c} \cdot \theta_{\mathrm{spur.},c}. \tag{49}$$

The variable μ_p denotes the *signal strength* for the Higgs production mode labelled with p. If $\mu_p = 1$, the number of measured events for production mode p is equal to the number of events predicted by the Standard Model. The value of the probability density function for each diphoton event, labelled with i, with invariant diphoton mass $m_{\gamma\gamma}$ is denoted by $f_c(m_{\gamma\gamma})$. The variable θ represents nuisance parameters. These are parameters of the model that are known only with limited accuracy. This uncertainty is incorporated by including probability density functions $G(\theta)$, which means that these already measured nuisance parameters themselves can vary to

---

[37]Comparable to the term *selection*. The term *category* will only be used in the description of the official analysis.

[38]The expected number of background events is based on a parametrization of the background in each category.

[39]Spurious signal events quantify the systematic uncertainty on the chosen background parametrization. If, for example, the background model leads to the assumption of fewer background events in the signal region than actually true, this difference between expected and true background events will be interpreted as signal events, causing an overestimation of the number of signal events.

some extent in the process of the likelihood maximization. The normalized invariant diphoton mass distribution for a category c can be written as

$$f_c(m_{\gamma\gamma}^i) = \frac{(\sum_p \mu_p N_{p,c} + N_{\text{spur.},c} \cdot \theta_{\text{spur.},c}) f_{S,c} + N_{\text{bkg},c} \cdot f_{\text{bkg},c}}{N_c} . \tag{50}$$

The functions $f_{S,c}$ and $f_{\text{bkg},c}$ are normalized distribution functions for the Higgs signal and the background, respectively. For obtaining the individual signal strengths μ_p, one maximizes the product of the likelihood functions (48) for the different categories c.

Each diphoton event is distributed to exactly one of the twelve categories. In this process, it is first tested whether an event is passing the criteria for the categories with the smallest expected signal yield ($t\bar{t}H$, ZH and then WH). If an event fails to meet the corresponding conditions, it will be tested whether it matches the criteria for the VBF *tight* category. If this fails, the event is passed on to the VBF *loose* category. If the event does not fulfill either of the requirements of the two VBF categories, it is distributed to one of the *untagged* categories, which are expected to contain mostly gluon fusion events. The four untagged categories are based on the component of the diphoton momentum orthogonal to the diphoton thrust axis in the transverse plane[40] p_{Tt} and the pseudorapidity of the photons. Both VBF categories require

- at least two jets,

- a difference of the pseudorapidities of the two leading jets $|\Delta\eta_{jj}| > 2.0$,

- and $\eta^* = \eta_{\gamma\gamma} - \frac{\eta_{j1}+\eta_{j2}}{2} < 5.0$.

If the event passes these criteria, a *Boosted Decision Tree* (BDT) [53] is applied to obtain a number O_{BDT} which summarizes the probability that a given event is a VBF event. This multivariate analysis is based on

- the invariant dijet mass of the two leading jets, m_{jj},

- $|\Delta\eta_{jj}|$,

- η^*,

- the azimuthal angle between the dijet and the diphoton system $\Delta\phi_{\gamma\gamma-jj}$,

---

[40]It is defined as $p_{\text{Tt}} = |(\vec{p}_T^{\gamma1} + \vec{p}_T^{\gamma2}) \times \vec{t}|$ with the thrust axis in the transverse plane $\vec{t} = (\vec{p}_T^{\gamma1} - \vec{p}_T^{\gamma2})/|\vec{p}_T^{\gamma1} - \vec{p}_T^{\gamma2}|$.

- the minimal angle between each of the leading photons and each of the two leading jets $\Delta R_{\gamma,j}^{\min}$ and

- p_{Tt}.

A given event will be part of the VBF *tight* category, if the BDT output O_{BDT} is higher than 0.83, while a value of $0.3 < O_{\text{BDT}} < 0.83$ leads to a VBF *loose* categorization. These two definitions of VBF categories have the following VBF-efficiencies ε_{VBF} and VBF-purities P_{VBF}:

- VBF *tight*: $\varepsilon_{\text{VBF}} = 6.4\%$, $P_{\text{VBF}} = 80.5\%$

- VBF *loose*: $\varepsilon_{\text{VBF}} = 7.2\%$, $P_{\text{VBF}} = 56.5\%$

3.5.3 A Simple Cut-Based Approach

In this analysis, a less sophisticated method than described in the preceding part will be used. No maximum-likelihood method will be used and only one category instead of twelve categories will be considered. A simple cut-based selection will be used to study the use of the 2-jettiness τ_2, defined in section 3.6 for the definition of a category enriched in VBF events. The VBF signal strength and its corresponding uncertainty is computed as follows in this analysis:

$$\mu_{\text{VBF}} = \frac{N_H^{\text{data}} - N_{\text{ggF}}^{\text{MC}} - N_{WH}^{\text{MC}} - N_{ZH}^{\text{MC}} - N^{\text{MC}}}{N_{\text{VBF}}^{\text{MC}}} \, . \tag{51}$$

$$(\Delta\mu_{\text{VBF}})^2 = \frac{1}{(N_{\text{VBF}}^{\text{MC}})^2} \left[(\Delta N_H^{\text{data}})^2 + (\Delta N_{\text{ggF}}^{\text{MC}})^2 + (\Delta N_{WH}^{\text{MC}})^2 + (\Delta N_{ZH}^{\text{MC}})^2 + (\Delta N^{\text{MC}})^2 \right]$$
$$+ \left(\frac{\Delta N_{\text{VBF}}^{\text{MC}}}{(N_{\text{VBF}}^{\text{MC}})^2} \right)^2 \left(N^{\text{data}} - N_{\text{ggF}}^{\text{MC}} - N_{WH}^{\text{MC}} - N_{ZH}^{\text{MC}} - N^{\text{MC}} \right)^2 \, . \tag{52}$$

There are more uncertainties to be studied than those appearing this equation, but this is not within the scope of this thesis. The uncertainties included here are the ones that are most dependent on the specifics of the VBF selection. The background will parametrized by an analytic function. The shape of the Higgs peak will be determined using Monte-Carlo simulations. Using these parametrizations, the invariant diphoton mass spectrum will be fitted with a sum of the background- and Higgs-signal parametrization. From this fit, the number of Higgs events, N_H^{data},

can be taken. In order to compute the number of VBF events in the selection, the expected number of non-VBF Higgs events will be subtracted from the number of Higgs events, assuming the Standard Model predictions for production cross sections to be correct.

In order to compute the uncertainty in equation (52), it is necessary to know ΔN_H^{data} and ΔN_i^{MC}, where i stands for the Higgs production modes. The latter uncertainties ΔN_i^{MC} contain a statistical and a theoretical uncertainty and are computed as follows:

$$\Delta N_i^{\text{MC}} = \sqrt{(\Delta N_i^{\text{MC}}|_{\text{stat.}})^2 + (\Delta N_i^{\text{MC}}|_{\text{theo.}})^2}. \tag{53}$$

The theoretical uncertainty in turn is composed of a perturbative uncertainty, which is obtained by variations of unphysical scales as described in section 1, and of a parametric uncertainty, consisting of uncertainties on the parton distribution functions and the strong coupling constant α_s. In case of the gluon fusion contribution to the VBF selection, the application of the ST procedure as described in section 1.2 is necessary. The determination of this uncertainty is presented in section 3.10. All other theoretical uncertainties are taken from [4], as done in [2]. The uncertainty on the Higgs signal yield, ΔN_H^{data}, depends on the invariant mass spectrum in data and will be determined in section 3.11.2. All of these uncertainties are added in quadrature, similar to what is done in the coupling analysis described in section 3.5.2.

Thus, several quantities have influence on the uncertainty $\Delta\mu_{\text{VBF}}$. Especially the perturbative uncertainty on the gluon fusion contamination and the statistical uncertainty on the fitted number of Higgs events are of importance for the creation of a VBF selection. The statistical uncertainty is connected with the fraction of Higgs events in the signal region of the invariant diphoton mass spectrum, while the former is connected with the purity in VBF and with the phase-space restrictions of the VBF selection.

The outcome of this estimation of μ_{VBF} relies on the correctness of the assumption that the signal strengths of non-VBF Higgs production modes are as expected in the Standard Model. This is a disadvantage, because especially the gluon-fusion production mode is vulnerable to influences of new physics as it contains a loop. In general, the above mentioned analysis [2] has a more performant approach on the measurement. However, a full categorized analysis along the lines of [2] is beyond the scope of this thesis. Nevertheless, the use of the 2-jettiness for a VBF selection can be studied also with this simple method.

3.6 The *N*-Jettiness: τ_N

3.6.1 Introduction

The observable *N*-jettiness, denoted by τ_N, is an inclusive event shape and introduced in [5]. The *N*-jettiness quantifies how much a given event looks like an event with exactly *N* very narrow jets. This information is encoded in terms of a real number. The *N*-jettiness vanishes if there are exactly *N* narrow jets in the event, whereas large values indicate considerable amounts of additional radiation. The additional radiation may be or may be not reconstructed as additional jets, it enters the calculation of τ_N either way.

Being inclusive, all tracks coming from the Higgs vertex are considered in the computation of τ_N. Ideally, not only charged particles, which lead to tracks, but also neutral particles from the hard-interaction vertex would enter this event shape. But charged particles are the only sort of particles that can be assigned to an individual vertex with high reliability. Hence, the use of neutral particles would make the computation sensitive to pile-up. At truth-level, however, neutral particles can be considered as well. The two Higgs candidate photons are always disregarded for the computation of τ_N since they are not part of the hadronic activity. If not otherwise stated, only charged particles or tracks which fulfill the following requirements are used for the coming studies.

- Transverse momentum: $p_T > 0.5\,\text{GeV}$

- Pseudorapidity: $|\eta| < 2.5$

In figure 26, a generic dijet-event is sketched. One way to characterize this event is to count the number of reconstructed jets. Another way would be to use the *N*-jettiness as a measure of the jet activity and of additional hadronic radiation.

The number of jets identified in an event depends on the specifics of the jet reconstruction. Roughly speaking, a spray of hadrons will be reconstructed as jet if it has a transverse momentum larger than a certain value within a cone of a certain size. These values contain no absolute meaning. They might be 5 % smaller or bigger and the number of jets would change accordingly[41]. The mere number of jets is therefore a complicated measure. The *N*-jettiness gives more

---

[41]Still, these values are not arbitrarily chosen, but the result of theoretical considerations and are based on reconstruction and calibration performance.

inclusive information about hadronic radiation because it does not rely on the details of the jet reconstruction and in principle takes into account all detected particles. Still, the axis resulting from the jet reconstruction algorithm are useful for the computation of the N-jettiness, which requires N jet axes[42].
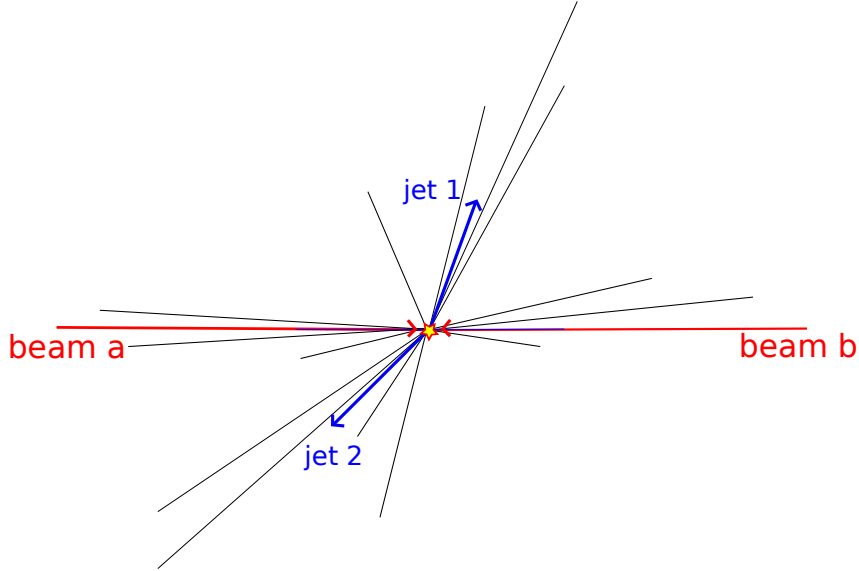

FIG. 26: Display of a generic event in which one or more jets could be defined.

The minimization of the N-jettiness of a given event corresponds to dividing the full solid angle of 4π into $N + 2$ regions, i.e. N jet regions and two beam regions. Each track assigned to the hard-interaction vertex is thus assigned to one of the N jets or to one of the two beam regions. The result of this is that each of the $N + 2$ jet- and beam directions is the seed of a cluster of tracks which are *closest* to the respective jet or beam. The distance measure is given by the four-product between two Lorentz vectors. This assignment is performed for each individual track by determining the minimal four-product between the track and all $N + 2$ jet- and beam directions. The jet or beam with which the minimal four-product is performed, will be the region to which the track is assigned. To understand why the minimization process leads to the association of tracks to nearby jets or beams, figure 27 and equation (54) may be helpful. The smaller the angle between the jet axis and the jet constituents and/or the softer the jet constituents are, the smaller the corresponding Lorentz product between the jet axis and the jet constituents will be, leading to a smaller τ_N.

---

[42]These axes can also be obtained by a minimization of τ_N, but this method has not been implemented in this analysis.
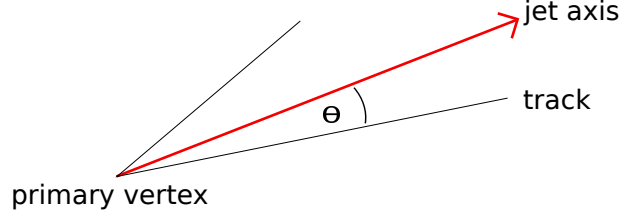
FIG. 27: A small jet and its constituents.

The four-product of a track and a normalized jet direction is given by following equation:

$$n_j^{\mu} \cdot p_{\mu} = E_k \left(1 - \cos(\theta)\right).$$

(54)

In this equation, the jet- or beam axis is given by the normalized Lorentz vector n_j^{μ}, the Lorentz vector and energy of the track is denoted by p_{μ} and E_k, respectively, and the angle between jet axis and track is given by θ. When this product is small there are three possible reasons for that:

- The angle between track and jet or beam is small.

- The track is soft.

- The track is soft *and* the angle between the track and jet or beam is small.

VBF events tend to look like two quite narrow jets more than most other events, including gluon fusion events, therefore an exclusive 2-jet cut is useful to enrich a sample in VBF events. This cut can be implemented using the 2-jettiness.

3.6.2 Definition

There is more than one way to define the *N*-jettiness. These ways are differing in the normalization of the jet Lorentz vectors. Different normalizations lead to different shapes of the jet areas. Equation (55) used in this thesis leads to roughly circular areas which are of comparable size in different regions of pseudorapidity. This version of normalization is called *geometric measure*.

The 2-jettiness is computed as follows [54]:

$$\tau_2 = \sum_k^{N_{\text{trk}}} \min \left\{ n_{a,\mu} \cdot p_k^\mu, n_{b,\mu} \cdot p_k^\mu, \frac{n_{1,\mu} \cdot p_k^\mu}{\rho}, \frac{n_{2,\mu} \cdot p_k^\mu}{\rho} \right\}$$
$$= \sum_{k \in \text{jets}}^{N_{\text{trk}}} \min\{\cdots\} + \sum_{k \in \text{beams}}^{N_{\text{trk}}} \min\{\cdots\}$$
$$= \tau_2^{\text{jets}} + \tau_2^{\text{beams}} . \tag{55}$$

The n_μ denote the normalized Lorentz vectors of the beam- and jet directions. They are normalized such that $n_\mu = (1, \vec{n})$. The subscripts a and b label the two beam directions: $n_{a,\mu} = (1, 0, 0, 1)$ and $n_{b,\mu} = (1, 0, 0, -1)$. The vector of the leading and sub-leading jet is denoted by $n_{1,\mu}$ and $n_{2,\mu}$, respectively. The track Lorentz vectors are denoted by p_k^μ.

The angular size of the jet regions is controlled by the factor of $\frac{1}{\rho}$. The larger ρ, the smaller the products of tracks with jets are, therefore they are more likely to be the minimal product, which in turn leads to the tendency of more tracks being associated with one of the two jet directions. Thus, jet regions are getting larger when ρ is increasing. In figure 28 the influence of ρ on the outcome of the track association is shown: Two maps in η and in ϕ can be seen, in which all reconstructed tracks are indicated. The tracks assigned to one of the two jet directions are colored green and blue and are represented by triangular markers, while the tracks which are assigned to the two beam directions are colored black and red, respectively, and are represented by circular markers. The left plot shows the map for $\rho = 0.5$, the right one for $\rho = 1.0$. In the following, the value for the jet size parameter is chosen to be $\rho = 0.5$ if not otherwise stated. This value is close to the distance parameter $R = 0.4$ in the anti-k_{T} jet finding algorithm, therefore it is a good starting point.

In the second and third line of equation (55), a division of the total 2-jettiness into a beam and a jet part of τ_2 is performed. Doing so, one can draw additional information about the event kinematics from τ_2: The 2-jettiness can be big because the beam part is big, because the jet part is big or because both are big. But the beam part is typically much larger than the jet part, and so the information about the jet part is shadowed by the size of the beam part if τ_2 in total is considered. By considering each part of τ_2 individually, this can be avoided. Widely-spread jets result in large values of τ_2^{jets}, while a large amount of hadronic initial state radiation, which is

71

unlikely to be concentrated in the jet direction, or the presence of additional jets leads to large values of τ_2^{beams}.

If not otherwise stated, only tracks and particles which fulfill the following requirements are considered for the following studies.

- Transverse momentum: $p_{\text{T}} > 0.5\,\text{GeV}$

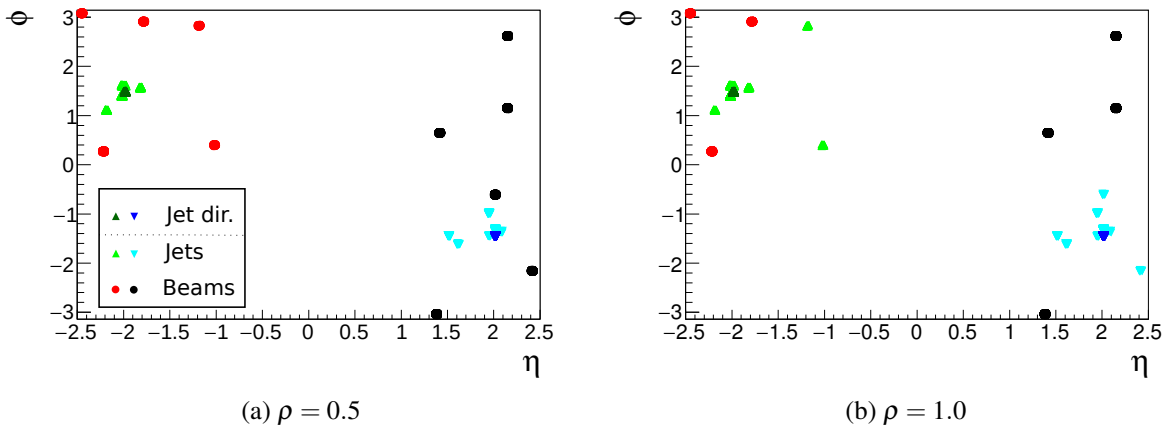- Pseudorapidity: $|\eta| < 2.5$

- Charge: Only charged particles

(a) $\rho = 0.5$ (b) $\rho = 1.0$

FIG. 28: Maps in η and ϕ showing the positions of all reconstructed tracks in an event with two reconstructed jets. The colors and shapes indicate the assignment in the course of the τ_2 algorithm: Green (upward triangle) and blue (downward triangle) tracks are assigned to one of the two leading jets, while red and black circles correspond to tracks which have been assigned to one of the two beam jets. The darker markers within the jet areas indicate the direction of the reconstructed leading jets.

The determination of the jet directions by minimizing τ_2 would eliminate the dependence on the jet reconstruction algorithm. The implementation of a 2-jettiness minimization was not in the scope of this thesis, therefore the reconstructed jet directions have been used. These jet directions are taken as the starting points of an iteration which aims at getting closer to the jet directions that would result from a stand-alone minimization of the 2-jettiness. First the tracks are assigned to either one of the two beam regions or to one of the two jet regions on basis of the reconstructed jet direction. After that, the jet direction is recomputed by the following equation:

$$\vec{n}_{\text{jet}} = \frac{\sum_{\text{trk}\in\text{jet}} \vec{p}_{\text{trk}}}{|\sum_{\text{trk}\in\text{jet}} \vec{p}_{\text{trk}}|}, \tag{56}$$

72

where *i* runs over all tracks assigned to the given jet. The disadvantage of this recomputation of the jet direction is that the neutral particles are not contributing to the iteration process.

3.7 The Spectrum of the 2-Jettiness

3.7.1 Spectrum of the 2-Jettiness for Gluon Fusion and Vector Boson Fusion Events

The amount of additional gluon radiation is expected to be larger for gluon fusion events than for vector boson fusion events. This is a consequence of the differing color factors of the incoming particles. As could be seen in section 1, gluons are the initial-state particles of gluon fusion, whereas quarks are the initial-state particles for vector boson fusion. The color factor for the 3-gluon vertex is $\frac{9}{4}$ times larger than for the corresponding vertex of a quark emitting a gluon. Therefore the initial-state radiation is weaker for VBF than for ggF. While gluon fusion is a process involving the strong force at leading order, vector boson fusion is to first approximation an electroweak process.

The spectrum of the 2-jettiness, i.e. the sum of the beam and jet part of the 2-jettiness, is shown in figure 29. It is useful to discuss its components τ_2^{beams} and τ_2^{jets} individually. Initial-state radiation will mainly contribute to τ_2^{beams}, since there is no reason to believe that initial-state radiation will be predominantly emitted in the direction of the hard jets. The other type of additional gluon radiation is final-state radiation: In VBF events, the outgoing quarks again are modest emitters of additional gluons. Thus, VBF jets are expected to be rather narrow, corresponding to a relatively small τ_2^{jets}. In gluon-fusion events, only gluon jets are possible, such that the jets in gluon-fusion events will be less collimated due to the large gluon color factor.

So one can summarize: The beam part as well as the jet part of the 2-jettiness are expected to be larger for ggF events than for VBF events. This can be seen in the spectra of τ_2^{beams} and τ_2^{jets} in figure 30. In general the events contributing to these spectra were generated to include *multi-parton interactions*, if not otherwise stated. The definition of these interactions and their influence on the τ_2 spectrum will be detailed later in section 3.7.5.
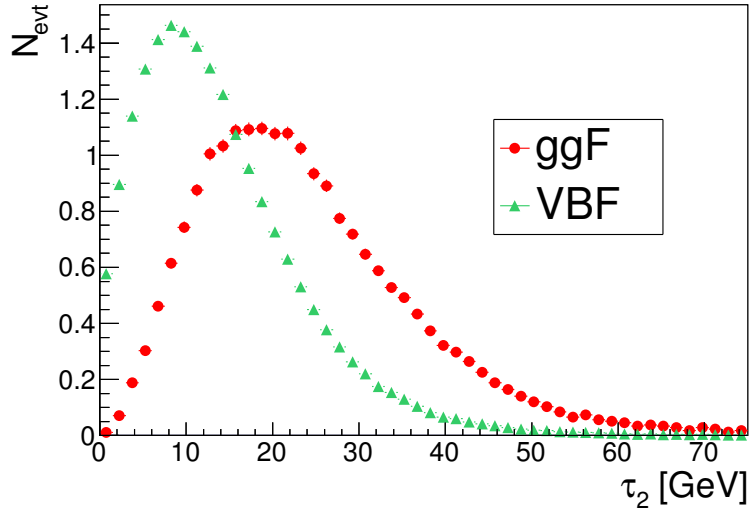
FIG. 29: Spectrum of the 2-jettiness τ_2 for ggF and VBF events at truth level, normalized to the integrated luminosity. Only charged particles within the Inner Detector acceptance with $p_T > 0.5\,\text{GeV}$ are considered.

The spectrum which is shown in figure 30b features a irregularity in the first bin of the spectrum. The jet part of τ_2 is zero, if less than two particles are assigned to the jet directions. This happens quite often, as one can see in figure 30b, especially for vector boson fusion, whose jets are likely to be in the forward direction, i.e. not in the tracking region.

(a)

(b)
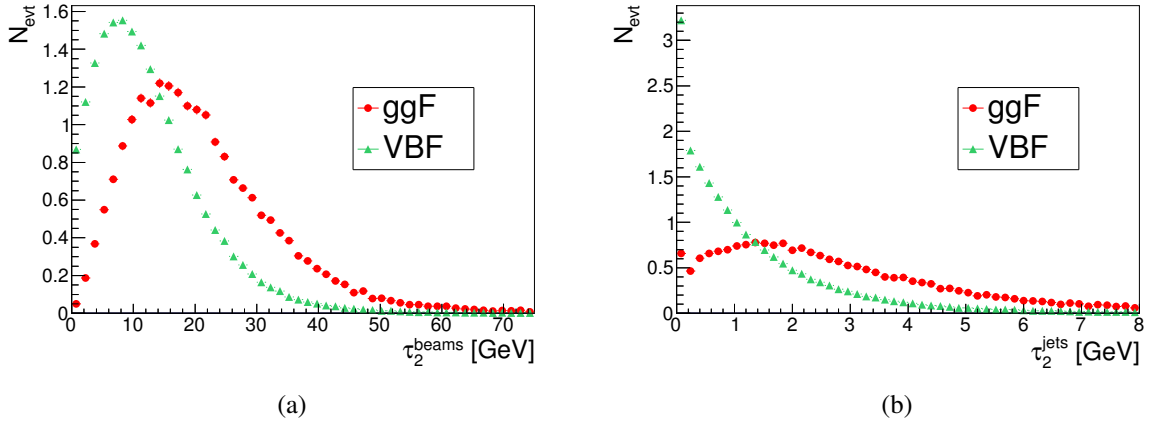
FIG. 30: Spectrum of the constituents of τ_2, i.e. τ_2^{beams} in (a) and τ_2^{jets} in (b), for gluon fusion and vector boson fusion at truth level, normalized to the integrated luminosity. Only charged particles within the Inner Detector acceptance with $p_T > 0.5\,\text{GeV}$ are considered.

3.7.2 Influence of the Jet Size Parameter ρ on the 2-Jettiness

The jet-size-controlling parameter ρ is chosen to be $\rho = 0.5$ for this analysis. However, it is interesting to see how variations of this parameter affect the τ_2 spectrum.

(a)   (b)
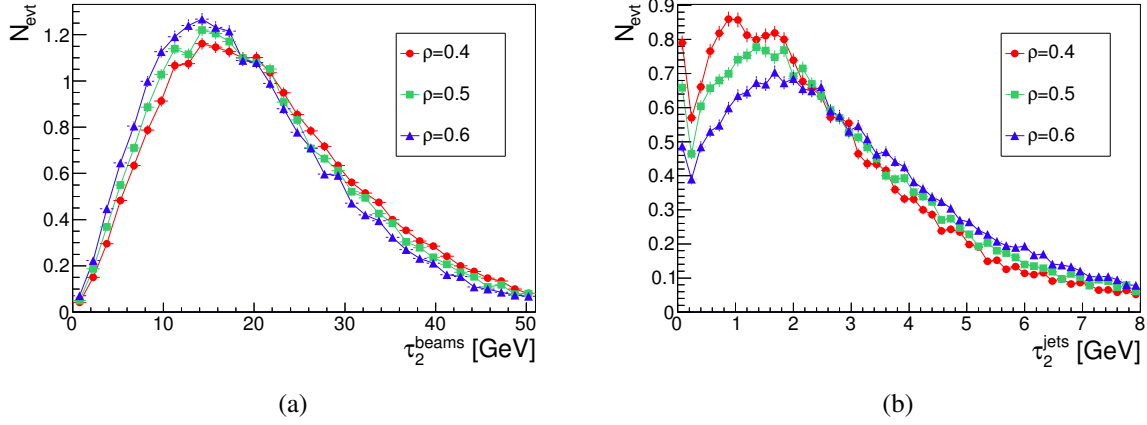
FIG. 31: Truth-level spectrum of (a) τ_2^{beams} and (b) τ_2^{jets} for ggF and for different values of jet area size ρ, normalized to the integrated luminosity. Only charged particles within the Inner Detector acceptance with $p_T > 0.5\,\text{GeV}$ are considered.

(a)   (b)
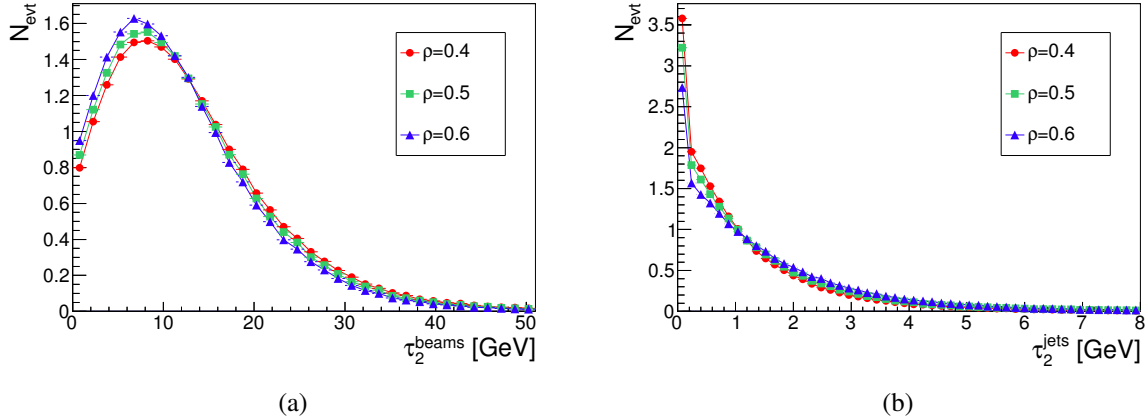
FIG. 32: Truth-level spectrum of (a) τ_2^{beams} and (b) τ_2^{jets} for VBF and for different values of jet area size ρ, normalized to the integrated luminosity. Only charged particles within the Inner Detector acceptance with $p_T > 0.5\,\text{GeV}$ are considered.

One expects that with increasing ρ the beam part of τ_2 will be decreased as the jet part will increase. In fact, this can be seen in figures 31 and 32. The spectrum is not very sensitive to small variations around small values for ρ, however, the effect for ggF events is quite noticeable. This might be due to the enhances amount of diffuse radiation in ggF events or to the larger width

of gluon jets. Since the parameter ρ corresponds to a size measure of the jet area, comparable to a simple radius, one can expect that the area of the jets will be roughly proportional to ρ^2. From this it can be inferred that the increase in τ_2^{jets} will be stronger when choosing values for ρ which are of order 1 or larger.

3.7.3 Influence of the Particle Mass on the 2-Jettiness

As the Inner Detector measures the particle's 3-momentum but gives in general no information about the particle type, it is not immediately clear which particle mass should enter the four-product between track and jet vectors in equation (55). For this reason, a compilation of the τ_2 spectrum for different track masses at truth level is shown in figures 33 and 34. As can be seen from these figures, there is barely any difference between the case of zero mass and the pion mass $m_\pi = 139.57\,\text{MeV}$ [7]. The charged pion is the lightest and most abundant hadronic particle to be measured in the Inner Detector and is used as default mass value of the computation of τ_2 at reconstruction level. At truth level the masses of the individual particles are available and are therefore used in the calculation of the four-products. The use of the pion mass as default mass hypothesis for particle masses leads to a small bias in τ_2. Since the pion is the lightest charged hadron it is not surprising that τ_2 is shifted to higher values when one uses the real particle masses for the computation.
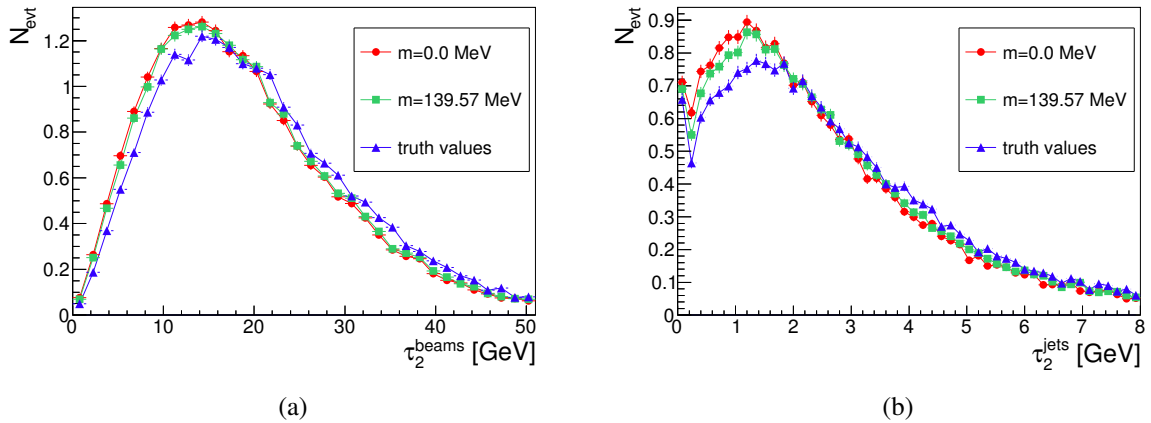

(a)   (b)

FIG. 33: Spectrum of (a) τ_2^{beams} and (b) τ_2^{jets} at truth level for ggF and for different particle mass values, normalized to integrated luminosity. Only charged particles within the Inner Detector acceptance and with $p_{\text{T}} > 0.5\,\text{GeV}$ are considered.

FIG. 34: Spectrum of (a) τ_2^{beams} and (b) τ_2^{jets} at truth level for VBF and for different particle mass values, normalized to integrated luminosity. Only charged particles within the Inner Detector acceptance and with $p_T > 0.5\,\text{GeV}$ are considered.
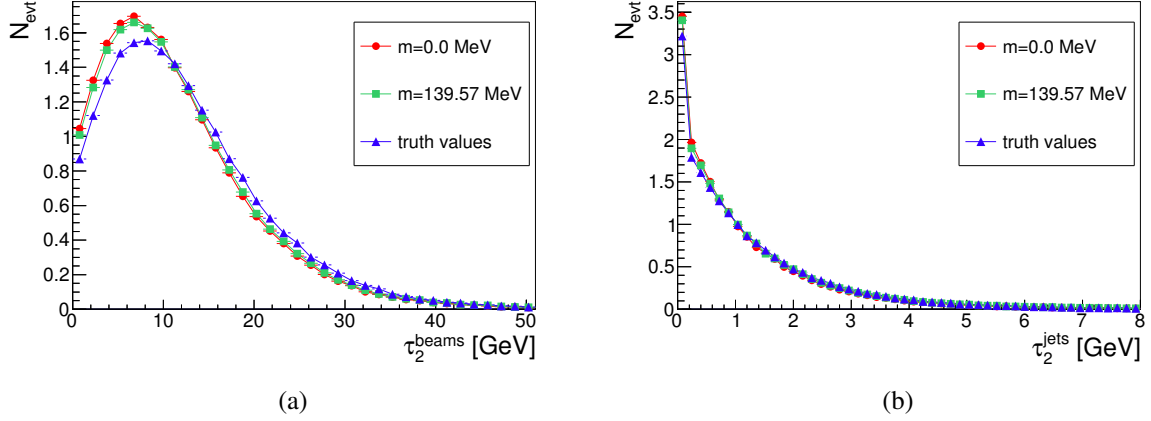
3.7.4 Impact of the Jet Axis Recomputation on the 2-Jettiness

The value of τ_2 depends on the chosen jet axis. As is explained in section 3.6.2, the original jet direction is used to assign all tracks from the Higgs vertex to one of the four jet- and beam regions. The jets' Lorentz vectors are taken from the jet reconstruction algorithm. After the process of assigning the tracks, new jet directions are computed on the basis of the momenta of the tracks which have been assigned to the jets. The difference in τ_2 which is induced by this iteration is shown in figure 35. The difference is small. Since the iteration of the jet axes is not changing the beam part of τ_2, only the spectrum of the jet part is shown. The spike in the first bin is less distinct when the jet axis is not recomputed, which is understandable: When the axis is not recomputed, the jet part of τ_2 is zero only if not a single particle is assigned to the jets. If, however, the jet direction is iterated, the jet part of τ_2 is zero if for both jets less than two particles are assigned to the jets.
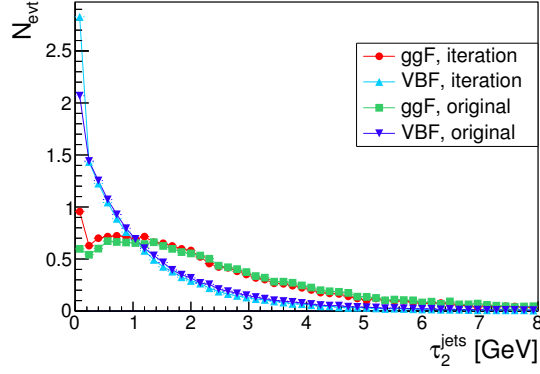
FIG. 35: The jet part of τ_2 at truth level for ggF and VBF events, using the original jet axis as well as using the iterated jet axis. Only charged particles within the Inner Detector acceptance and with $p_T > 0.5\,\text{GeV}$ are considered.

3.7.5 Influence of Multi-Parton Interactions on the 2-Jettiness

In pp collisions at the LHC, there are additional interactions between partons of the same proton pair in which the hard-interaction occurs. These additional interactions give rise to what is called the *underlying event*. The underlying event, which comprises all interactions of the proton pair except the hard-interaction must be modelled. *Multi-parton interactions* (MPI) are entering the Monte-Carlo simulations as a model for the underlying event. This introduces a model dependence; and since modelling is accompanied by a systematic uncertainty, the influence of the modelling of multi-parton interactions on the analysis result should be kept as small as possible.

In figure 36a, one can compare the normalized p_T spectrum of truth charged particles with and without MPI turned on in the Monte-Carlo simulation. The influence of MPI leads to an enhanced contribution of low-p_T particles. The p_T distribution is shown which is scaled by the inverse number of ggF and VBF events, respectively, so that the *y*-axis gives the mean number of particles per bin and event. The η spectrum, to be seen in figure 36b, essentially gets flattened out to some degree by the influence of MPI, which shows that the distribution in η of particles coming from MPI is rather flat. The influence on the τ_2 spectrum is shown in figures 37a and 37b. One can see that the difference between the spectra including and not including multi-parton interactions is considerable, especially in τ_2^{beams}. If not otherwise stated, the results shown in

78

this thesis always include multi-parton interactions. Therefore the results of this analysis will have uncertainties from the modelling of multi-parton interactions.
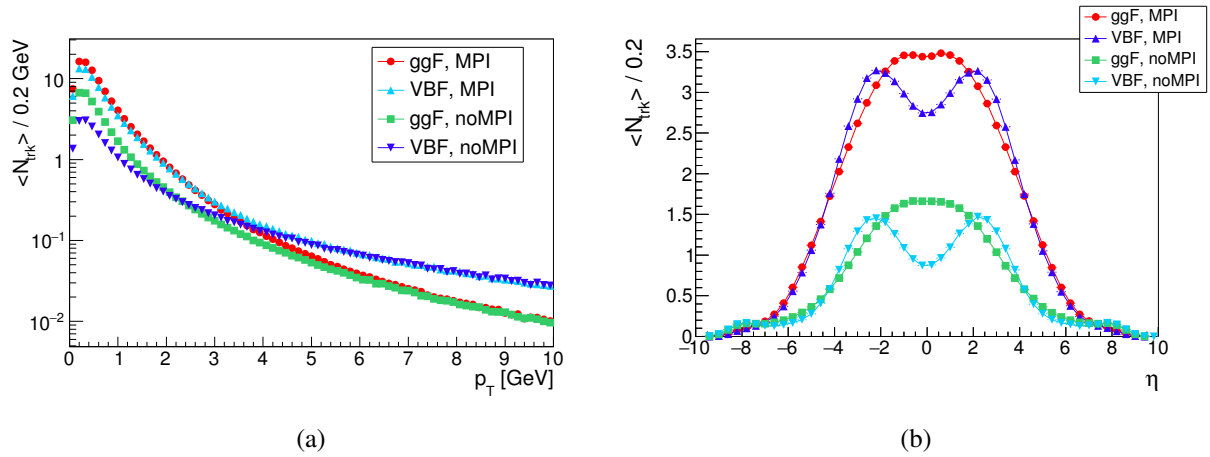

FIG. 36: Distribution of (a) particle transverse momentum and (b) track pseudorapidity at truth level for events including MPI and events not including MPI. The distribution is scaled by the inverse number of events in ggF and VBF, respectively. Only charged particles are considered. In (a), only particles within the Inner Detector acceptance are considered; in (b), only particles with a $p_T > 0.5$ GeV are considered.
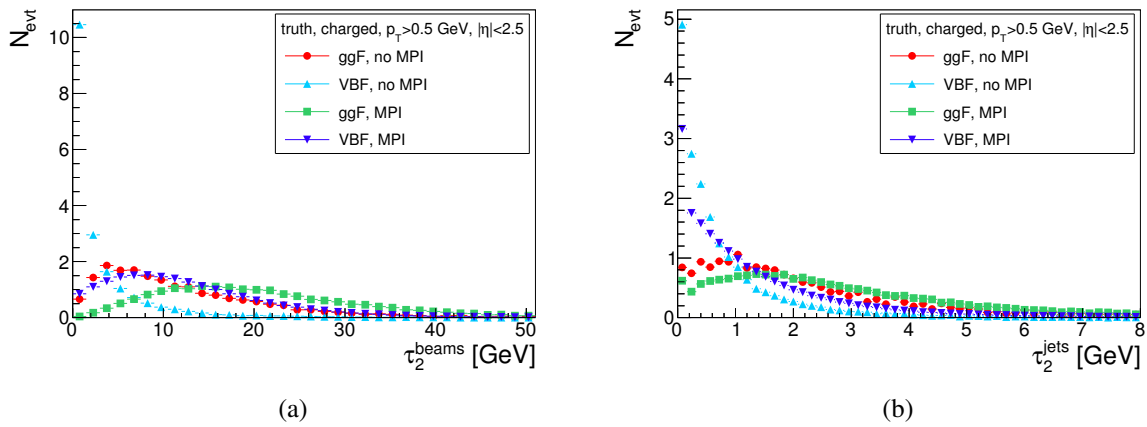
FIG. 37: Spectrum of (a) τ_2^{beams} and (b) τ_2^{jets} at truth level for events including MPI and events not including MPI, normalized to the integrated luminosity. A lower p_T cut of 0.5 GeV has been applied and only charged particles in the acceptance of the Inner Detector are considered.

It is desirable to keep the corrections between the spectra from perturbative calculations and the measured spectra as small as possible. Since multi-parton interactions are not part of the perturbative calculations, their effect on the spectrum and therefore on analysis results is sought to be minimized. Because the underlying event consists mainly of soft interactions, a reasonable

attempt to minimize the impact of MPI is to impose lower bounds on the p_T, such that soft particles are not considered in the computation of τ_2. The result of this can be seen in figures 38 and 39.
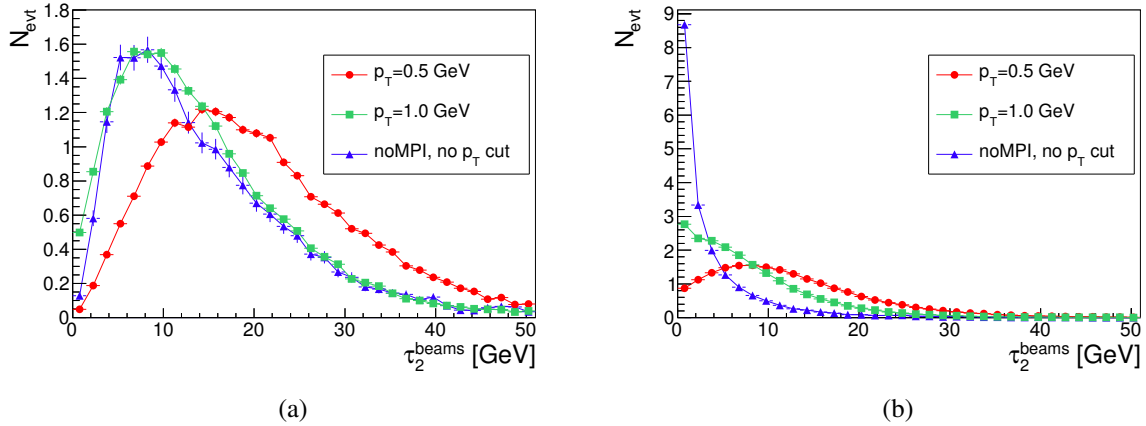

FIG. 38: The τ_2^{beams} spectra at truth level for (a) ggF and (b) VBF events imposing different lower cuts on the track transverse momentum. Only charged particles in the Inner-Detector acceptance are considered.
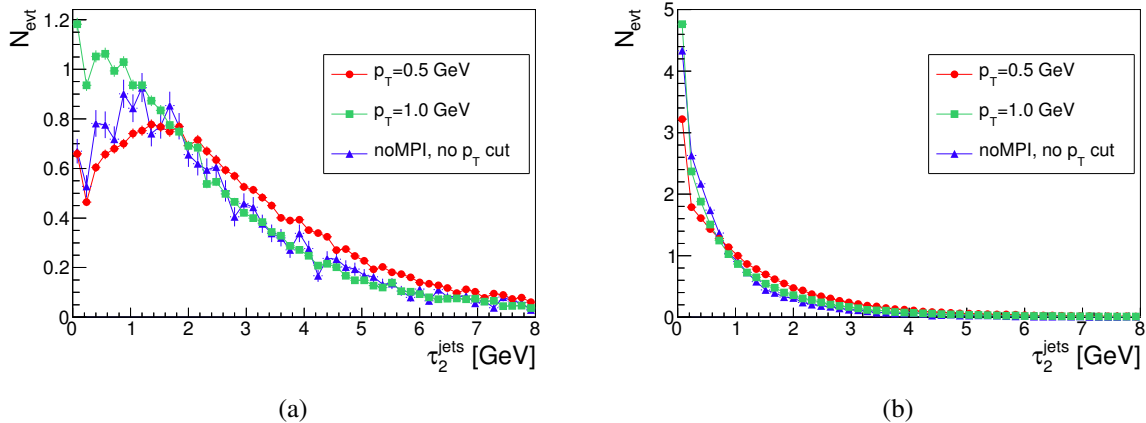

FIG. 39: The τ_2^{jets} spectra at truth level for (a) ggF and (b) VBF events imposing different lower cuts on the track transverse momentum. Only charged particles in the Inner-Detector acceptance are considered.

It can be concluded from these figures that it is possible to render the MPI and no-MPI spectra more similar, but especially for the beam part of VBF events no moderate cut on the particle transverse momentum can annihilate the MPI influence to a high degree. Moreover, higher cuts on the particle p_T have negative effects on the VBF purity, as is shown in section 3.9.1. The uncertainties which result from MPI would need to be estimated in order to make a statement

whether a higher p_T cut than $0.5\,\text{GeV}$ should be applied, given that the purity decreases and accordingly the theoretical uncertainty on the gluon fusion contribution would be enhanced when higher p_T cut is applied. The treatment of the uncertainties resulting from the modelling of MPI could not be done in the scope of this thesis; therefore the initial cut on p_T of $0.5\,\text{GeV}$ is not changed to larger values.

3.8 Resolution of the 2-Jettiness Measurement

In this section, the steps from the true τ_2 of an event to a definition that can be used for data are investigated. These steps are, starting with a fully inclusive truth definition, in which *all* particles are used, the following:

- All $\eta \to |\eta| < 2.5$ (due to limited Inner Detector acceptance)

- All $p_T \to p_T > 0.5\,\text{GeV}$ (lower limit on transverse momentum of tracks in this analysis)

- Neutral and charged particles $\to$ Only charged particles (only charged particles can be reliably assigned to their vertices; the inclusion of neutral particles would therefore lead to vulnerability to pile-up effects)

- Truth level $\to$ Reconstruction level (The event needs to be reconstructed; in general, there are differences between the true and reconstructed values of observables)

The effect which each of these steps has on the τ_2 spectrum will be shown both qualitatively in form of the τ_2 spectra and quantitatively in form of distributions of the form $\Delta(\text{lvl}\,1 - \text{lvl}\,2) = \tau_2^{\text{lvl}\,1} - \tau_2^{\text{lvl}\,2}$, where lvl 1 always corresponds to the less inclusive level. From these distributions Δ the contribution to the total resolution of each step will be measured. The resolution is measured by means of the standard deviation

$$\sigma = \sqrt{\frac{1}{N}\sum(\Delta_i - \bar{\Delta})^2}\,, \tag{57}$$

of the distribution of Δ. In the truth-level spectra of τ_2, the events need to fulfill the photon requirements detailed in section 3.3 in order to contribute. Not all of those events are also fulfilling the imposed restrictions at reconstruction level; these events are disregarded for the computation of the resolution distributions, so for this only a subset of the events used for the

spectra at truth level has been used. In order to compute the resolution distribution, only events with at least two jets at both truth- and reconstruction level are used. In data, one will also have a contribution of events which have at least two jets at reconstruction level, but less than two jets at truth level. The fraction of events in which this is the case is 0.32 %.

Starting from the fully inclusive truth spectrum of all particles without cut on the particle p_T and without cut on η, the smallest step towards reconstruction level is to apply the same η cut as at reconstruction level, i.e. $|\eta| < 2.5$. The comparison between these two levels is shown in figure 40. The corresponding distribution of the difference Δ is shown in figure 41. The distribution 41b features a very distinct peak at zero. This shows that the cut on η removes in most cases no particles assigned to the jet regions, especially for ggF events, where the jets tend to be central.
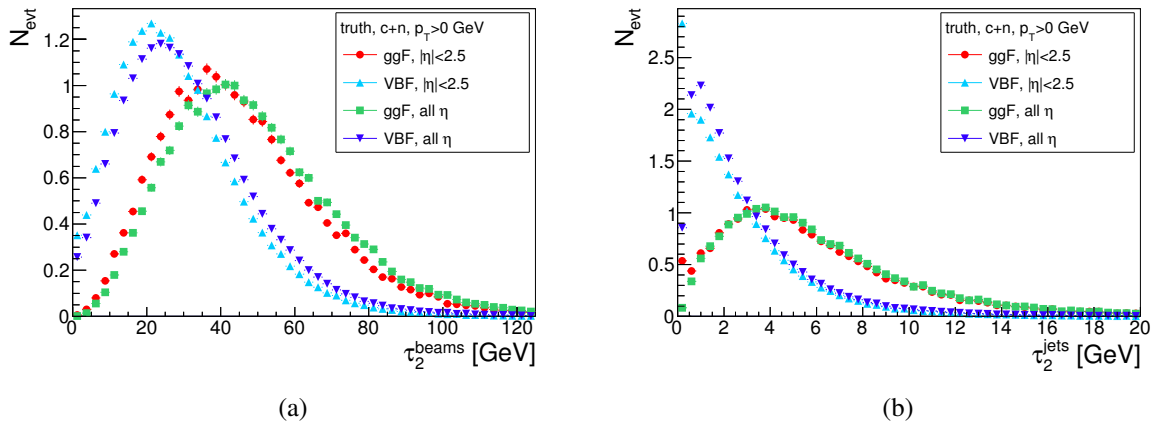

(a)

(b)

FIG. 40: Spectra of (a) τ_2^{beams} and (b) τ_2^{jets} for ggF and VBF events at different truth levels. In one case, *all* particles, in the other case only particles inside the Inner-Detector acceptance of $|\eta| < 2.5$ are considered: (truth, charged and neutrals, all p_T, all η) vs. (truth, charged and neutrals, all p_T, $|\eta| < 2.5$).
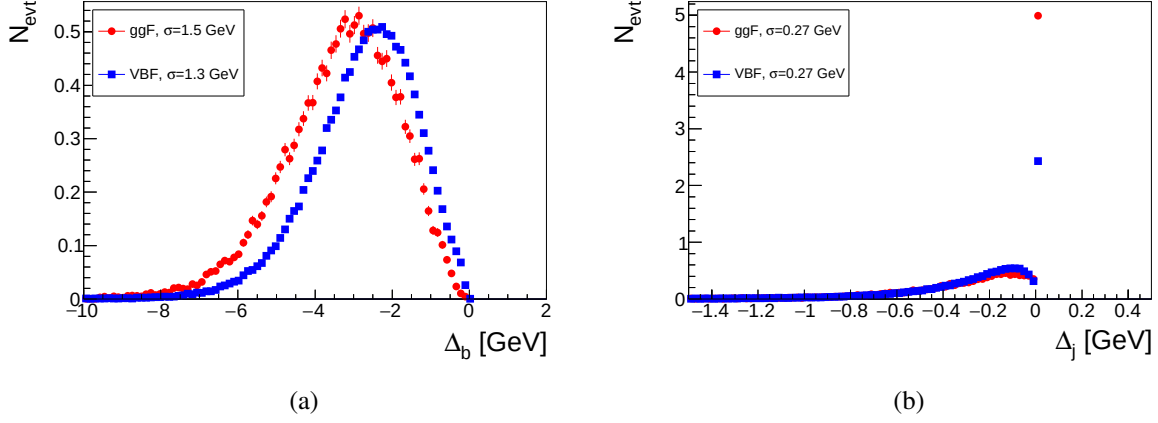
(a)   (b)

FIG. 41: Resolution contribution in (a) τ_2^{beams} and (b) τ_2^{jets} of the limited acceptance of the Inner Detector: (truth, charged and neutrals, all p_{T}, all η) vs. (truth, charged and neutrals, all p_{T}, $|\eta| < 2.5$).

Another contribution to the total difference between the inclusive truth spectrum and the reconstruction-level spectrum is the omission of low-p_{T} particles. The default value for this cut on the transverse momentum is $0.5\,\text{GeV}$ in this analysis. The corresponding comparison of the τ_2 spectra is shown in figure 42 and the corresponding distribution of Δ is shown in figure 43.
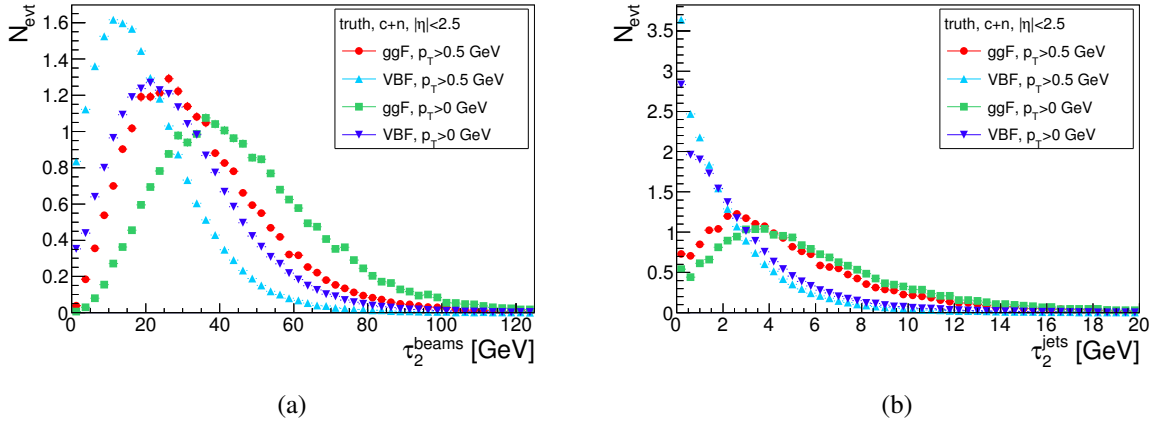

(a)   (b)

FIG. 42: Spectra of (a) τ_2^{beams} and (b) τ_2^{jets} for ggF and VBF events at different truth levels, considering only particles in the Inner-Detector acceptance. In one case, no restriction on the particle p_{T} is imposed, in the other case, a lower bound on the particle p_{T} of $0.5\,\text{GeV}$ is imposed: (truth, charged and neutrals, $|\eta| < 2.5$, $p_{\text{T}} > 0.5\,\text{GeV}$) vs. (truth, charged and neutrals, $|\eta| < 2.5$, no p_{T} cut).

(a)   (b)
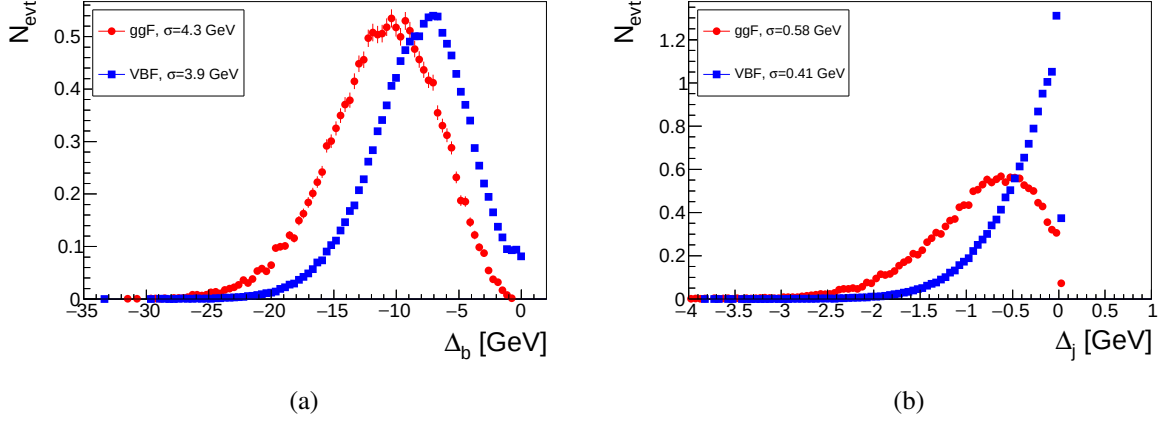
FIG. 43: Resolution contribution in (a) τ_2^{beams} and (b) τ_2^{jets} of the lower bound on the particle p_T of $0.5\,\text{GeV}$: (truth, charged and neutrals, $|\eta| < 2.5$, $p_T > 0.5\,\text{GeV}$) vs. (truth, charged and neutrals, $|\eta| < 2.5$, no p_T cut).

The next step is to measure how the exclusion of neutral particles from the measurement of τ_2 affects the distribution of τ_2. The results of this and the corresponding distribution of Δ can be seen in figures 44 and 45.
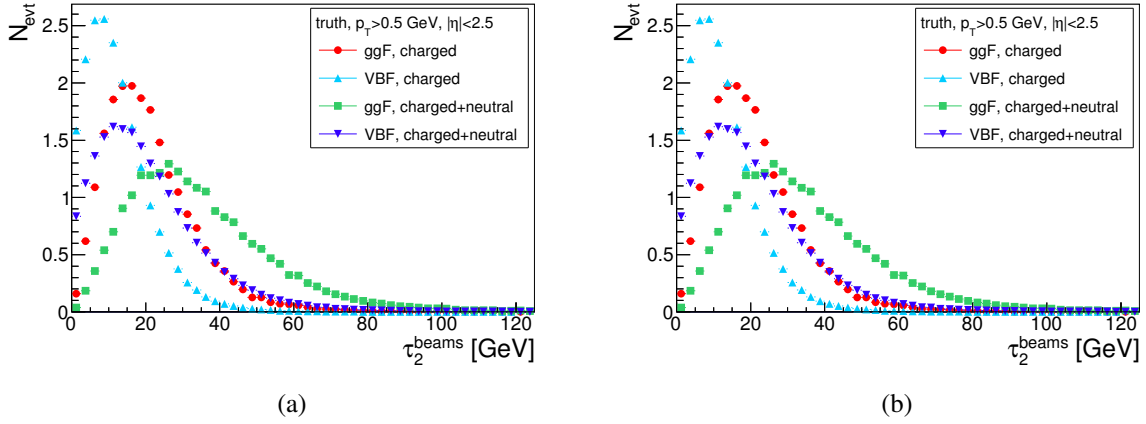

(a)   (b)

FIG. 44: Spectra of (a) τ_2^{beams} and (b) τ_2^{jets} for ggF and VBF events at different truth levels, considering only particles with $p_T > 0.5\,\text{GeV}$ within the Inner Detector acceptance. In one case, neutral and charged particles are considered, in the other case, only charged particles: (truth, charged, $|\eta| < 2.5$, $p_T > 0.5\,\text{GeV}$) vs. (truth, charged and neutrals, $|\eta| < 2.5$, $p_T > 0.5\,\text{GeV}$).
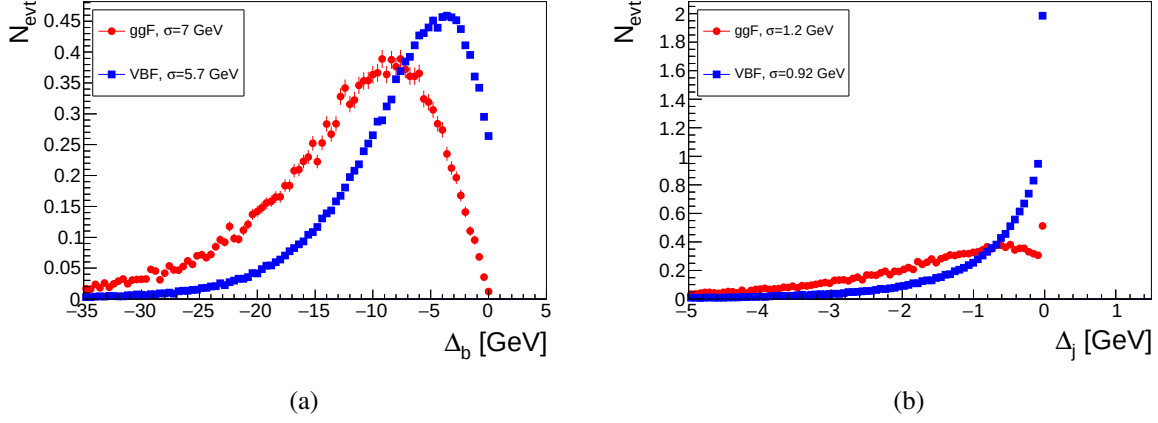
FIG. 45: Resolution contribution in (a) τ_2^{beams} and (b) τ_2^{jets} of the omission of neutral particles in τ_2^{beams}: (truth, charged, $|\eta| < 2.5$, $p_T > 0.5\,\text{GeV}$) vs. (truth, charged and neutrals, $|\eta| < 2.5$, $p_T > 0.5\,\text{GeV}$).

The next and last step is to measure the influence of the detector and reconstruction effects on τ_2. For a comparison of the corresponding spectra, see figure 46 and for the distribution of the corresponding Δ, see figure 47. The information from this distribution can be used to constrain the range of possible cut values for τ_2^{beams} and τ_2^{jets}. The cut values should not be smaller than the experimental resolutions, because this would lead to many misclassifications with respect to the question whether a given event has a τ_2 smaller or larger than the cut value.
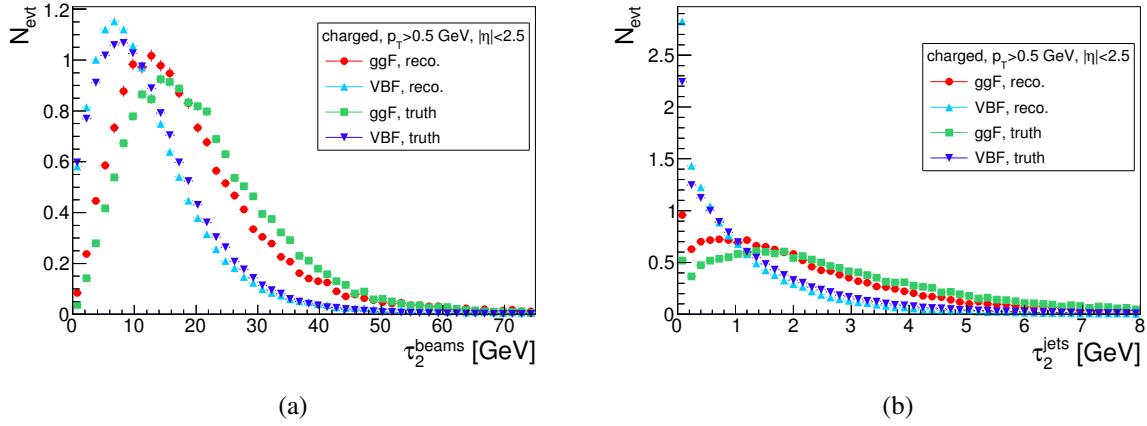

FIG. 46: Spectra of (a) τ_2^{beams} and (b) τ_2^{jets} for ggF and VBF events at reconstruction and truth level, considering only charged particles within the Inner Detector acceptance and with $p_T > 0.5\,\text{GeV}$.
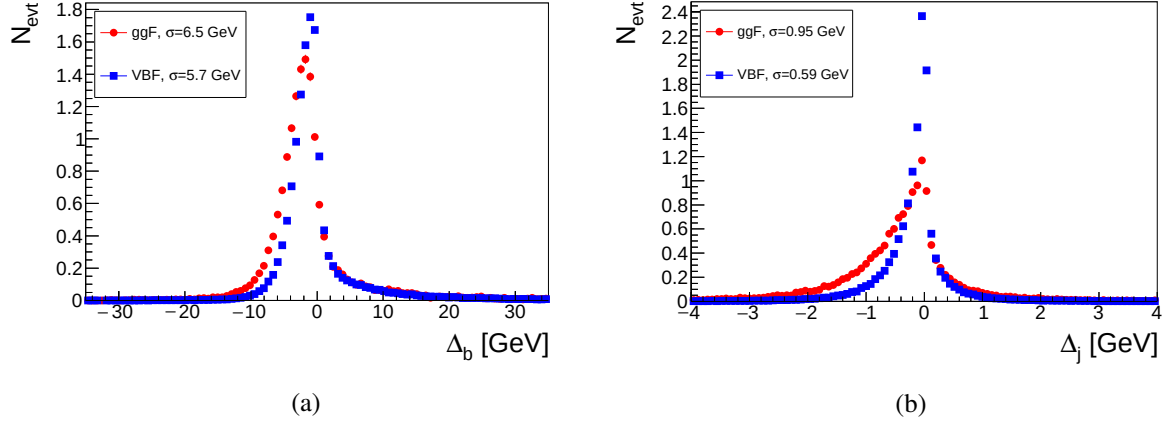
FIG. 47: Resolution contribution in (a) τ_2^{beams} and (b) τ_2^{jets} of detector- and reconstruction effects: (reconstructed, charged, $|\eta| < 2.5$, $p_T > 0.5\,\text{GeV}$) vs. (truth, charged, $|\eta| < 2.5$, $p_T > 0.5\,\text{GeV}$).

The exclusion of neutral particles and the difference between true and reconstructed quantities lead to the largest resolution contributions. The next-largest contribution results from the exclusion of low-p_T particles. The cut on the pseudorapidity gives the smallest contributions to the resolution. In figure 48, the τ_2 spectrum at reconstruction level and at the fully inclusive truth level is shown. The corresponding distribution of the event-by-event difference Δ can be seen in figure 49. The standard deviations of these resolution distributions are of order 15 GeV and 2 GeV for the beam part and jet part of τ_2, respectively. If one relates this number to typical numbers for τ_2^{beams} and τ_2^{jets}, it seems fortunate that one does not have to unfold these effects for the results of this analysis: The computation of the perturbative uncertainty, see section 3.10, is done using selections which are based on reconstruction-level information. Also, the measurement of the VBF signal strength uses simulation-based quantities which are at reconstruction level, so that unfolding is also not necessary in this case.
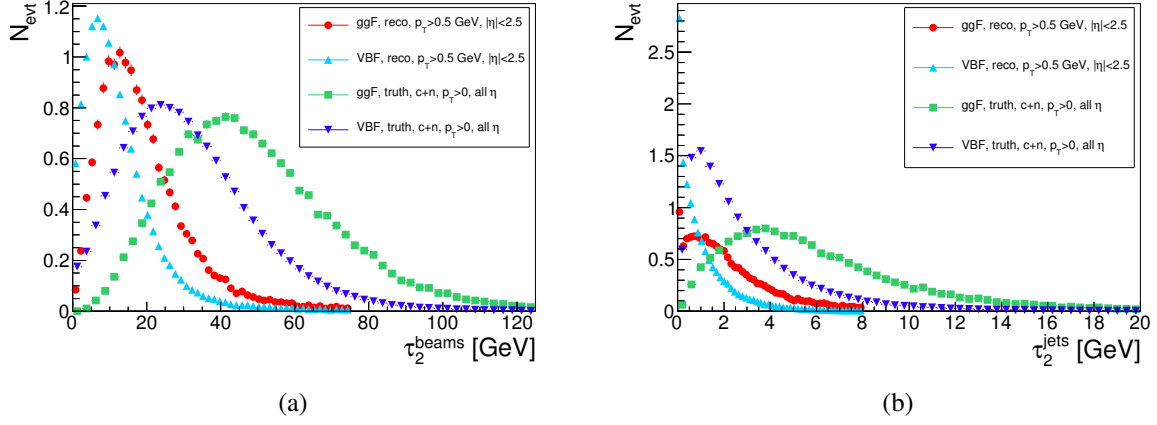
FIG. 48: Spectra of (a) τ_2^{beams} and (b) τ_2^{jets} for ggF and VBF events at reconstruction and truth level. At truth level, *all* particles are considered. At reconstruction level, tracks with $p_T > 0.5\,\text{GeV}$ with $|\eta < 2.5|$ are considered. The spectrum at reconstruction level is normalized to the integrated luminosity and the spectrum at truth level is in turn normalized to the number of reconstructed events.
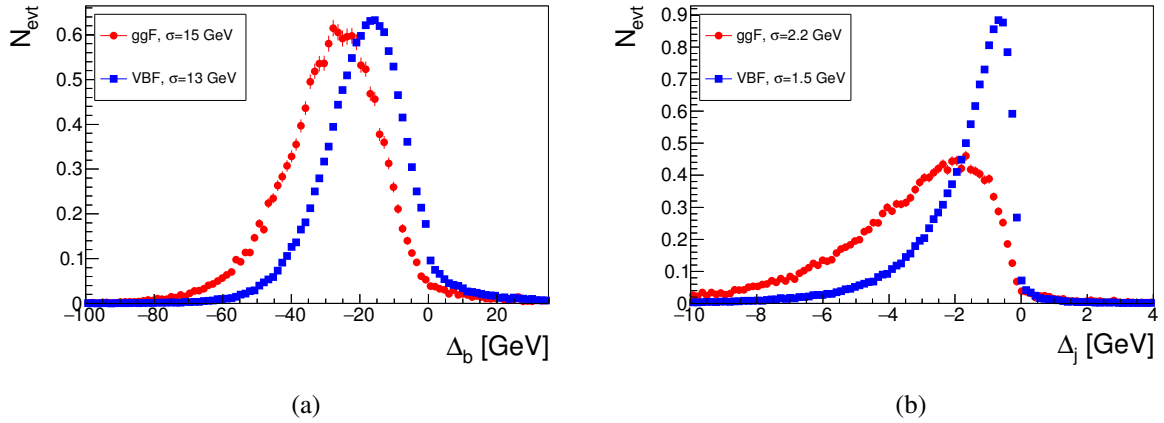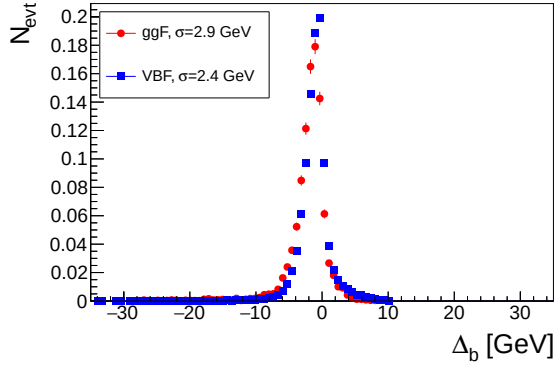

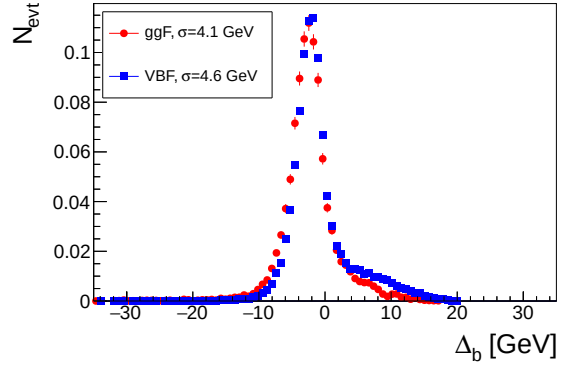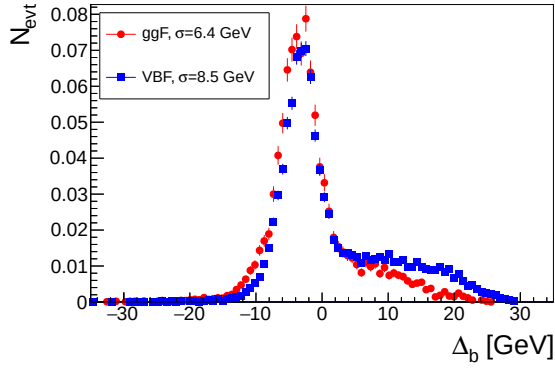FIG. 49: Total resolution in (a) τ_2^{beams} and (b) τ_2^{jets} between fully inclusive truth level and reconstruction level: (reconstructed, charged, $p_T > 0.5\,\text{GeV}$), $|\eta| < 2.5$) vs. (truth, charged and neutral, no p_T cut, all η).

(a) $0\,\mathrm{GeV} < \tau_2^{\mathrm{beams}}|_{\mathrm{reco}} < 10\,\mathrm{GeV}$

(b) $10\,\mathrm{GeV} < \tau_2^{\mathrm{beams}}|_{\mathrm{reco}} < 20\,\mathrm{GeV}$

(c) $20\,\mathrm{GeV} < \tau_2^{\mathrm{beams}}|_{\mathrm{reco}} < 30\,\mathrm{GeV}$
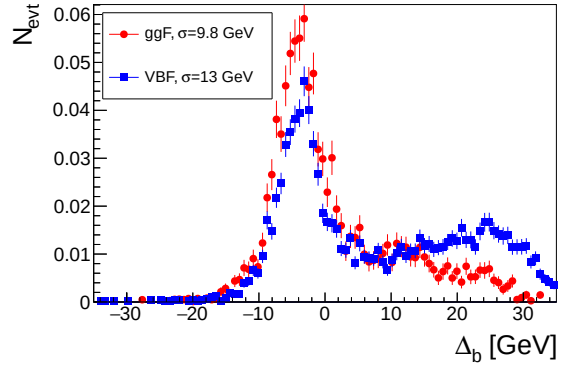
(d) $30\,\mathrm{GeV} < \tau_2^{\mathrm{beams}}|_{\mathrm{reco}} < 40\,\mathrm{GeV}$

FIG. 50: Resolution contribution from reconstruction and detector effects for different ranges of reconstructed τ_2^{beams}. Only charged particles with $p_{\mathrm{T}} > 0.5\,\mathrm{GeV}$ in the acceptance of the Inner Detector are considered.

(a) $0\,\mathrm{GeV} < \tau_2^{\mathrm{jets}}|_{\mathrm{reco}} < 0.8\,\mathrm{GeV}$ (b) $0.8\,\mathrm{GeV} < \tau_2^{\mathrm{jets}}|_{\mathrm{reco}} < 2.6\,\mathrm{GeV}$

(c) $1.6\,\mathrm{GeV} < \tau_2^{\mathrm{jets}}|_{\mathrm{reco}} < 2.4\,\mathrm{GeV}$ (d) $2.4\,\mathrm{GeV} < \tau_2^{\mathrm{jets}}|_{\mathrm{reco}} < 3.2\,\mathrm{GeV}$
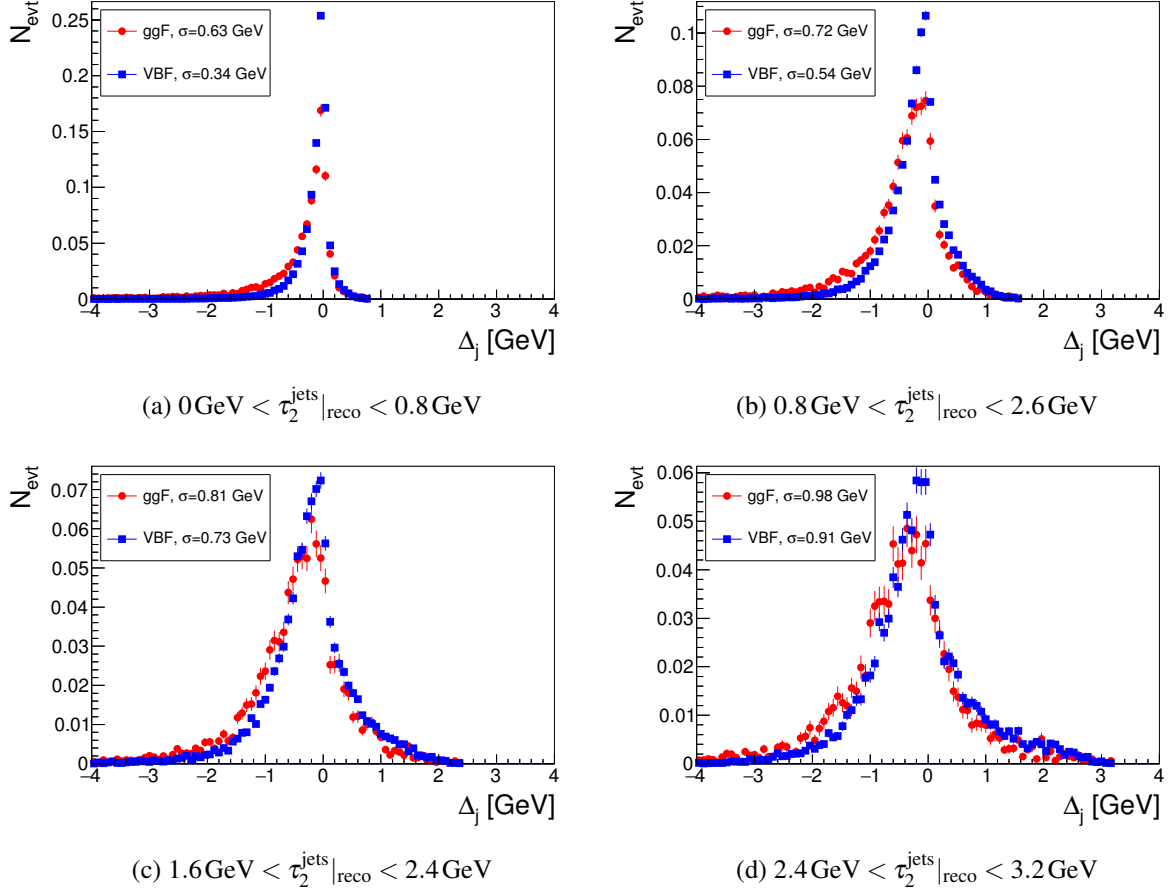
FIG. 51: Resolution contribution from reconstruction and detector effects for different ranges of reconstructed τ_2^{jets}. Only charged particles with $p_{\mathrm{T}} > 0.5\,\mathrm{GeV}$ in the acceptance of the Inner Detector are considered.

In the following, the resolution contribution from the event reconstruction will be further studied. The resolution of the τ_2^{beams}- and τ_2^{jets} measurement depends on the magnitude of the measured τ_2^{beams} and τ_2^{jets}, respectively. This is shown in detail in figures 50 and 51 for τ_2^{beams} and τ_2^{jets}, respectively. The resolution is smaller for events with smaller value of τ_2 (evaluated at reconstruction level).

As can be seen in figure 50, there is a considerably large extension of the distribution on the right side when considering large reconstruction-level values of τ_2^{beams}, which means that relatively many events in that range of τ_2^{beams} have a higher τ_2^{beams} than the event has on truth level. Especially for VBF events this feature is quite significant. From figure 52 one can conclude that this is an effect from the reconstruction of events: the reconstruction-level spectrum of τ_2^{beams} of the event sample with $\Delta > 5\,\mathrm{GeV}$ is significantly shifted to larger values, while the

truth-level spectrum of that event sample is rather similar to the control sample with $\Delta < 5\,\text{GeV}$. It may be suspected that pile-up is at least a contributor to this feature of the Δ distribution at large values of τ_2^{beams}. In order to test this hypothesis, the distribution in figure 50d, has been reproduced using four different event samples:

- Low pile-up & correct primary-vertex choice

- Low pile-up & incorrect primary-vertex choice

- High pile-up & correct primary-vertex choice

- High pile-up & incorrect primary vertex choice

Whether a primary vertex is here classified to be *correctly* selected, is determined by the condition that the reconstructed position of the primary vertex must be less than $0.3\,\text{mm}$ away from the true position. An event is assigned to the low pile-up sample, if the number of reconstructed primary vertices exceeds 16; events with less than 10 reconstructed primary vertices are assigned to the low-pile-up samples. The result is shown in figure 53. The incorrect selection of vertices gives a contribution to the second peak on the right side; however, it can not account for the whole extent of the second peak. There is no distinct difference in the distributions of the low-pile-up event samples and the high-pile-up event samples, which does not support the hypothesis that the unexpected large extension on the right side of the distribution is due to pile-up. It is possible that the large values of $\tau_2^{\text{beams}}|_{\text{reco.}}$ are due to the merging of pile-up vertices with the Higgs vertex. However, this hypothesis remains to be tested.
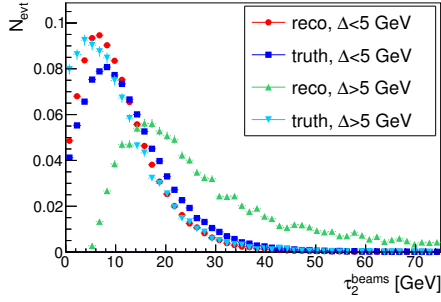
FIG. 52: Comparison of the τ_2^{beams} at reconstruction and truth level for VBF events. The spectra denoted with $\Delta > 5$ are are based on events from the region corresponding to the distribution's extension on the right side in50.
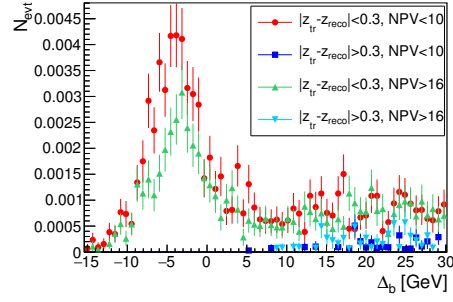

FIG. 53: Resolution distributions Δ for VBF events for reconstruction- and truth level at which only charged particles within the Inner Detector acceptance with $p_T > 0.5\,\text{GeV}$ are considered. Only events with $30\,\text{GeV} < \tau_2^{\text{beams}}|_{\text{reco.}} < 40\,\text{GeV}$ are considered.

3.9 Efficiency and Purity of the Vector Boson Fusion Selection

The VBF-efficiency ε_{VBF} and VBF-purity P_{VBF} of the signal selection, defined in section 3.5.2, are an important input for the decision on the cut menu. The efficiency and purity are calculated using Monte-Carlo simulations as given in equations (46) and (47). The efficiency is computed with respect to all simulated VBF events. As can be seen in the τ_2 spectrum in figure 54, one can enrich a selected sample with VBF events by excluding events with a τ_2, τ_2^{beams} and/or τ_2^{jets} value above some threshold. Both beam part and jet part of τ_2 tend to be smaller for VBF events than for gluon fusion events. Thus, by cutting at low values of τ_2 one can achieve a relatively high purity, since more gluon fusion events than vector boson fusion events will be removed by this cut. Of course some VBF efficiency will be lost, too. The efficiency and purity as a function of the cut value on τ_2 can be seen in figure 55. At large cut values the efficiency converges to the fraction of VBF events passing the photon cuts, see section 3.2, and jet requirements as described in section 3.3, while the purity converges to the purity resulting from these photon and jet cuts.
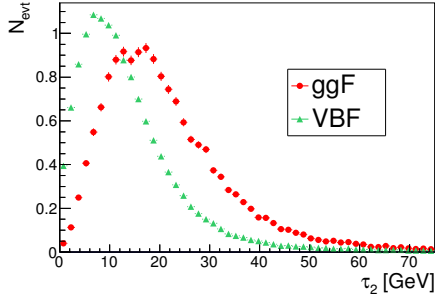
91

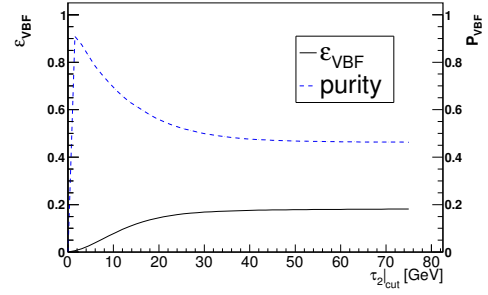FIG. 54: Spectrum of τ_2 at reconstruction level.

FIG. 55: VBF efficiency and purity as a function of the cut value on τ_2.

It is advantageous to not simply cut on the total 2-jettiness. This becomes clear when one looks at the two-dimensional distributions of the jet- and beam part of τ_2 in figure 56a and 56b. A plain cut on $\tau_2 = \tau_2^{\text{beams}} + \tau_2^{\text{jets}}$ would mean to select events below a straight line which is defined by $\tau_2^{\text{beams}} + \tau_2^{\text{jets}} = \tau_2|_{\text{cut}}$. But looking at the shape of the VBF distribution, it appears more efficient to employ a rectangular cut, which corresponds to separate cuts on τ_2^{beams} and τ_2^{jets}. The efficiency and purity which result from this rectangular cuts, is shown in figures 57a and 57b, respectively.

(a)

(b)
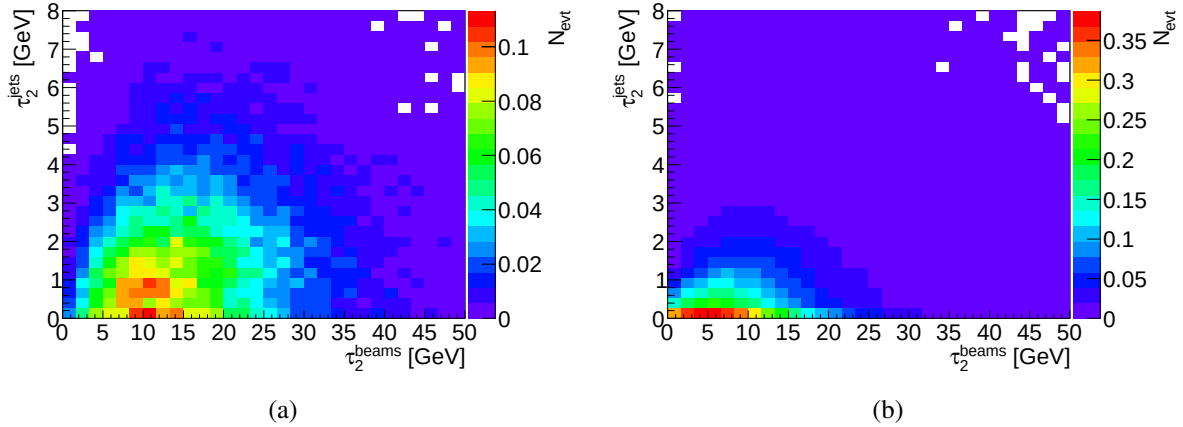
FIG. 56: Two-dimensional distribution of the beam- and the jet part of τ_2 for (a) gluon fusion and (b) vector boson fusion events at reconstruction level.

Using cuts on τ_2^{beams} and τ_2^{beams} to achieve a high purity of 80.5 %, as achieved in the *VBF tight* category of the official analysis, see section 3.5.2, would lead to very small efficiencies of about 3 %. Therefore, a selection using τ_2 in the simple way as it is done in this analysis

would rather result in a lower purity of 70 % at the same efficiency as for the *VBF tight* category (6.4 %).
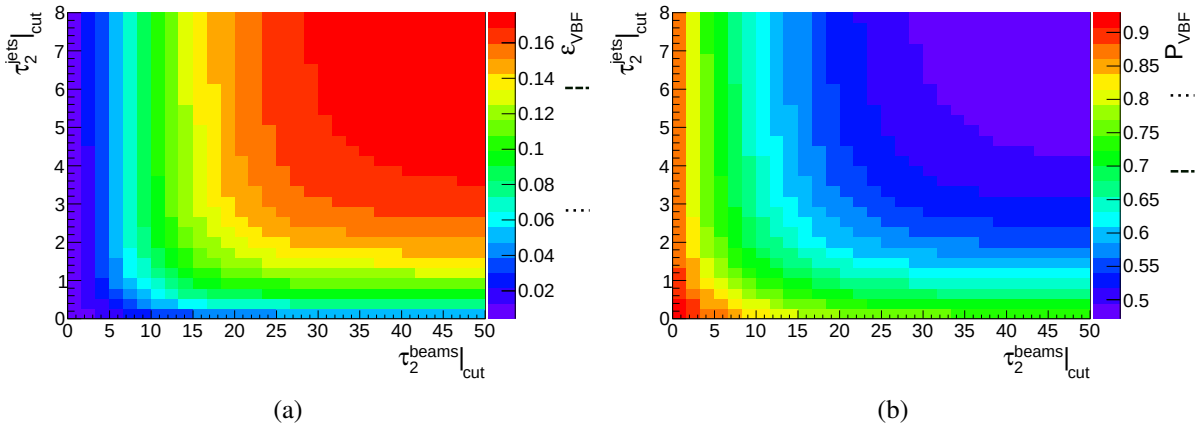
FIG. 57: VBF-efficiency (a) and VBF-purity (b) as function of cut values on τ_2^{beams} and τ_2^{jets}.

3.9.1 Impact of Cuts on the Track Transverse Momentum on the Efficiency and Purity

When considering the use of p_T cuts in rejecting particles coming from MPI, as it has been done in section 3.7.5, one should also consider the influence of these cuts on the efficiency and purity. This influence can be seen in figures 58 and 59.

FIG. 58: VBF efficiencies and purities for different lower cuts on the track transverse momentum as function of τ_2^{beams}. No cut on τ_2^{jets} is applied.
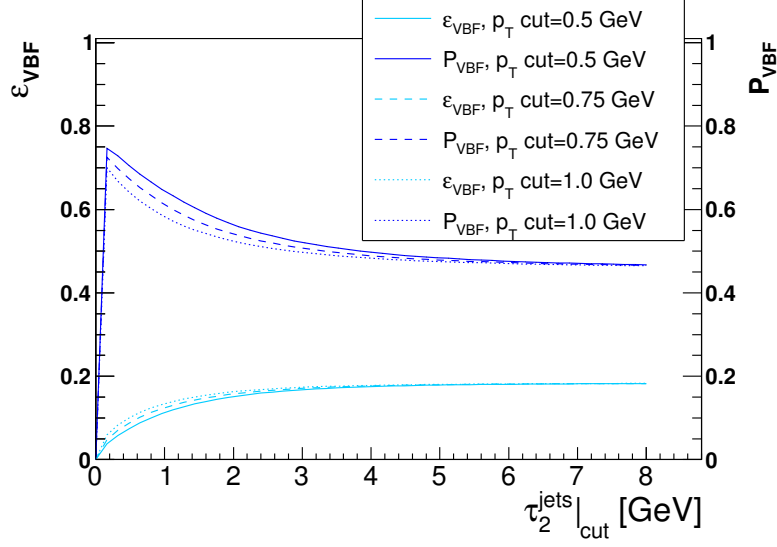
FIG. 59: VBF efficiencies and purities for different lower cuts on the track transverse momentum as function of τ_2^{jets}. No cut on τ_2^{beams} is applied.
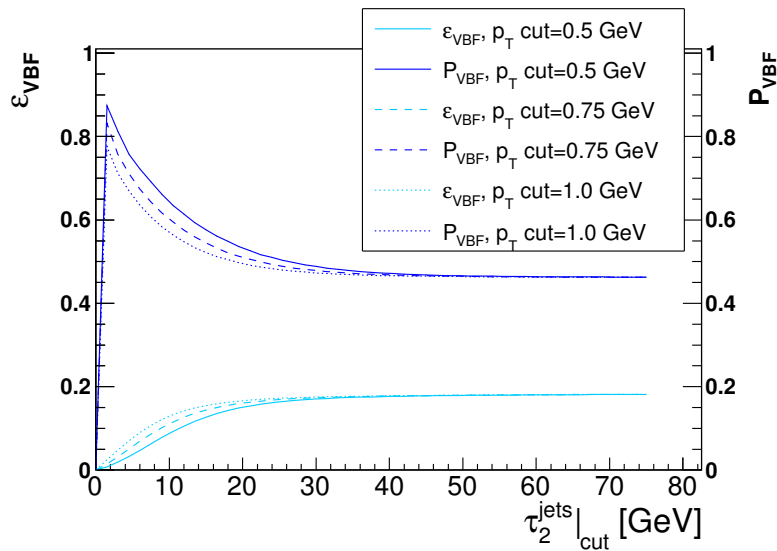
A higher cut on the track p_T decreases the purity. By increasing the p_T cut in a moderate range, as has been done here, mainly tracks in gluon fusion events are removed from the calculation of τ_2. This can be seen in figure 60, which gives the fraction of tracks with a p_T larger than the lower bound p_T^{cut}. From the observation that the number of ggF tracks decreases with a higher rate at increasing cut values one can draw the conclusion that also the 2-jettiness will decrease at higher rate for ggF events than for VBF events. But since gluon fusion events tend to be larger in terms of τ_2, gluon fusion and vector boson fusion events will look more similar in terms of τ_2 after a higher track p_T cut, which in turn leads to a decreased VBF purity.

FIG. 60: Fraction of tracks with a p_T larger than than $p_T|_{cut}$ at reconstruction level.

94

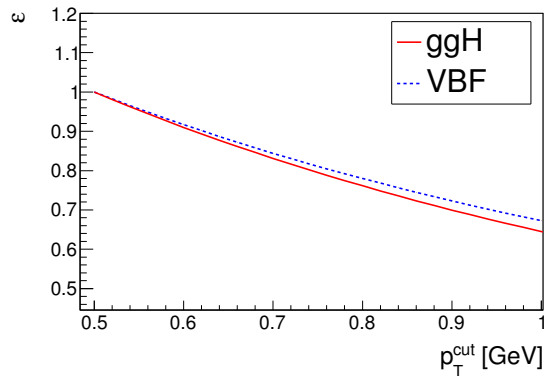## 3.10 Perturbative Uncertainty on the Gluon Fusion Contribution to Vector Boson Fusion Selections

The perturbative uncertainty on the predicted number of gluon fusion events contaminating the VBF-enriched event sample can be computed using a method which has already been used in the standard coupling analysis [2]. As mentioned in section 3.5, the standard analysis employs a Boosted Decision Tree to define its VBF-enriched categories. Due to the use of such a multivariate analysis, the selected phase space is quite complicated, such that an application of an extended version of the ST method as described in section 1 is necessary [4]. This extension consists in the definition of the ST procedure with more than two bins of a variable that quantifies the amount of additional radiation. Such a multi-bin-extension of the ST method is also used here; it is based on the variable $\Delta\phi_{H-jj}$ and uses 17 bins [55]. A corresponding correlation matrix has been created as outlined in section 1 [4].

The uncertainty is computed on the basis of the $\Delta\phi_{H-jj}$ spectrum (at truth level) after applying the selection cuts, using gluon-fusion Monte-Carlo simulations. In figure 5 on page 23 the gluon-fusion cross section and its ST uncertainty as a function of cuts on this variable was shown. Basically, the cuts in the chosen variable, e.g. the 2-jettiness, are matched to cuts on $\Delta\phi_{H-jj}$ and then the uncertainties which are computed for $\Delta\phi_{H-jj}$ are used to estimate the uncertainty of the chosen selection in the 2-jettiness. The selection can be applied using variables at reconstruction level. For each of the 17 bins of this spectrum, the perturbative uncertainty on the gluon-fusion cross section has been computed beforehand. The gluon-fusion cross section uncertainties in the $\Delta\phi_{H-jj}$ bins close to π are relatively large because a tight cut on additional radiation, as is applied when only selecting events with $\Delta\phi_{H-jj}$ close to π, introduces large Sudakov double logarithms. In the limit of a very tight selection, *any* additional emission with arbitrarily small p_T would be vetoed; approximating this limit, fixed-order perturbation theory becomes more and more unreliable and a logarithmic resummation is necessary [14].A basic idea of the method is: If the spectrum of $\Delta\phi_{H-jj}$ after applying the multivariate analysis or simple cuts on some event shape is strongly concentrated at values close to π, the perturbative uncertainty on the number of gluon fusion events that is selected by this selection will be large. The $\Delta\phi_{H-jj}$ spectrum after the application of a given selection, however complicated, can be used to evaluate the perturbative

cross section uncertainties via the following equation:

$$\frac{\Delta\sigma_{\text{ggF}}^{\text{sel.}}}{\sigma_{\text{ggF}}^{\text{sel.}}} = \sqrt{\sum_{i,j}^{n} \frac{\text{Cov}[i][j]}{\sigma[i]\,\sigma[j]} \cdot \frac{h[i]}{N} \cdot \frac{h[j]}{N}}. \tag{58}$$

Here, the number n denotes the number of bins in $\Delta\phi_{H-jj}$, $\text{Cov}[i][j]$ is the ij-component of the covariance matrix and $\sigma[i]$ denotes the calculated differential cross section in bin i; $h[i]$ is the number of gluon-fusion events having a $\Delta\phi_{H-jj}$ value (computed at truth level) which falls into bin i *after* the application of the selection. The total number of events which are selected is denoted with N.

The relative uncertainty for the 2-jet-inclusive selection, i.e. requiring at least two jets[43] at both reconstruction and truth level is computed to be 21.3 %. The corresponding distribution in $\pi - \Delta\phi_{H-jj}$ is shown in figure 61, together with $\pi - \Delta\phi_{H-jj}$ distribution for several selections based on cuts on τ_2, whose corresponding uncertainties can be obtained from tables 3, 4, or alternatively from figure 62. Among the shown distributions, the distribution which belongs to the tightest cut on the beam part of τ_2 has the highest fraction of events in the bin of $\Delta\phi_{H-jj}$ associated with the highest perturbative uncertainty, i.e. the bin of the distribution of $\pi - \Delta\phi_{H-jj}$ closest to zero.
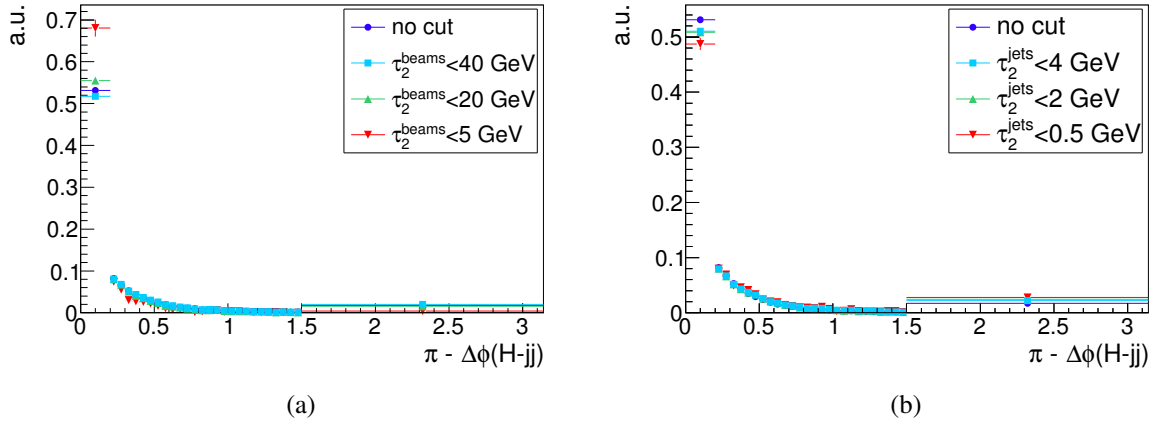
FIG. 61: The normalized $\pi - \Delta\phi_{H-jj}$ distributions for different cuts on (a) τ_2^{beams} and on (b) τ_2^{jets}. The selection denoted with *no cut* requires two jets at reconstruction and at truth level and imposes no restriction on $\Delta\eta_{jj}$.

The dependence of the perturbative uncertainty on the cut on τ_2^{beams} and on τ_2^{jets} can be seen

---

[43]This means also that no cut on $\Delta\eta_{jj}$ is applied.

$\tau_2^{\text{beams}}\|_{\text{cut}}$ [GeV]	no cut	40	30	20	10	5
$\Delta\sigma_2/\sigma_2$ [%]	21.4	20.8	21.1	22.5	26.4	33.9

TABLE 3: Perturbative uncertainties on the gluon fusion contribution to a VBF-enriched selection for different cuts on τ_2^{beams}.

$\tau_2^{\text{jets}}\|_{\text{cut}}$ [GeV]	no cut	6	4	2	1	0.5
$\Delta\sigma_2/\sigma_2$ [%]	21.4	20.6	20.7	20.6	20.5	20.4

TABLE 4: Perturbative uncertainties on the gluon fusion contribution to a VBF-enriched selection for different cuts on τ_2^{jets}.

in figures 62a and 62b, respectively. Cuts on the beam part of the 2-jettiness impose a veto on additional central jets and radiation. This veto results in enhanced selection of events with $\Delta\phi_{H-jj}$ close to π, which in turn leads to larger perturbative uncertainties. The value of the jet part of the 2-jettiness, on the other hand, is basically a measure for the jet size, not a sensible measure of additional central jet activity and therefore it is not surprising that the uncertainty does not depend significantly on this cut. However, one has to take into account that there may be other theoretical uncertainties arising from cuts on the jet part of the 2-jettiness that are not uncertainties resulting from central jet vetos. The study of these uncertainties was beyond the scope of this thesis[44]. In general, the values of the uncertainty for very tight cuts on the beam- or jet part of τ_2 are expected to be not entirely trustworthy, since there is some averaging due to the binning in $\Delta\phi_{H-jj}$, which may lead to an underestimation of the uncertainty for very tight cut values. In figure 63, the relative perturbative uncertainty on the gluon fusion contribution to the VBF-enriched sample is shown as a function of cuts on τ_2. The uncertainties range from 21 % to 40 %. In figure 64 the relative uncertainty with respect to the expected number of selected VBF events can be seen; this quantity is an important measure of the effect of the perturbative uncertainty on gluon-fusion cross section on the VBF signal strength uncertainty, see equation 52. At tightening cut values, the influence of the uncertainty on the gluon fusion contamination is decreasing. The relative uncertainty on the gluon fusion cross section in the VBF-enriched selection is increasing, but the higher purity in VBF at tight cut values overcompensates this

---

[44]Such a study could be performed by comparing samples that have been produced using different jet shower models, e.g. that of PYTHIA and that of HERWIG [56].

increase. Therefore the contribution of the theoretical uncertainty on the total uncertainty on the VBF signal strength can be minimized by cutting tightly. In general, one would also like to compute the theoretical uncertainty as a function of τ_2 cuts directly, i.e. to not only use an indirect method as it is presented here. However, this is difficult, especially because only tracks (and not the inclusive set of all produced particles) are used in the computation at reconstruction level.

(a)

(b)
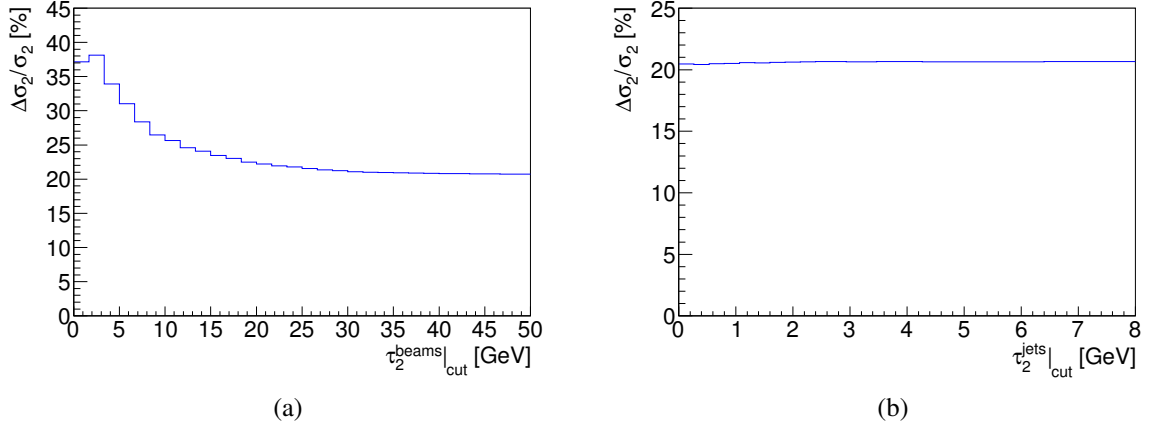
FIG. 62: Relative perturbative uncertainty on the gluon fusion contribution to the VBF selection as a function of cuts on τ_2^{beams} (no cut on τ_2^{jets}) (a) and as of cuts on τ_2^{jets} (no cut on τ_2^{beams}).
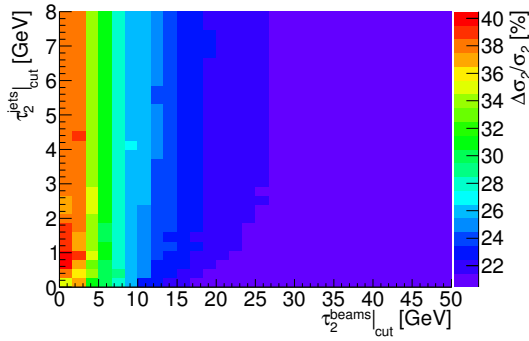
FIG. 63: Relative perturbative uncertainty on the ggF contribution as a function of cut values for τ_2^{beams} and τ_2^{jets}.
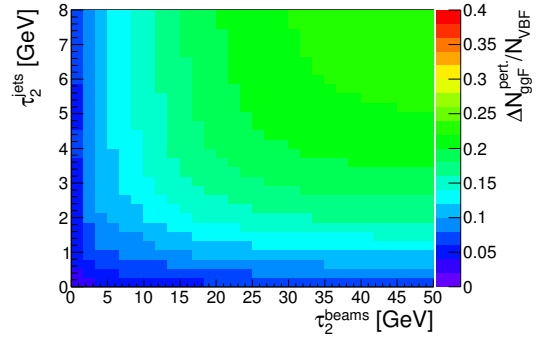
FIG. 64: Ratio of perturbative uncertainty on the gluon fusion contamination and the number of selected VBF events as a function of cut values for τ_2^{beams} and τ_2^{jets}.

3.11 Vector Boson Fusion Signal Strength and Final Selection

In this section, the vector boson fusion signal strength and its uncertainty will be computed as outlined in subsection 3.5, using a τ_2-based VBF-enriched selection. For this procedure, data

events will be used which have been selected as described in sections 3.2.1 and 3.3. In order to compute the VBF signal strength and its uncertainty, the background shape and expected signal shape need to be parametrized. Using this parametrizations, the expected uncertainty on the VBF signal strength will be determined as a function of cuts on τ_2. Based on this uncertainty distribution, suitable cut combinations with minimal uncertainty on μ_{VBF} can be chosen. For these cut combinations, the VBF signal strength will be computed. This computation is done in three steps: The invariant diphoton mass spectrum of data events is fitted, and from this one can obtain the fitted number of Higgs events. Subsequently, the expected number of non-VBF Higgs events from the fitted number of Higgs events is subtracted. By comparing the resulting number with the expected number of VBF events, determined by Monte-Carlo simulation, one obtains the VBF signal strength.

3.11.1 The Shape of the Higgs Peak

Before the invariant diphoton mass spectrum is fitted, see figure 65 for an example, the shape of the signal as well as the shape of the background distribution must be determined. In this section, the determination of the former will be presented.

The Higgs peak in the invariant diphoton mass spectrum is in ATLAS analyses commonly described by the sum of a *Crystal-Ball* function and a Gaussian function. For an example of the mass spectrum of simulated $H \rightarrow \gamma\gamma$ events and the corresponding fit of the Higgs peak, see figure 66. The Crystal-Ball function covers most of the events in the central peak, while the relatively wide Gaussian collects the outliers. The Crystal-Ball function is defined as [57]

$$y_{\text{CB}}(x) = N_{\text{S}} \cdot f_{\text{CB}} \cdot A \cdot \left\{ \begin{array}{ll} \exp(-\frac{(x-\bar{x})^2}{2\sigma^2}) & \text{if } \frac{x-\bar{x}}{\sigma} \geq -\alpha \\ \left(\frac{n}{|\alpha|}\right)^n \exp(-\frac{|\alpha^2|}{2}) \cdot (\frac{n}{|\alpha|} - |\alpha| - \frac{x-\bar{x}}{\sigma})^{-n} & \text{if } \frac{x-\bar{x}}{\sigma} \geq -\alpha \end{array} \right\}, \quad (59)$$

where x is the variable of the spectrum, in this case $m_{\gamma\gamma}$; the number of signal events, in this case Higgs events, is denoted by N_{S}. The fraction of signal events contained in the Crystal-Ball function is denoted with f_{CB}, and A is a normalization factor given by

$$A^{-1} = \sigma \cdot \left(\frac{n}{|\alpha|} \cdot \frac{1}{n-1} \cdot \exp(-\frac{-|\alpha|^2}{2} + \sqrt{\frac{\pi}{2}} \cdot (1 + \text{erf}(\frac{|\alpha|}{2}))) \right) . \quad (60)$$

The Gaussian function is defined as

$$y_G = (1 - f_{CB}) \cdot N_S \cdot \frac{1}{\sigma_G \sqrt{2\pi}} \exp\left(-\frac{(x - \bar{x}_G)^2}{2\sigma_G^2}\right). \tag{61}$$

Here, $\bar{x}_G$ denotes the mean value of the Gaussian distribution and σ_G^2 its width. The mean value of the Crystal-Ball function $\bar{x}$ and the mean value of the Gaussian $\bar{x}_G$ are not required to be identical. The parameters of the Crystal-Ball function and the Gaussian have been taken from fits to $m_{\gamma\gamma}$ spectra from Monte-Carlo simulations, using events from all five Higgs production modes. Each mode enters the spectrum with a relative weight corresponding to the expected number of selected events from each production mode. The mass of the Higgs boson in the simulation is taken to be 125.0 GeV. Since the Higgs mass is measured to be 0.36 GeV larger than that [11], $\bar{x}$ and $\bar{x}_G$ are shifted accordingly. The signal shape has been determined as a function of cuts on τ_2^{beams} and τ_2^{jets}. In spite of efforts to achieve parametrizations that fit the spectra perfectly, the fits of the most mass spectra underestimate the peak to a small degree, see figure 66 for an example.
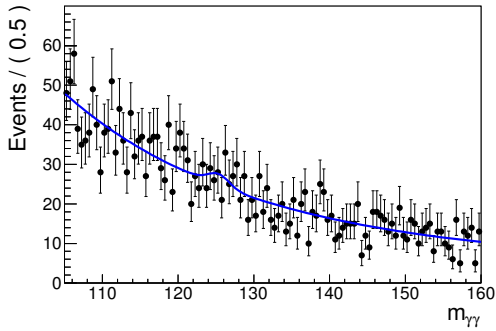
FIG. 65: Fitted invariant diphoton mass spectra and fits for data events with $|\Delta\eta_{jj}| > 2.0$.
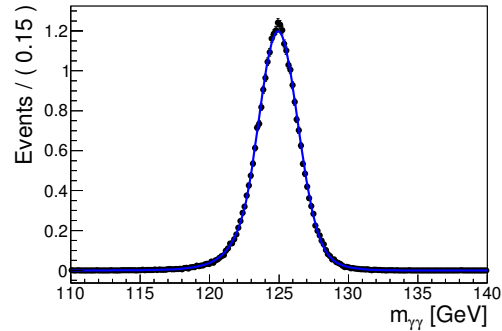
FIG. 66: Fitted invariant diphoton mass spectrum of Higgs events from Monte-Carlo simulations, using events with $|\Delta\eta_{jj}| > 2.0$.

3.11.2 The Purity in Higgs and the Expected Statistical Uncertainty on the Higgs Event Yield

Most events from the data event sample are non-Higgs events. These constitute the background of the Higgs signal. In the following, it will be discussed to what degree the VBF-enriched selection based on τ_2 is able to reject this background. This can be measured in terms of the

purity in Higgs. The amount of background in the Higgs signal region is an important input for the uncertainty on the VBF signal strength: the more background events are in the signal region, the larger the statistical uncertainty on the fitted number of Higgs events at a given value of signal events. The expected purity in Higgs, here denoted by P_{90}, will be determined as a function of cuts on τ_2 and is is defined as

$$P_{90} = \frac{N_{H,90}^{\mathrm{MC}}}{N_{H,90}^{\mathrm{MC}} + B_{90}}, \tag{62}$$

where the expected number of background events in the smallest mass region which contains 90 % of the expected signal events is denoted by B_{90}; correspondingly S_{90}^{MC} denotes 90 % of the expected Higgs event yield. In order to determine the expected purity in Higgs, one first needs a parametrization of the invariant diphoton mass spectrum, which contains both background events and signal events. The shape is chosen to be a sum of the signal shape which has been determined in section 3.11.1 and an exponential function of a second-order polynomial. Both are common choices for signal and background, respectively, in $H \rightarrow \gamma\gamma$ analyses [2]. The background is thus parametrized as:

$$y_{\mathrm{bkg}}(m_{\gamma\gamma}) = N_{\mathrm{bkg}} \cdot B \cdot e^{a m_{\gamma\gamma} + b m_{\gamma\gamma}^2}, \tag{63}$$

where N_{bkg} is a normalization factor, a and b are free parameters of the background model, and B is a normalization constant which can be computed as follows:

$$B^{-1} = -\frac{1}{2\sqrt{b}} \cdot \left[\sqrt{\pi} \cdot \exp\left(-\frac{a^2}{4b}\right) \cdot \left(\mathrm{erfi}\left(\frac{2 b m_{\gamma\gamma}^{\mathrm{max}} + a}{2\sqrt{b}} \right) - \mathrm{erfi}\left(\frac{2 b m_{\gamma\gamma}^{\mathrm{min}} + a}{2\sqrt{b}} \right) \right) \right]. \tag{64}$$

Here, $m_{\gamma\gamma}^{\mathrm{min}}$ and $m_{\gamma\gamma}^{\mathrm{max}}$ specify the bounds of integration[45]. The lower limit is chosen to be 105 GeV, while the upper integration limit is 160 GeV. The function denoted with *erfi(x)* is the imaginary error function.

The free parameters, which are obtained by fitting the invariant diphoton mass spectrum with the sum of signal and background distribution function, are the number of Higgs events, the number of background events and the two parameters describing the distribution function

---

[45]Other than the integral of the Crystal-Ball or Gaussian function, the integral of these background parametrization would not be converging if the integration range would not be fixed to a finite range. Correspondingly, the number of background events N_{bkg} is the number of background events *inside* of the specified range.

of the background. Four mass spectra based on different τ_2-based VBF selections and the corresponding fits are shown in figure 67.

(a) $\tau_2^{\text{beams}}|_{\text{cut}} = 40\,\text{GeV}$, $\tau_2^{\text{jets}}|_{\text{cut}} = 6.4\,\text{GeV}$

(b) $\tau_2^{\text{beams}}|_{\text{cut}} = 25\,\text{GeV}$, $\tau_2^{\text{jets}}|_{\text{cut}} = 6.4\,\text{GeV}$

(c) $\tau_2^{\text{beams}}|_{\text{cut}} = 40\,\text{GeV}$, $\tau_2^{\text{jets}}|_{\text{cut}} = 3.2\,\text{GeV}$

(d) $\tau_2^{\text{beams}}|_{\text{cut}} = 25\,\text{GeV}$, $\tau_2^{\text{jets}}|_{\text{cut}} = 3.2\,\text{GeV}$
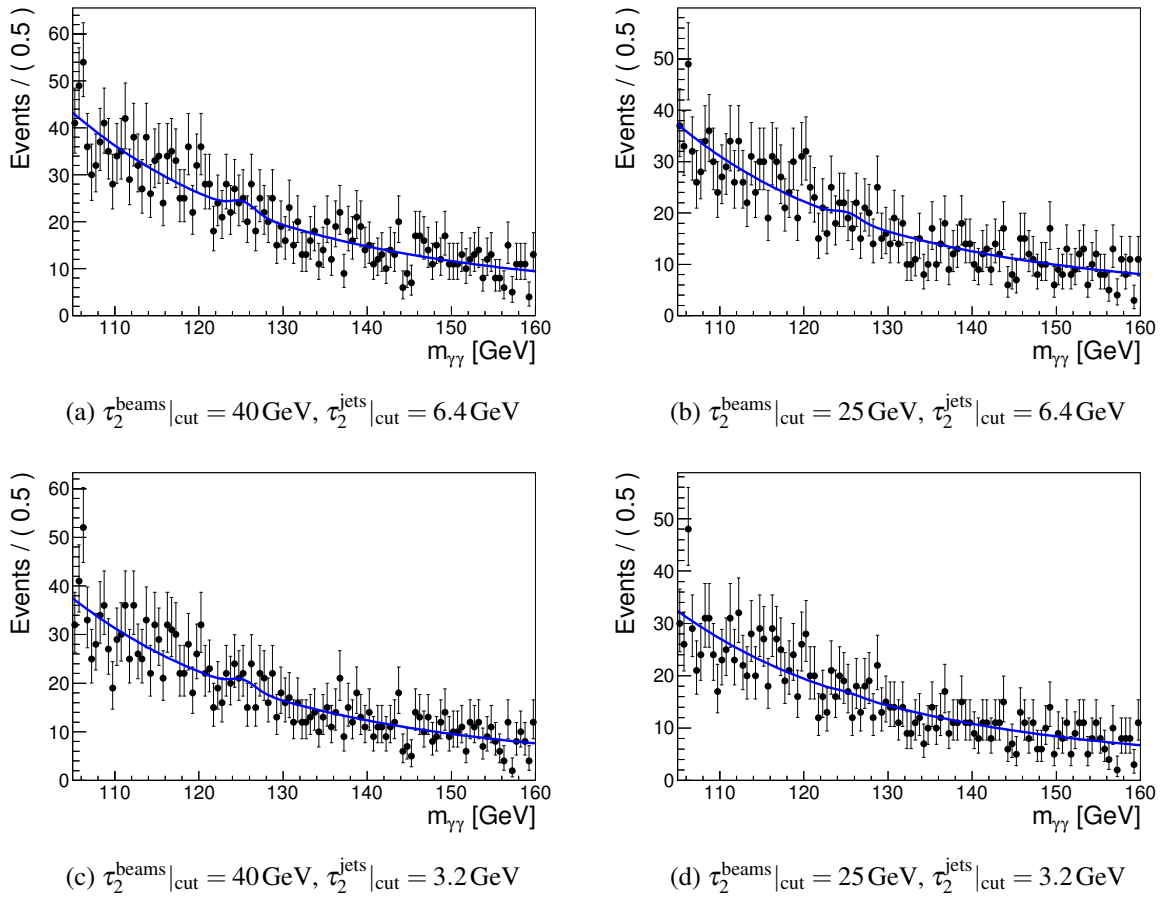
FIG. 67: Invariant diphoton mass spectra and fits for different cuts on τ_2.

From these fits, the background shape is determined as a function of cuts on τ_2. For several VBF-enriched categories, the corresponding values of the number of background events in the signal region and the expected number of signal events are listed in table 5. The expected purity is shown in figure 68 as a function of the cuts on τ_2^{beams} and τ_2^{jets}. The dependence on the cut values is small. Very tight cut values lead to very limited statistics such that the results in those bins suffer from large statistical uncertainties. The small dependence of the purity in Higgs on the cut values implies that the cuts on τ_2 remove Higgs events and background events at a similar rate. This is also expected from the spectrum of τ_2 of these data events, which is shown in figure 69 and is quite similar to the spectrum of Higgs events. In figure 70 one can explicitly see that
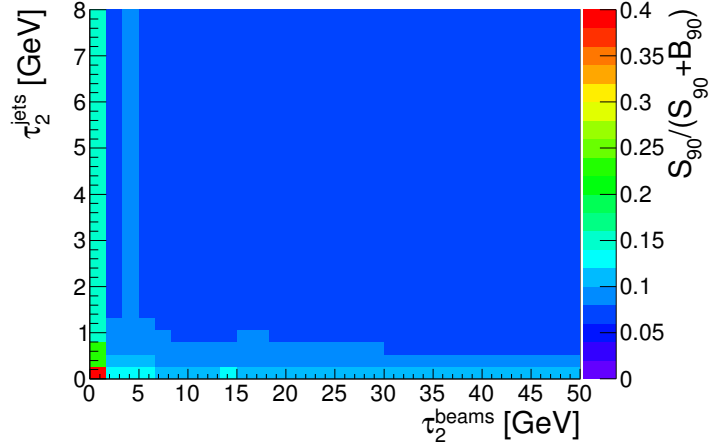
FIG. 68: Expected purity in Higgs as a function of cut values on τ_2^{beams} and τ_2^{jets}.

Selection	B_{90}	$N_{H,,90}^{\text{MC}}$	$P_{90}[\%]$	σ_{90} [GeV]
no cut on τ_2	274 ± 6	20.98 ± 0.07	7.0 ± 1.1	2.78
$\tau_2^{\text{beams}} < 40\,\text{GeV},\ \tau_2^{\text{jets}} < 6.4\,\text{GeV}$	244 ± 5	18.77 ± 0.06	7.1 ± 1.3	2.78
$\tau_2^{\text{beams}} < 25\,\text{GeV},\ \tau_2^{\text{jets}} < 6.4\,\text{GeV}$	205 ± 5	16.30 ± 0.06	7.4 ± 1.3	2.78
$\tau_2^{\text{beams}} < 40\,\text{GeV},\ \tau_2^{\text{jets}} < 3.2\,\text{GeV}$	208 ± 5	16.25 ± 0.06	7.2 ± 1.4	2.78
$\tau_2^{\text{beams}}| < 25\,\text{GeV},\ \tau_2^{\text{jets}} < 3.2\,\text{GeV}$	181 ± 5	14.36 ± 0.05	7.3 ± 1.4	2.78
VBF loose	44	8.38	16	2.78
VBF tight	6.7	5.26	44	2.61

TABLE 5: Higgs-purity-related quantities in different VBF-enriched categories. The selections *VBF tight* and *VBF loose* have been defined in section 3.5.2.

the ratio of the expected number of Higgs events and the number of background events in the close vicinity of the Higgs signal region is not significantly depending on the τ_2 bin.
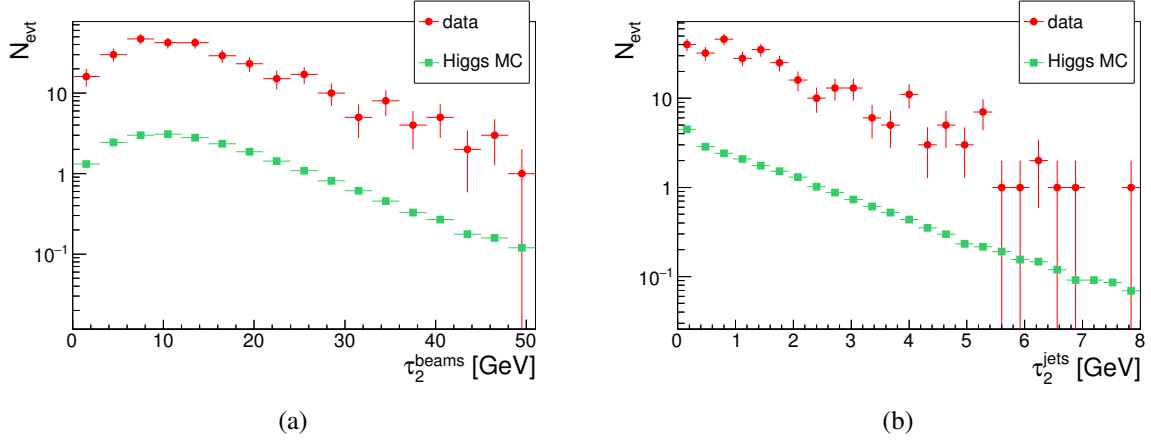
FIG. 69: The τ_2^{beams} spectrum (a) and the τ_2^{jets} spectrum (b) both data and Higgs events from Monte-Carlo simulations. Only data events with a invariant diphoton mass $m_{\gamma\gamma}$ in the range of [120 GeV; 123 GeV] and [127 GeV; 130 GeV] are considered.
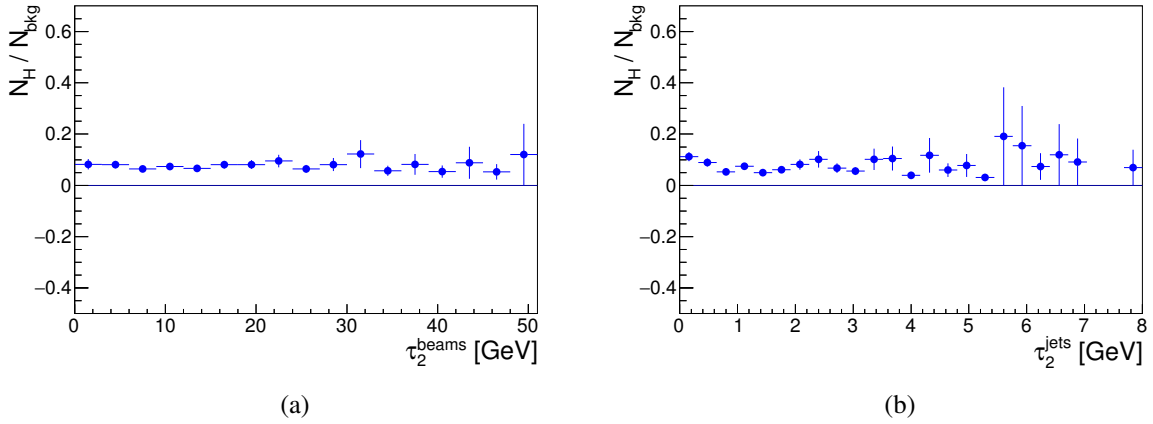
FIG. 70: The ratio of expected Higgs events and background events in the $m_{\gamma\gamma}$ range of [120 GeV; 123 GeV] and [127 GeV; 130 GeV] in τ_2^{beams} bins (a) and τ_2^{beams} bins (b).

In order to understand why the purity in Higgs is comparatively small in the τ_2-based VBF selection, the background processes and the Higgs signal processes will be discussed. The number of gluon fusion and of vector boson fusion events are similar, see table 6, if the cut values on τ_2 are not very tight. Two Feynman diagrams for corresponding Higgs events with dijet signature are shown in figure 71, while in figure 72, three Feynman diagrams of non-Higgs processes with two photons and two partons in the final state are shown. corresponding invariant diphoton mass spectra and fits are shown in figure 65 and 67. The cut values on τ_2 have been chosen such that the uncertainty on μ_{VBF} is expected to be minimal, see figure 74.

Selection	N_H^{MC}	$N_{\mathrm{ggF}}^{\mathrm{MC}}$	$N_{\mathrm{VBF}}^{\mathrm{MC}}$	N_{WH}^{MC}	N_{ZH}^{MC}	N_{ttH}^{MC}
no cut on τ_2	$23.31^{+2.76}_{-2.74}$	$12.14^{+2.74}_{-2.72}$	$10.38^{+0.27}_{-0.29}$	$0.408^{+0.011}_{-0.011}$	$0.250^{+0.010}_{-0.010}$	$0.138^{-0.017}_{+0.012}$
$\tau_2^{\mathrm{beams}} < 40\,\mathrm{GeV}, \tau_2^{\mathrm{jets}} < 6.4\,\mathrm{GeV}$	$20.9^{+2.3}_{-2.3}$	$10.5^{+2.3}_{-2.3}$	$9.79^{+0.26}_{-0.28}$	$0.328^{+0.009}_{-0.009}$	$0.204^{+0.009}_{-0.009}$	$0.028^{+0.003}_{-0.004}$
$\tau_2^{\mathrm{beams}} < 25\,\mathrm{GeV}, \tau_2^{\mathrm{jets}} < 6.4\,\mathrm{GeV}$	$18.1^{+2.0}_{-2.0}$	$8.6^{+2.0}_{-2.0}$	$9.09^{+0.24}_{-0.26}$	$0.256^{+0.007}_{-0.007}$	$0.158^{+0.007}_{-0.007}$	$0.011^{+0.001}_{-0.001}$
$\tau_2^{\mathrm{beams}} < 40\,\mathrm{GeV}, \tau_2^{\mathrm{jets}} < 3.2\,\mathrm{GeV}$	$18.1^{+1.9}_{-1.9}$	$8.4^{+1.9}_{-1.8}$	$9.19^{+0.24}_{-0.26}$	$0.266^{+0.008}_{-0.008}$	$0.168^{+0.007}_{-0.007}$	$(0.019^{+0.002}_{-0.002}$
$\tau_2^{\mathrm{beams}}| < 25\,\mathrm{GeV}, \tau_2^{\mathrm{jets}} < 3.2\,\mathrm{GeV}$	$16.0^{+1.6}_{-1.6}$	$7.0^{+1.6}_{-1.6}$	$8.58^{+0.23}_{-0.24}$	$0.213^{+0.006}_{-0.006}$	$0.133^{+0.006}_{-0.006}$	$(0.008^{+0.001}_{-0.001}$
VBF loose	8.89	3.54	5.23	0.06	0.04	0.01
VBF tight	5.59	0.89	4.65	<0.03	<0.02	<0.011

TABLE 6: Expected number of Higgs events in different Higgs production modes. *VBF tight* and *VBF loose* are defined in section 3.5.2.
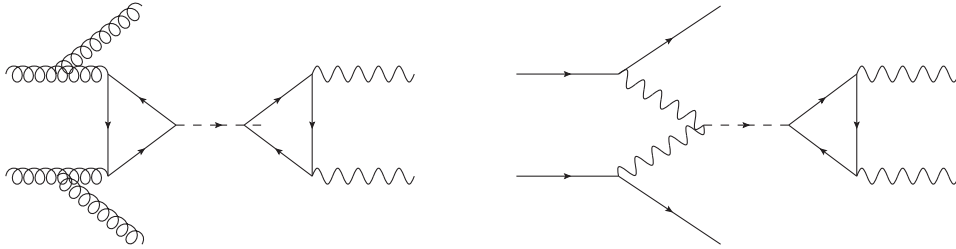
FIG. 71: Feynman diagram for a $H \rightarrow \gamma\gamma$ gluon-fusion process with two jets in the final state (left) and for a $H \rightarrow \gamma\gamma$ vector boson fusion process (right).
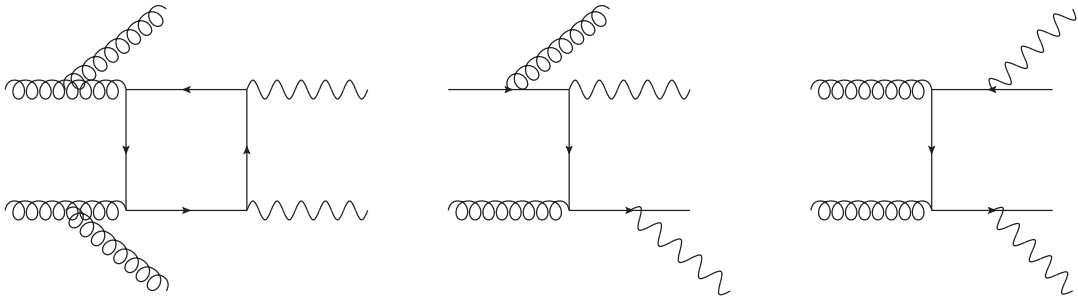
FIG. 72: Feynman diagrams for prompt diphoton background with two jets.

At first appearance, the Higgs processes can not be expected to look much differently than the background processes. As in gluon fusion events, there can be gluon-induced jets from non-Higgs processes with a diphoton in the final state. At the same time, non-Higgs diphoton-dijet processes with quark-induced jets as they can be found in VBF events are possible. Therefore it can not be expected that one can effectively distinguish between Higgs- and non-Higgs events by means of the jet part of τ_2, which measures the width of the jets. Initial-state radiation from the

incoming gluons in non-Higgs background will contribute to the beam part, as it does in ggF events. All together, it is not incomprehensible that the purity in Higgs is relatively low when using a solely-τ_2-based selection and a cut on $\Delta\eta_{jj}$. Of course, one would need more detailed information about the background processes and their kinematics and individual prevalence in order to understand better why the background rejection of a τ_2-based VBF selection is rather ineffective.

The expected uncertainty $\Delta\mu_{\mathrm{VBF}}$ is computed using equation (52) as a function of cuts on the beam- and jet part of τ_2. For this, it is useful to compute the expected statistical uncertainty on the fitted number of Higgs events:

Connected to the purity in Higgs is the statistical uncertainty on the fitted number of Higgs events, which will enter the uncertainty on the VBF signal strength and is expected to be sizable. Therefore it is useful to compute the *expected* statistical uncertainty as a function of the cut values one τ_2 in order to select a VBF selection with smallest possible uncertainty. The statistical uncertainty on the fitted number of events itself is subject to statistical fluctuations. The expected statistical uncertainty is evaluated in the following, using a method called *Asimov dataset* [58]. In order to use this method, one needs a parametrization of the expected $m_{\gamma\gamma}$ spectrum, i.e. the parametrization of the background and of the Higgs signal. The shape of the Higgs peak, as determined in the previous section 3.11.1, is added to the background shape, scaled with the expected number of Higgs events in a given VBF-enriched selection. The result of this is presented in the form of a relative uncertainty on the number of Higgs events in figure 73 as a function of τ_2 cut values. Loose cut values lead to the lowest expected relative uncertainties, which are nevertheless quite sizable.

3.11.3 The Vector Boson Fusion Signal Strength

In the following, the VBF signal strength and its uncertainty will be computed, using equations (51) and (52) from section 3.5.2, respectively. The statistical uncertainties on the expected number of Higgs events from different production modes are taken from Monte-Carlo samples. Except for the perturbative uncertainty on the gluon fusion contamination, the theoretical uncertainties on these numbers are taken from [4]. The perturbative uncertainty on the gluon fusion contamination has been computed in section 3.10. The previous section 3.11.2 yielded the expected statistical uncertainty on the measured number of Higgs events. With all contributions
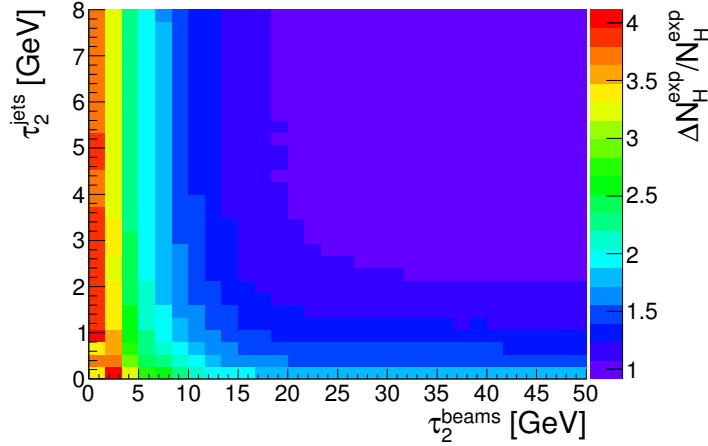
FIG. 73: Ratio of expected number of selected Higgs events to expected statistical uncertainty on the fitted number of Higgs events $\frac{N^{\text{exp.}}}{\Delta N_H^{\text{exp.}}}$ as a function of cuts on τ_2.

of the uncertainty on μ_{VBF} in hand, the expected uncertainty as a function of cuts on τ_2 will be determined. Using this result, a set of cut values is chosen for which the VBF signal strength and its actual uncertainty will be computed.

To measure the VBF signal strength, one needs to measure the number of Higgs events in a given selection. The type of parametrization which is used in the fit of the invariant diphoton mass spectrum is described in the previous section 3.11.2. From the fitted number of Higgs events the predicted number of non-VBF Higgs events is subtracted, which introduces both additional statistical[46] as well as theoretical uncertainties. The perturbative uncertainty on the gluon-fusion contamination, which is subtracted from the fitted Higgs event yield, is the largest among the theoretical uncertainties. The expected contributions from the five considered Higgs production modes in five VBF-enriched selections and the corresponding uncertainties are listed in table 6.

The resulting total uncertainty – using on the *expected* statistical uncertainty on the Higgs signal yield, not the fit uncertainty obtained in the final fitting of the data spectrum – on μ_{VBF} is presented as a function of cuts on τ_2^{beams} and τ_2^{jets} in figure 74. A minimal uncertainty of about 2.0 is expected at loose cut values. The expected uncertainty is completely dominated by the statistical uncertainty on the fitted number of Higgs events. The second-largest contribution comes from the theoretical uncertainty on the gluon fusion cross section passing the selection

---

[46]These statistical uncertainties on the contributions from the different Higgs production modes are small, due to the use of Monte-Carlo simulations with a large number of simulated events.
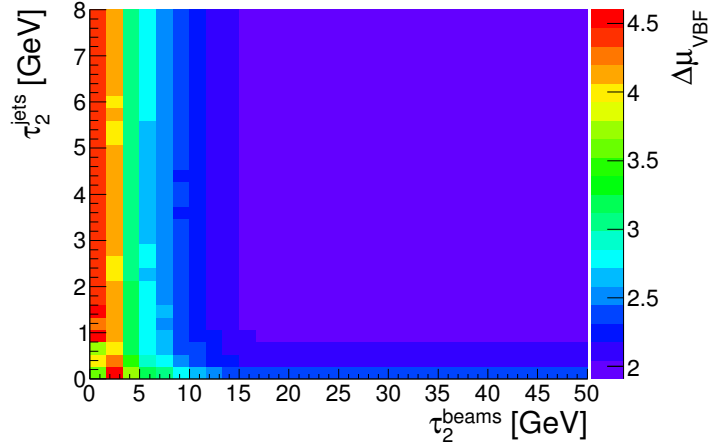
FIG. 74: Uncertainty on the VBF signal strength as function of cut values of τ_2^{beams} and τ_2^{jets}, according to equation (51). Because asymmetrical uncertainties can not be displayed in this format, the larger of the two uncertainties has been chosen.

Selection	N_H^{fit}	N_H^{MC}	$\Delta\mu_{\text{VBF}}^{\text{ggF theo.}}$	μ_{VBF}
no cut on τ_2	22.9 ± 20.0	$23.31^{+2.76}_{-2.74}$	$^{+0.26}_{-0.26}$	$0.95^{+2.0}_{-2.0}$
$\tau_2^{\text{beams}} < 40\,\text{GeV}, \tau_2^{\text{jets}} < 6.4\,\text{GeV}$	16.8 ± 18.9	$20.9^{+2.3}_{-2.3}$	$^{+0.24}_{-0.24}$	$0.6^{+1.9}_{-1.9}$
$\tau_2^{\text{beams}} < 25\,\text{GeV}, \tau_2^{\text{jets}} < 6.4\,\text{GeV}$	9.4 ± 17.2	$18.1^{+2.0}_{-2.0}$	$^{+0.22}_{-0.22}$	$0.0^{+1.9}_{-1.9}$
$\tau_2^{\text{beams}} < 40\,\text{GeV}, \tau_2^{\text{jets}} < 3.2\,\text{GeV}$	14.2 ± 17.5	$18.1^{+1.9}_{-1.9}$	$^{+0.20}_{-0.20}$	$0.6^{+1.9}_{-1.9}$
$\tau_2^{\text{beams}}| < 25\,\text{GeV}, \tau_2^{\text{jets}} < 3.2\,\text{GeV}$	2.8 ± 22.5	$16.0^{+1.6}_{-1.6}$	$^{+0.19}_{-0.19}$	$-0.5^{+2.6}_{-2.6}$

TABLE 7: Measured number of Higgs events, expected number of Higgs events, VBF signal strength and contribution of the theoretical uncertainty on the gluon fusion contamination to the total uncertainty on μ_{VBF} (see also figure 64 in section 3.10) for different VBF-enriched categories.

cuts and is about one order of magnitude smaller than the leading contribution. Again one order of magnitude lower is the contribution from the uncertainty on the expected number of VBF events. The uncertainties resulting from the WH, ZH and $t\bar{t}H$ contributions are in turn more than one order of magnitude smaller than the uncertainty on the selected number of VBF events. In table 7, four τ_2-based categories, two selections from [2] which are not based on τ_2 and the preselection ($N_j \geq 2$, $|\Delta\eta_{jj}| > 2.0$) are listed together with the information necessary to compute the VBF signal strength, according to equation (51), as well as the VBF signal strength itself. The

3.11.4 Final selection

Considering the expected total uncertainty on the VBF signal strength, see figure 74, tight cuts are disfavored due to large statistical uncertainties. Only cut values on τ_2^{beams} above roughly 15 GeV and cut values on τ_2^{jets} above roughly 1 GeV are considered as candidates for a final selection in order to give a result of the VBF signal strength measurement. This constraint agrees with the demand of not cutting tighter than the resolution of the τ_2 measurement, see subsection 3.8.

Based on these two constraints, from the listed selections in table 7 a cut menu is chosen to be $\tau_2^{\text{beams}}|_{\text{cut}} = 40\,\text{GeV}$, $\tau_2^{\text{jets}}|_{\text{cut}} = 6.4\,\text{GeV}$, because this selection results in the smallest relative uncertainty on the fitted number of Higgs events among the four example selections. The result for the signal strength is accordingly

$$\mu_{\text{VBF}} = 0.6^{+1.9}_{-1.9} = 0.6 \pm 1.9\,(\text{stat.})\,^{+0.2}_{-0.2}\,(\text{theory}).$$

The corresponding spectrum is shown in figure 67a. The uncertainty is composed of the following contributions, which, added in quadrature, result in values for the only very slightly asymmetrical uncertainties of +1.91420 and -1.91418, rounded to 1.9:

- $\Delta\mu_{\text{VBF}}^{N_H} = \pm 1.9$

- $\Delta\mu_{\text{VBF}}^{N_{\text{ggF}}} = \pm 0.2$

- $\Delta\mu_{\text{VBF}}^{N_{\text{VBF}}} = \pm 0.03$

- $\Delta\mu_{\text{VBF}}^{N_{WH,ZH,ttH}} = \pm 0.001$

Because of the large uncertainty, the estimated value of $\mu_{\text{VBF}} = 0.6$ is well compatible with the assumption that the Standard Model is valid. A comparison with the result for μ_{VBF} from the standard analysis [2], i.e. $\mu_{\text{VBF}} = 0.8 \pm 0.7 = 0.8 \pm 0.7\,(\text{stat.})\,^{+0.2}_{-0.1}\,(\text{syst.})\,^{+0.2}_{-0.3}\,(\text{theory})$, shows that the uncertainty resulting from this simple analysis is considerably larger than the uncertainty obtained in the more sophisticated standard analysis, which can be also attributed to the relatively low purity in Higgs which can be achieved by cuts on τ_2, see figure 68 and 70. The multivariate analysis which has been used in the official analysis is employing several variables which can be used to discriminate both against non-Higgs background and ggF events. It must be also

noted that this result of the standard analysis is taking into account the entire 2012 and 2011 data set, whereas in this analysis 75.7 % of the 2012 dataset could be used. Hence, the statistical uncertainty on this measurement could be reduced by a modest degree by taking more data into account, when available. The treatment of the systematic uncertainties was not in the scope of this thesis; more studies would be necessary to evaluate these. In general, they are expected to be of similar size as in [2].

A result of this study is that the statistical uncertainty is, at least in this simple method of computing μ_{VBF}, too high as that one could draw benefits from the lower impact of the perturbative uncertainty on the gluon-fusion cross section. With higher statistics, it would be advantageous to cut tighter than it has been done in this final selection.

4 Conclusion

The signal strength of the vector boson fusion Higgs production mode is an important input for the measurement of the Higgs boson's coupling to the weak gauge bosons. In this thesis, the inclusive event shape observable τ_2 has been investigated with the aim to create a vector boson fusion selection based on this variable.

The gluon fusion process is expected to have a cross section about one order of magnitude larger than the vector boson fusion cross section. Therefore the amount of the gluon fusion contamination in a VBF-enriched sample and its uncertainty are of primary interest.

The variable τ_2 has been defined and its spectra have been studied for simulated gluon-fusion- and for vector boson fusion event samples. It proved useful to divide the 2-jettiness into a beam part and a jet part, $\tau_2 = \tau_2^{\text{jets}} + \tau_2^{\text{beams}}$. The beam part, τ_2^{beams}, is a measure of additional radiation, especially in the central region, while the jet part, τ_2^{jets}, is a measure of the width of the two leading jets. Both the jet and the beam part of τ_2 tend to be larger for gluon fusion events, allowing for an effective selection of vector boson fusion events by imposing upper limits on τ_2 or its components τ_2^{beams} and τ_2^{jets}. The expected selection efficiencies and purities have been calculated as a function of the cuts on τ_2^{beams} and τ_2^{jets} using Monte-Carlo simulations.

In order to select the cut menu such that resolution effects are of minor impact, the resolution with respect to detector- and reconstruction effects has been determined. The remaining contributions to the total resolution between the value of τ_2 at the inclusive truth level and at reconstruction level, have been studied; these contributions result from the limited acceptance in pseudorapidity, from the lower threshold on the particle p_{T} of $0.5\,\text{GeV}$ and from the exclusion of neutral particles. The resolution contributions from the event reconstruction and from the exclusion of neutral particles are the largest contributions to the resolution, followed by the contribution of the lower cut on the particles' transverse momentum. The acceptance cut in η gives the smallest contribution. Because the resolution effects are considerable large, it is advantageous that for the results of this study, such as the computation of the perturbative uncertainty or the determination of the VBF signal strength, no unfolding had to be performed.

Common to many VBF selections is that a veto against additional radiation in the central region is imposed; this is also the case for the VBF selection based on τ_2. The perturbative uncertainty on the number of gluon-fusion events selected by the VBF selection is depending

on the phase space restrictions which the VBF selection imposes. Using the Stewart-Tackmann method, the uncertainty resulting from a central jet veto has been estimated as a function of the cuts on τ_2^{beams} and τ_2^{jets}. This uncertainty is effectively independent on on the cut on the jet part of τ_2. Tighter cuts on the beam part, however, increase the theoretical uncertainty. The VBF signal strength has been computed using 8 TeV data[47]. In order to compute the VBF signal strength, the number of Higgs events in the data sample using different τ_2-based categories has been measured. For this, the background shape has been parametrized, based on the data. Cuts on τ_2 are not effective in rejecting non-Higgs background; hence, the expected purity in Higgs is rather low. The VBF signal strength and its uncertainty have been computed based on the assumption that the non-VBF Higgs production mode cross sections are as predicted in the Standard Model. The uncertainty on the VBF signal strength depends the statistical and theoretical uncertainties on the contributions of the various Higgs production modes as well as on the statistical uncertainty of the fitted number of Higgs events. The latter is completely dominating the total uncertainty on the measured VBF signal strength. The uncertainty on the measurement of the VBF signal strength μ_{VBF} is smallest for loose selections at the presently available integrated luminosity. Not all uncertainties could be considered in the scope of this thesis; for example, there will be uncertainties on the 2-jettiness which are related to tracking, the selection of the hard-interaction vertex, and uncertainties due to the modelling of multi-parton interactions.

The result for the VF signal strength is

$$\mu_{\mathrm{VBF}} = 0.6 \pm 1.9 = 0.6 \pm 1.9\,(\mathrm{stat.}) \pm 0.2\,(\mathrm{theory}).$$

Due to the large uncertainty, the value of 0.6 for the VBF signal strength measurement is compatible with the Standard Model. Since the statistical uncertainty is by far the leading contribution to the uncertainty on the VBF signal strength, it would be useful to reconsider the cut menu when the statistical uncertainty is no longer dominant, since the contribution of the theoretical uncertainty can be minimized by cutting tight on τ_2. Moreover, the 2-jettiness could be used in a more sophisticated analysis like [2] as an input variable for a Boosted Decision Tree, for example as a replacement of $\Delta\phi_{H-jj}$. To some extent, quark- and gluon jets can be

---

[47]Due to technical reasons, not the total amount of integrated luminosity could be used but only 75.7 % of it.

distinguished by the 2-jettiness, which would be a useful extension of the present standard analysis.

The LHC environment after the restart of the collider in this year will be different than considered in this analysis. There will be more pile-up, which complicates the selection of the correct vertex. A high Higgs vertex selection efficiency is very important for the use of τ_2, and therefore the usability of the 2-jettiness, or in general, N-jettiness in the new LHC environment needs to be examined if this observable is intended to be used for studies using data from the next LHC run.

References

[1] The ATLAS Collaboration. *Observation of a new particle in the search for the Standard Model Higgs boson with the ATLAS detector at the LHC*. Phys. Lett. B **716** (2012). 2012.

[2] The ATLAS Collaboration. *Measurement of Higgs boson production in the diphoton decay channel in pp collisions at center-of-mass energies of 7 and 8 TeV with the ATLAS detector*. Phys. Rev. D **90**, 112015. 2014.

[3] The ATLAS Collaboration. *Study of the spin and parity of the Higgs boson in HVV decays with the ATLAS detector*. ATLAS-CONF-2015-008. 2015.

[4] LHC Higgs Cross Section Working Group, S. Heinemeyer, C. Mariotti, G. Passarino, and R. Tanaka (Eds.). *Handbook of LHC Higgs Cross Sections: 3. Higgs Properties*. CERN-2013-004, FERMILAB-CONF-13-667-T. 2013.

[5] I.W. Stewart, F.J. Tackmann, W.J. Waalewijn. *N-Jettiness: An Inclusive Event Shape to Veto Jets*. Phys. Rev. Lett. **105** (2010) 092002. 2010.

[6] B.R. Martin, G. Shaw. *Particle Physics*, Wiley. 2008.

[7] K.A. Olive *et al.* (Particle Data Group). *Particle Physics Booklet*. Chin. Phys. C **38**, 090001 (2014). 2014.

[8] M.E. Peskin, D.V. Schroeder. *An Introduction to Quantum Field Theory*, Westview Press. 1995.

[9] I.J.R. Aitchison, A.J.G. Hey. *Gauge Theories in Particle Physics, Volume 2, Non-Abelian Gauge Theories*. CRC Press. 2013.

[10] M. Robinson. *Symmetry and the Standard Model*, Springer-Verlag New York. 2011.

[11] The ATLAS Collaboration. *Measurement of the Higgs boson mass from the $H \rightarrow \gamma\gamma$ and $H \rightarrow ZZ^* \rightarrow 4l$ channels with the ATLAS detector using 25 fb^{-1}*. Phys. Rev. D **90**, 052004 (2014). 2014.

[12] The ATLAS Collaboration. *Evidence for the spin-0 nature of the Higgs boson using ATLAS data*. Phys. Lett. B **726** (2013) 120. 2013.

[13] LHC Higgs Cross Section Working Group, S. Heinemeyer, C. Mariotti, G. Passarino, R. Tanaka (ed.), *Handbook of LHC Higgs Cross Sections: 1. Inclusive Variables*. CERN-2011-002. 2011.

[14] S. Gangal, F.J. Tackmann, *Next-to-leading-order uncertainties in Higgs+2 jets from gluon fusion*. Phys. Rev. D **87** (2013) 093008. 2013.

[15] I.W. Stewart, F.J. Tackmann. *Theory Uncertainties for Higgs and Other Searches Using Jet Bins*. Phys. Rev. D **85** (2012) 034011. 2011.

[16] I.W. Stewart, F.J. Tackmann, J.R. Walsh, S. Zuberi, *Jet p_T resummation in Higgs production at NNLL′+ NNLO*. Phys.Rev. D **89** (2014) 054001. 2013.

[17] C.F. Berger, C. Marcantonini, I.W. Stewart, F.J. Tackmann, W.J. Waalewijn. *Higgs Production with a Central Jet Veto at NNLL + NNLO*. JHEP **1104** (2011) 092. 2010.

[18] O.S. Brüning, P. Collier, P. Lebrun, S. Myers, R. Ostojic, J. Poole, P. Proudlock (Eds.), *LHC Design Report, Volume 1: The LHC Main Ring*, CERN. 2004.

[19] M. Lamont. *Status of the LHC*. Journal of Physics: Conference Series **455**. 2013.

[20] M. Lamont. *The LHC's first long run*. `http://cerncourier.com/cws/article/cern/54381`. Visited 24.3.2015.

[21] ATLAS Experiment ©2014 CERN. `http://www.atlas.ch/photos/full-detector.html`. Visited 24.3.2015.

[22] The ATLAS Collaboration. *The ATLAS Experiment at the CERN Large Hadron Collider*. JINST **3** (2008) S08003. 2008.

[23] The ATLAS Collaboration. *Electron and photon energy calibration with the ATLAS detector using LHC Run 1 data*. Eur. Phys. J. C **74** (2014). 2014.

[24] The ATLAS Callaboration. *The ATLAS Inner Detector commissioning and calibration*. Eur. Phys. J. **C70** (2010). 2010.

[25] ATLAS Experiment ©2008 CERN. *Computer generated image of the ATLAS inner detector*. `http://cdsweb.cern.ch/record/1095926`. Visited 1.3.2012.

[26] G. Pospelov. *The overview of the ATLAS local hadronic calibration*. Journal of Physics: Conference Series **160**. 2009.

[27] P. Krieger. *The ATLAS Liquid Argon Calorimeter: Construction, Integration, Commissioning and Performance from Selected Particle Beam Test Results*. IEEE Nuclear Science Symposium Conference Record. 2005.

[28] The ATLAS Collaboration. *Performance of the ATLAS Inner Detector Track and Vertex Reconstruction in the High Pile-Up LHC Environment*. ATLAS-CONF-2012-042. 2012.

[29] The ATLAS Collaboration. *Expected Performance of the ATLAS Experiment - Detector, Trigger and Physics*. SLAC-R-980, CERN-OPEN-2008-020, 2009

[30] ATLAS Experiment ©2014 CERN. *First 900 GeV Collision Events in Stable-Beam Conditions with Inner Detector Fully Powered, December 6, 2009.* `http://atlas.web.cern.ch/Atlas/public/EVTDISPLAY/events2009.html`. Visited 9.3.2015.

[31] The ATLAS Collaboration. *Performance of primary vertex reconstruction in proton-proton collisions at $\sqrt{s} = 7\,\text{TeV}$ in the ATLAS experiment*, ATLAS-CONF-2010-069. 2010.

[32] W. Lampl, S. Laplace, D. Lelas, P. Loch, H. Ma, S. Menke, S. Rajagopalan, D. Rousseau, S. Snyder, G. Unal. *Calorimeter Clustering Algorithms: Description and Performance*. ATL-LARG-PUB-2008-002. 2008.

[33] The ATLAS Collaboration. *Electron reconstruction and identification efficiency measurements with the ATLAS detector using the 2011 LHC proton–proton collision data*. Eur. Phys. J. C **74** (2014) 2941. 2014.

[34] The ATLAS Collaboration. *Measurements of the photon identification efficiency with the ATLAS detector using* $4.9\,\text{fb}^{-1}$ *of pp collision data collected in 2011*. ATLAS-CONF-2012-123. 2012.

[35] The ATLAS Collaboration. *Measurement of the inclusive isolated prompt photon cross section in pp collisions at $\sqrt{s} = 7\,\text{TeV}$ with the ATLAS detector*. Phys. Rev. D **83** (2011) 052005. 2010.

[36] M. Cacciari, G.P. Salam. *The anti-k_T jet clustering algorithm*. JHEP **0804** (2008) 063. 2008.

[37] The ATLAS Collaboration. *Jet energy measurement with the ATLAS detector in proton-proton collisions at $\sqrt{s} = 7\,\text{TeV}$*. Eur. Phys. J. C **73** (2013) 2304. 2011.

[38] The ATLAS Collaboration. *Pile-up subtraction and suppression for jets in ATLAS*. ATLAS-CONF-2013-083. 2013.

[39] *Vertex reconstruction plots*. `http://atlas.web.cern.ch/Atlas/GROUPS/PHYSICS/IDTRACKING/PublicPlots/ATL-COM-PHYS-2012-474/`. Visited 9.3.2015

[40] The ATLAS Collaboration. *Jet energy measurement and its systematic uncertainty in proton–proton collisions at $\sqrt{s} = 7\,\text{TeV}$ with the ATLAS detector*. Eur. Phys. J. C **75** (2015) 17. 2015

[41] *LuminosityPublicResults* . `https://twiki.cern.ch/twiki/bin/view/AtlasPublic/LuminosityPublicResults#Publications_and_Conference_Resu`. Visited 6.4.2015.

[42] T. Sjostrand, S. Mrenna, P.Z. Skands. *A Brief Introduction to PYTHIA 8.1*. Comput. Phys. Commun. **178** (2008). 2007.

[43] P. Nason. *A New method for combining NLO QCD with shower Monte Carlo algorithms*. JHEP **0411** (2004) 040. 2004.

[44] S. Frixione, P. Nason, C. Oleari. *Matching NLO QCD computations with parton shower simulations: the POWHEG method*. JHEP **0711** (2007) 070. 2007.

[45] S. Alioli, P. Nason, C. Oleari, E. Re. *NLO Higgs boson production via gluon fusion matched with shower in POWHEG*. JHEP **0904** (2009) 002. 2008.

[46] P. Nason, C. Oleari. *NLO Higgs boson production via vector boson fusion matched with shower in POWHEG*. JHEP **1002** (2010) 037. 2009.

[47] E. Bagnaschi, G. Degrassi, P. Slavich, A. Vicini. *Higgs production via gluon fusion in the POWHEG approach in the SM and in the MSSM*. JHEP **1202** (2012) 088. 2011.

[48] S. Alioli, P. Nason, C. Oleari, E. Re. *A general framework for implementing NLO calculations in shower Monte Carlo programs: the POWHEG BOX*. JHEP **1006** (2010) 043. 2010.

[49] G. Bevilacqua *et al.*. *Helac-nlo*. Comput. Phys. Commun. **184** (2013) 986-997. 2011.

[50] H.-L. Lai *et al. New parton distributions for collider physics*. Phys. Rev. D **82** (2010) 074024. 2010.

[51] J. Pumplin *et al. New Generation of Parton Distributions with Uncertainties from Global QCD Analysis*. JHEP **0207** (2002) 012. 2002.

[52] GEANT4 Collaboration. *GEANT4: A Simulation toolkit*. Nucl. Instrum. Meth. A **506** (2003) 250. 2002.

[53] A. Hoecker *et al. TMVA - Toolkit for Multivariate Data Analysis*. PoS **ACAT** (2007) 040. 2007.

[54] T.T. Jouttenus, I.W. Stewart, F.J. Tackmann, W.J. Waalewijn. *Jet mass spectra in Higgs boson plus one jet at next-to-next-to-leading logarithmic order*. Phys. Rev. D **88**, 054031. 2013.

[55] Private communication

[56] M. Bähr *et al. Herwig++ Physics and Manual*. Eur.Phys.J. C **58** (2008) 639-707. 2008.

[57] T. Skwarnicki. *A study of the radiative cascade transitions between the upsilon-prime and upsilon resonances*. DESY F31-86-02. 1986.

[58] G. Cowan, K. Cranmer, E. Gross, O. Vitells. *Asymptotic formulae for likelihood-based tests of new physics*. Eur. Phys. J. C **71** (2011) 1554. 2010.

Acknowledgements

I would like to thank Kerstin Tackmann who supervised this thesis. I am very grateful for this and the efforts which are connected with that. In fact, there are many I would like to thank. My thanks also go to Marco Filipuzzi for his work that made this thesis possible and for his many helpful advices. Furthermore I thank Frank Tackmann who explained me the theoretical basics which are of importance in this work and who contributed a lot of expertise. I thank Elisabeth Petit for her helpful support and advice and for proofreading many parts of this thesis. I would also like to thank Dag Gillberg and Florian Bernlochner, who created the code which I have used for the computation of the theoretical uncertainties and who gave me advice how to use it. My thanks also go to Peter Schleper who was so kind to be the secondary supervisor of this thesis and to review it. Moreover, I would like to express my gratitude to Jannis Lehmann and Lennart Heino who gave me valuable feedback in the process of writing. Finally, I would like to express my gratitude to my family and friends for all their direct and indirect support.